Modeling and Design Optimization of Permanent Magnet Variable Flux Machines

Amirmasoud Takbash

A Thesis

In the Department

of

Electrical and Computer Engineering

Presented in Partial Fulfillment of the Requirements

for the Degree

Doctor of Philosophy (Electrical and Computer Engineering) at

Concordia University

Montreal, Quebec, Canada

July 2018

CONCORDIA UNIVERSITY

SCHOOL OF GRADUATE STUDIES

This is to certify that the thesis prepared

By: Amirmasoud Takbash

Entitled: Modeling and Design Optimization of Permanent Magnet Variable Flux Machines

and submitted in partial fulfillment of the requirements for the degree of

Doctor of Philosophy (Electrical & Computer Engineering)

complies with the regulations of the University and meets the accepted standards with respect to originality and quality.

Signed by the final examining committee:

_____ Chair
Dr. Onur Kuzgunkaya

_____ External Examiner
Dr. Bhekisipho Twala

_____ External to Program
Dr. Subhash Rakheja

_____ Examiner
Dr. Akshay Kumar Rathore

_____ Examiner
Dr. Luiz A.C. Lopes

_____ Examiner
Dr. Christopher W. Trueman

_____ Thesis Supervisor
Dr. Pragasen Pillay

Approved by

Dr. Mustafa K. Mehmet Ali, Graduate Program Director

Monday, August 20, 2018

_____

Dr. Amir Asif, Dean
Faculty of Engineering and Computer Science

ABSTRACT

Modeling and Design Optimization of Permanent Magnet Variable Flux Machines

Amirmasoud Takbash, Ph.D.

Concordia University, 2018

Permanent magnet synchronous machines (PMSMs) with rare-earth magnets are widely used especially in traction applications as a result of their higher efficiency and torque density in comparison with other electrical motors. Due to price fluctuations and limited production of rare-earth materials, it is essential to find alternatives to the rare-earth PMSMs for different applications. This thesis focuses on the application of Aluminum-Nickel-Cobalt (AlNiCo) magnets in PMSMs. AlNiCo magnets can theoretically provide torque densities comparable to rare-earth magnets in electrical machines. The application of AlNiCo magnets in electrical machines can improve the field-weakening performance, due to the possibility of varying their magnetic flux density using armature current pulses. As a result, these machines are named variable flux machines (VFMs).

This thesis presents an analytical model for the VFM to calculate the no-load air gap flux density and consequently, the no-load back-EMF, torque peak to peak value, average torque, and magnetization current. The proposed model is used to develop an analytical design criterion for spoke type AlNiCo-based VFMs. An experimental characterization of an existing spoke type VFM at different magnetization levels is done of the torque waveform, the torque-angle characteristics, the no-load back-EMF and the magnetization/demagnetization energy. An optimization procedure to reduce the torque ripple and the magnetization current of the spoke type AlNiCo-based VFM is then proposed.

A new VFM design with radially magnetized interior magnets is presented to enhance the torque density in the field-weakening operating condition. The torque-speed and power-speed characteristics of the VFM are calculated considering the demagnetization of the AlNiCo magnets in the field-weakening region. The proposed design keeps the fully magnetized condition at both no-load and full-load conditions and provides high power densities at a wider speed range. This design is also optimized to have reduced torque ripple.

An improved core loss model is proposed and implemented in the finite element software,

and an experimental method based on the flux controllability of the VFM is developed to measure the mechanical and core losses at the no-load condition. These results are then used to verify the proposed core loss model.

ACKNOWLEDGMENTS

I would like to express my deep and sincere gratitude to my supervisor, Professor Pragasen Pillay for giving me the opportunity to go through the Ph.D. program. He has inspired me in many ways, from the beginning to the end of my research program. I also would like to thank him for the financial support.

I would also like to thank my committee members, Professor Bhekisipho Twala, Professor Subhash Rakheja, Professor Christopher W. Trueman, Professor Luiz A. C. Lopes and Dr. Akshay Kumar Rathore for serving as my committee members even at hardship. I also want to thank all of them for their brilliant comments and suggestions and their valuable time.

My sincere gratitude goes to all my colleagues from the PEER group at Concordia University for being supportive during my Ph.D. journey. Sincere thanks to Dr. Maged Ibrahim, Dr. Akrem Mohamed Aljehaimi, Rajendra Thike and Chirag Desai for their help with the experimental measurements and for their advice in replying to the reviewers' comments.

I would like to express my deepest gratitude to my beloved wife Mozhdeh, for her emotional support and continuous encouragement, to my parents, Maryam and Asghar, and my brothers, Majidreza and Alireza, for their unconditional support throughout my entire life.

I would like to acknowledge the support of the Natural Sciences & Engineering Research Council of Canada and Hydro-Québec for this work. This work was supported in part by the R&D program of the NSERC Chair entitled "Design and Performance of Special Electrical Machines" established in Concordia University.

CONTENTS

LIST OF FIGURES

LIST OF TABLES

LIST OF ABBREVIATIONS

Permanent Magnet Synchronous Motor	PMSM
Neodymium Iron Boron	NdFeB
Aluminum Nickel Cobalt	AlNiCo
Samarium Cobalt	SmCo
Dysprosium	Dy
Variable Flux Machine	VFM
Electro Motive Force	EMF
Doubly Excited Synchronous Machine	DESM
Doubly Salient Permanent Magnet	DSPM
Memory Machine	MM
Magneto Motive Force	MMF
Finite Element Analysis	FEA
One Dimensional	1D
Two Dimensional	2D
Brush Less DC	BLDC
Fractional Slot Concentrated Winding	FSCW
Permeance Coefficient	PC
Magnetization Level	ML
Genetic Algorithm	GA
Space Vector Pulse Width Modulation	SVPWM
Electric Vehicle	EV
Total Harmonic Distortion	THD

LIST OF SYMBOLS

α_p	Pole embrace
α	Slot pitch angle
α_{b1}, α_{b1}	Angle between the magnet and the barriers
τ, τ_p	Pole pitch
τ_s	Slot pitch
φ	Scaler magnetic potential
φ_{g0}	No-load air gap magnetic flux
μ_0	Air permeability
μ_{rec}	Relative recoil permeability of the magnet
θ	Torque angle
θ_p	Pole arc angle
θ_{1sb}, θ_{2sb}	Small barrier angle
θ_{mb}	Main barrier angle
δ, g	Air gap length
γ	Tooth tang angle
γ_s	Short pitch angle
λ_{fp}	Linkage flux in the partial magnetization condition
λ_{ff}	Flux linkage of the fully magnetized VFM
λ_m	Magnet flux
ω	Rotor electrical speed
ω_{base}	Rotor electrical base speed
$\mathcal{R}_s$	Reluctances of the stator
$\mathcal{R}_g$	Reluctances of the air gap
$\mathcal{R}_m$	Reluctances of the magnets

$\mathcal{R}_{ri}$	Reluctances of the rotor
A_g	Air gap area
A_m	Magnet area
A_j	Area of the mesh element
a	Number of layers
B_g	Air gap flux density
B_{go}	No-load air gap magnetic flux density
B_{g01}	Fundamental component of no-load air gap flux density
B_m	Magnet flux density
$B^{(1)}$	Average of flux density rate of change
b_o	Slot opening for the rectangular slot
b_1	Slot width
e_0	No-load back-EMF
f_{eq}	Equivalent frequency
g_{min}/g_{max}	Air gap length minimum/maximum
H_g	Air gap magnetic field intensity
H_m	Magnet magnetic field intensity
h_m	Magnet length
h_0	Tooth tip thickness
h_1	Tooth tip length
I_q	q-axis current
I_d	d-axis current
I_{mag}	Magnetization current
I_{dm}	limit of the negative d-axis current
i_a	Peak value of phase current

$\vec{J}$	Current density vector
K_c	Carter's coefficient
K_d	Distribution factor
K_p	Slot-pitch factors
K_s	Skewing factor
L_d	*d*-axis inductance
L_q	*q*-axis inductance
L_{stk}, L	Stack length
l_{1ur}	Upper rib horizontal length
l_{2ur}	Upper rib vertical length
l_{1mb}	Main barrier horizontal Length
l_{2mb}	Main barrier vertical length
$\vec{M}$	Residual magnetization vector
N_s	Number of winding turns
N_{spp}	number of slot per pole per phase
N	Number of current carrying turns
n_{tc}	number of turns for each coil
P	Number of pole pairs
P_1	Permeance in the air gap area
P_2	Permeance in the tooth area
$P_{core,i}$	Total core losses of part *i*
P_{mech}	Mechanical loss
P_{in}	Input power
P_{core}	Core loss
P_{max}	Maximum power

p_j	Estimated core loss density in each mesh element
R_{sb}	Small barrier radius
R_{mb}	Main barrier radius
R_{ro}	Rotor outer radius
R_{si}	Stator inner radius
r_{mb}	Main barrier upper radius
T_{el}	Electromagnetic torque
$T_{PM,mean}$	Average PM torque
T_{mean}	Torque mean value
T_{rel}	Reluctance torque
$T_r\%$	Torque ripple
t_{sb}	Small barrier thickness
t_m	Magnet thickness
V	Volume of magnet
V_{DC}	DC bus voltage
$V_{n,LL}$	RMS value of the line to line no-load back-EMF
V_d	*d*-axis voltage
V_q	*q*-axis voltage
V_m	Maximum achievable voltage
U_s	Stator magnetic potential
W'	Co-energy
W_m	Magnetic energy
w_{ti}	Tooth inner width

Chapter 1. Introduction

This chapter presents an overview on the permanent magnet synchronous motor, its benefits and drawbacks. This chapter is organized as follows: Section 1.1 proposes an introduction to the permanent magnet synchronous motor, permanent magnet materials, and the field-weakening limitations. Different designs of variable flux machines are presented and summarized in section 1.2. Section 1.3 states the problem and section 1.4 explores the research motivations and objectives. The contributions are listed in section 1.5. The dissertation organization is presented in section 1.6.

1.1 Permanent Magnet Synchronous Machine

The permanent magnet synchronous motor (PMSM) originates from the synchronous motor with permanent magnets replacing the wound field circuit. In late 1950s, the availability of switching power devices led to the development of inverters that enabled the replacement of the mechanical commutator with an electronic commutator. Therefore, PMSMs and brushless DC machines were developed. By removing the mechanical commutator, the armature of the DC machine can be on the stator side. This enables better cooling and higher voltages to be achieved. This modification eliminates copper loss in the rotor as well as the maintenance cost of the field exciting circuit. Thus, a PMSM has a higher efficiency, and the cooling design system is easier to implement. Moreover, the application of magnets in the rotor enhance the flux density in the air gap and consequently increases the motor power density and torque-to-inertia ratio. In demanding motion control applications, the PMSM has fast response, compact motor structure, and high efficiency. Interior permanent magnet synchronous motor (IPMSM) offer higher efficiency and torque density, wide range of constant power speed, reliability and potential magnet mass saving. Besides all of the mentioned benefits, the application of PMSMs in different sectors of industry shows drawbacks related to the price of the rare-earth magnets and also the field-weakening capability. These limitations are addressed in the following sections.

1.1.1 Permanent Magnets: Past, Present and Future

Permanent magnet materials are one of the earliest functional materials. Lodestones have been identified since 400 BC in China. Sir William Gilbert reported the magnetic properties of

Carbon steel in the 1600s. The discovery of electromagnetism in the early 19th century by Ampere and the development of Maxwell's equations enabled the link between mechanical energy to electrical energy through the electromagnetism. As a result, simple electric motors and generators were developed by the end of the 1800 [1].

Progress in permanent magnet technology has been enhanced in the dawn of the 20th century to achieve high energy products. The Carbon steel magnetic materials were first developed with energy products around 15 kJ.m^{-3}. In order to avoid the magnetic domain wall motion and enhance the coercive field, the Carbon steels are commonly alloyed with Tungsten and Chromium, thus forming Carbides but their tendency to demagnetize limits their application. In the early 30s, Fe-based oxides (Ferrite) were developed, offering larger coercive fields. Their energy products didn´t substantially improve the steels, but their resistance to corrosion and oxidation, as well as their reduced costs, made them as a favorite material for industrial applications. Aluminum Nickel Cobalt (AlNiCo) as the third group of magnets were developed in the 30s and provided higher coercivity compared to steels [1].

With the advent of the rare-earth magnet, a revolution of magnetic materials occurred in the 1960's. $SmCo_5$ (1966) presented a new class of materials where the dominant force linking the direction of the magnetic flux to the body of the magnet is magneto crystalline anisotropy. The next big jump in energy density came in 1981, after an increase in the price of Cobalt due to political unrest in the world's leading producer for high-quality and low cost Cobalt (Democratic Republic of the Congo). As a result of this uncertainty in the market, a new compound based on Neodymium, Iron, and Boron has been discovered in the research laboratories in Japan and the United States [1]. $Nd_2Fe_{14}B$ has a nearly ideal separation of the Fe atoms resulting in strong exchange coupling of the Fe and Nd sublattices resulting in the highest theoretical $(BH)_{max}$ of any compound to date at 510 kJ.m^{-3}. Fig. 1-1 shows the amount of energy produced by different families of magnets [2]. During the discovery period of rare-earth magnets, Japan and the United States were the major producers of these materials. With the discovery of the rare-earth magnets, the demand for rare-earth elements also increased throughout the 1980s. At the same time, the price of these elements were reduced because of the new resources were becoming available in China. The major producer in the world, the Molycorp's Mountain Pass mine in California, was experiencing problems with aging infrastructure, which required significant investment.

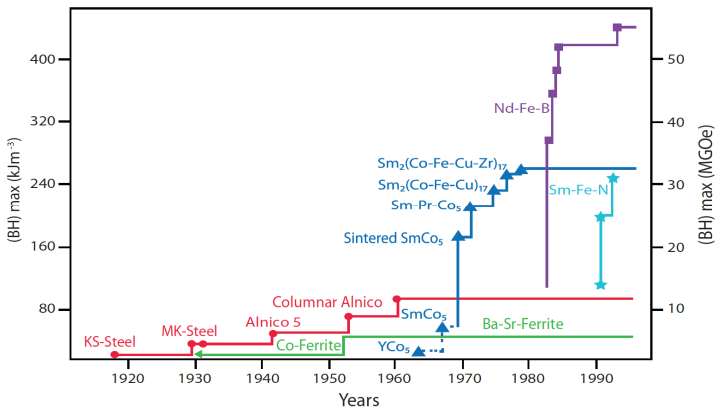

Fig. 1-1: Evolution of the energy product value for different families of permanent magnets [2].

With the low rare earth-element prices, improvements to the Mountain Pass mine were not economically viable, and in a few short years in the 1990s, China became the main producer of rare earth elements [1] as shown in Fig. 1-2.

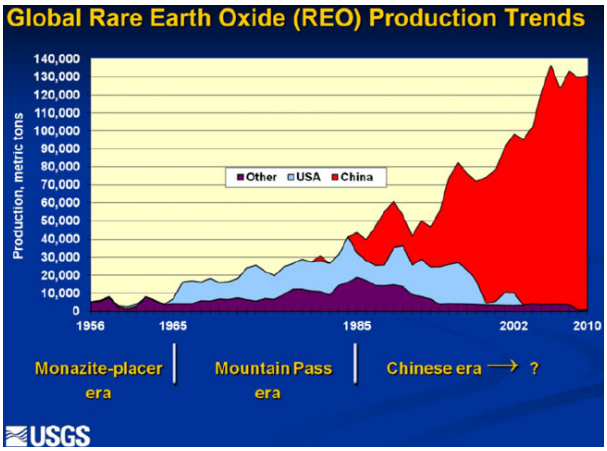

Fig. 1-2: Timeline showing the worldwide production of rare earth elements on an oxide basis by major producers [1].

By 2000, China was dominating the worldwide rare-earth element production. Over the period 2001 to 2005, the majority of the rare-earth magnet companies either ceased production or relocated to China to take advantage of lower manufacturing costs. While the demand for rare-earth magnets was increasing and the rare-earth supplies were limited, China announced that it would begin to reduce its export of the rare-earth element including, Europium, Terbium, and Dysprosium, in 2009 [1]. Regardless of the politics surrounding rare-earth elements, increase in demand, driven primarily by electric machines, is a major factor in both cost and availability of rare-earth elements in the near future.

Fig. 1-3 shows the global rare-earth oxide demand by industry sector for 2014 and 2015 [3].

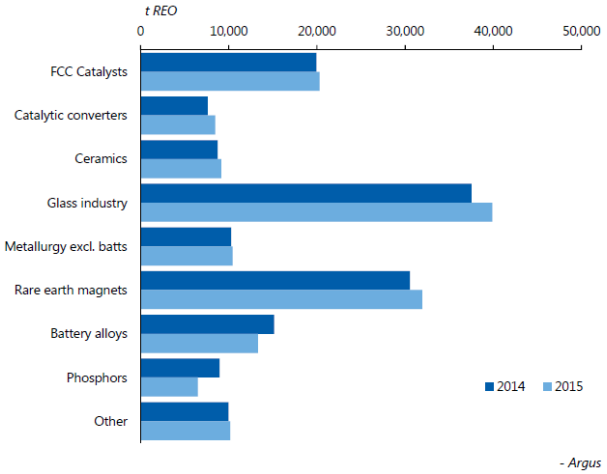

Fig. 1-3: Global rare-earth oxide demand by industry sector [3].

The rare-earth magnet industry is the 2nd highest demand and it is increasing. The higher temperature performance requirement of traction motors requires an adjustment to the Nd-based magnets with the addition of heavy rare-earth elements as Dysprosium (Dy). Dy, was trading near $100/kg in early 2009 to as high as $3400/kg in August of 2011, and it remains near $2000/kg as of April 2012 [1]. Fig. 1-4 shows the price of rare-earth magnets from 2008 to 2016 [3].

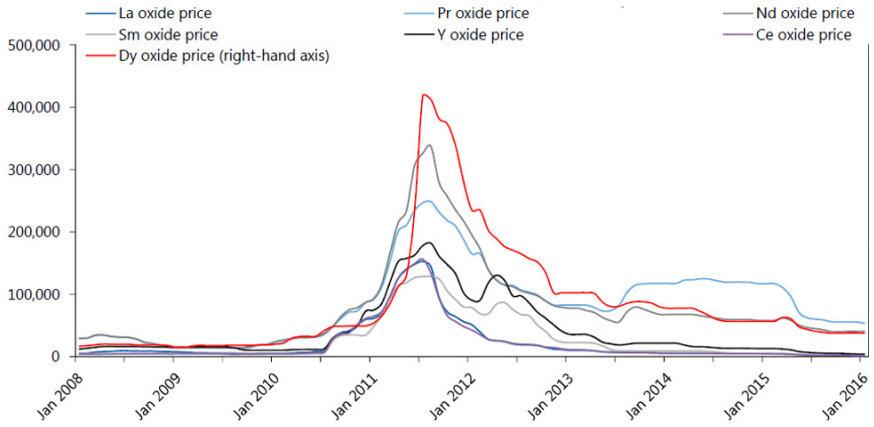

Fig. 1-4: Price of rare-earth oxides from 2008 to 2016 [3].

The high price fluctuation of rare-earth magnets causes issues for rare-earth PMSM manufacturers. Moreover, switching to Sm-based alloys is not a good alternative since Samarium is not available in adequate quantities.

1.1.2 Field-weakening Operation and its Limitations

While the rare-earth magnets in the PMSMs provide a high magnet flux, and as a result, high peak torque and power capability, the air gap flux of these machines is almost constant.

The constant magnet flux causes back electro motive force (back-EMF) limitations at high-speed operation due to the DC-bus voltage limit of the drive. For the high-speed region, the flux linkage of the machine should be weakened to keep the back-EMF within the acceptable range. The effective field-weakening operation becomes a challenge for rare-earth PMSMs, which has restricted their applications in some variable-speed systems. Many investigations have been carried out to enhance the field-weakening capability of PMSMs.

The vector control principle has been successfully applied, where a negative *d*-axis armature current is injected to counter the magnet flux and thus effectively reduce the induced voltage [4]. However, this current causes copper loss, as well as associated iron loss, which arises from the magnetic flux harmonics [5]. As a result of the extra losses in the field-weakening mode of operation, the efficiency of rare-earth PMSMs drops in the high-speed region. Although, several control strategies are reported in the literature [6]-[8], the efficiency problem for field-weakening mode of operation have not been solved completely.

Besides the control strategies, some design modifications are suggested to increase the machine performance during the field-weakening. One of these solutions is the variable flux machine (VFM). Different topologies of VFM are reviewed in the following sections.

1.2 Variable Flux Machines

VFMs are one of the alternatives to solve the problems related to the field-weakening operation in the conventional rare-earth PMSMs. In these machines, the magnet flux can be reduced at higher speed. Fig. 1-5 shows different categories of VFMs based on the methods which are used to control the magnet flux. Pure rare-earth PMSMs can be designed as a VFM with adding the auxiliary AC or DC coils in the rotor or stator. Moreover, the rare-earth PMSMs can be designed as a VFM with some mechanical considerations to provide the leakage flux path in order to reduce the flux linkage at high-speed region. The other category uses the low coercivity magnets in the PMSMs to provide the flux controllability. A combination of low coercivity and rare-earth magnets in the machine is a way to control the flux linkage.

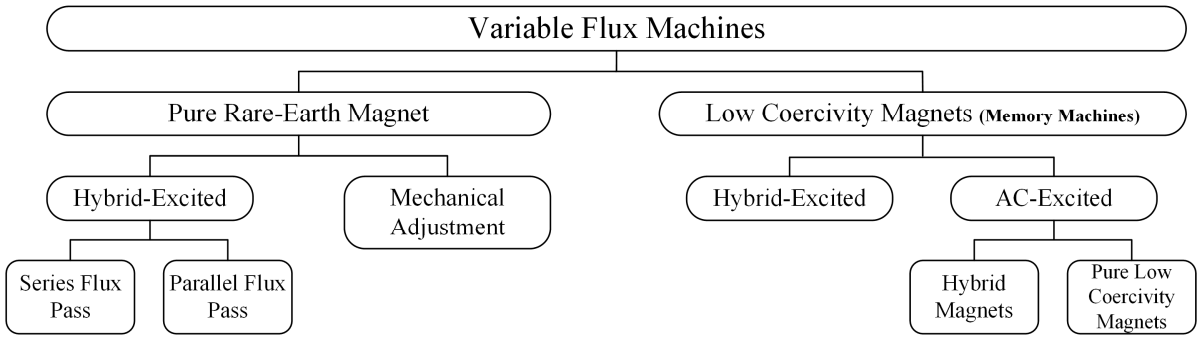

Fig. 1-5: Variable flux machine families.

In this method the rare-earth magnets provide the constant flux, and the machine flux is controlled by magnetizing or demagnetizing the low coercivity magnets using AC or DC coils. Additionally, pure low coercivity magnet based PMSMs are a family of VFMs that are using the armature winding to magnetize or demagnetize the rotor magnets.

All these categories are discussed in more depth in the following sections.

1.2.1 Hybrid-Excited Variable Flux Machines with Field Coil Excitation

Hybrid-excited PMSMs with a separate field coil is one category of VFMs and their potential to extend the field-weakening range has been studied in the literature. This type of VFM can be categorized based on the place of the excitation source and the configuration of the magnets and the field coils flux path.

1.2.1.1 Series Flux Path Hybrid-Excited Machines

Series flux path hybrid excited PMSMs as a family of the VFMs have been presented in the literature [9]-[13]. The doubly excited synchronous machines (DESM) and doubly salient permanent magnet (DSPM) machines are categorized in this family as shown in Fig. 1-6. According to Fig. 1-6(a), for DESM, both excitation sources are in the rotor. Magnets are fixed at the surface of the rotor teeth and the DC coils are wound at the end of the rotor tooth. The core loss reduction and efficiency improvements are reported for this type of DESMs in [9]. Based on Fig. 1-6(b), for the DSPM machine, both field sources are located in the stator in order to avoid the slip rings in the rotor. Both these designs show a reasonable capability of field-weakening. In both designs, the weakening flux line of the DC-coil pass through the magnet, which increases the risk of demagnetization [14].

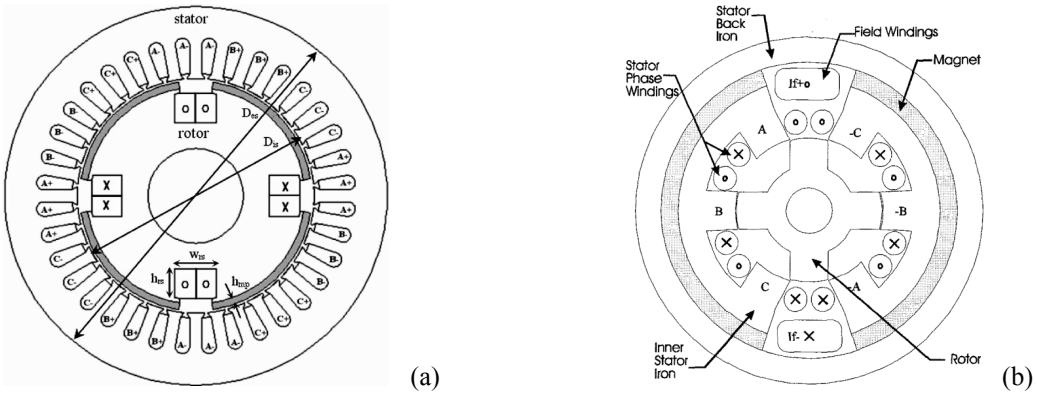

Fig. 1-6: (a): Doubly excited synchronous machines (DESM) [1], and (b): doubly salient permanent magnet (DSPM) machines [10].

1.2.1.2 Parallel Flux Path Hybrid-Excited Machines

This family of hybrid-excited variable flux machines is the most common one that can be categorized based on the configuration of the magnets and the DC coils. The majority of parallel flux path hybrid-excited machines have the magnets in the rotor and the DC coils in the stator [15]-[21]. In this topology a large diameter solenoidal field coil is sandwiched in the stator back iron. This topology has the capability to increase the torque density of the machine [18], that comes with a negative impact on the flux regulation. Both radial and axial flux topologies consequent-pole VFMs with DC coils in the stator are reported as shown in Fig. 1-7.

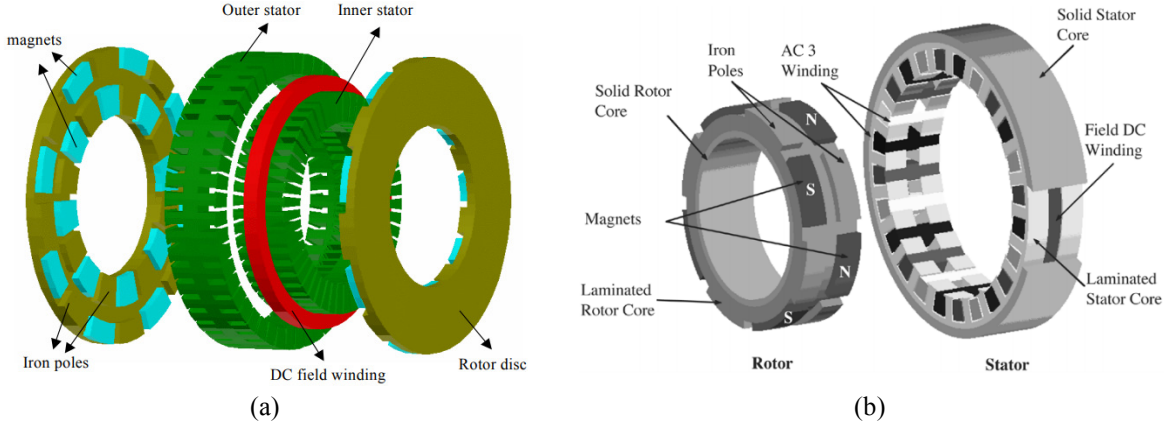

Fig. 1-7: The structure of (a): axial flux consequent-pole VFM [15], and (b): radial flux consequent-pole VFM [17], with DC field coils in the stator.

According to Fig. 1-7, the DC coils are placed in the specific slots in the stator. The consequent-pole designs provide a wide range of air gap flux control without any demagnetization risk for the magnet pieces. The control action is using a simple DC current control without brushes or slip rings [17]. However, the DC winding in the stator reduces the machine power density as the required space reduces inner diameter and/or increases the outer diameter. In addition, the three-dimensional flux distribution in this machine introduces extra losses, as the stator and rotor cores require tangential and axial flux conduction capacity that results in some manufacturing problems [9].

The parallel flux path hybrid-excited machines with both magnet and DC coils in the rotor are not popular because they require slip rings and do have lower torque density [22]-[23]. However, they have simpler topology [14]. Fig. 1-8 shows the topology of a hybrid-excited machine with the DC coils and magnets in the rotor [22]. The parallel flux path is clear in Fig. 1-8.

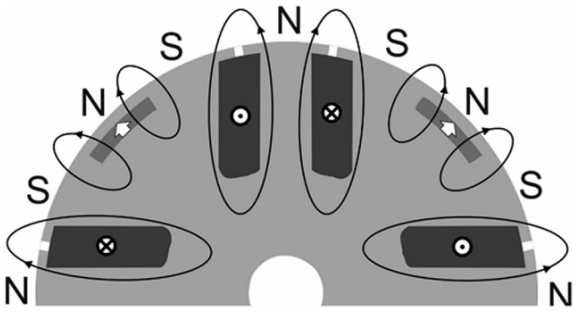

Fig. 1-8: The Hybrid excited machines with field coils and magnets in the rotor [22].

The hybrid-excited machines with magnets and field coils in the stator are categorized as the DSPM machines [24], [25], switched-flux permanent magnet machines [26], [27], and the doubly-excited, dual stator permanent magnet machines [28]. This type of hybrid-excited machines have good flux regulation, less torque density, and the rotor is simple and robust.

1.2.2 Variable Flux Machines with Mechanical Adjustment

In this family of the VFMs, the machine topology changes to provide the flux regulation in the machine. Field-weakening in these machines is achieved through the magnetic flux path changes and increasing the leakage flux in the machine [14].

Field-weakening can be done with adjustment of the rotor [29] or stator [30] sections in an axial flux surface mounted PMSM consisting of a slot-less stator, between two rotor disks. In

these machines, the rotor or stator is multi-section and the flux path and as a result the linking flux of the machine is changed with misaligning these sections. To control the flux of machine, a speed or torque dependent system and an actuator are required which makes the system more complex.

Variable air gap length is another method to provide the flux controllability in PMSMs. An axial flux machine with a variable air gap length using a spring and hinge setup is reported in [14]. Although this machine shows good potential in terms of the flux controllability, the complex mechanical system for air gap length variation affects the torque density and manufacturability.

A PMSM with flux-shorting iron plates in the stator is proposed in [31] as shown in Fig. 1-9. According to this figure, a set of springs and actuators are used to push the iron plated toward the rotor to increase the leakage flux and reduce the linkage flux in the machine.

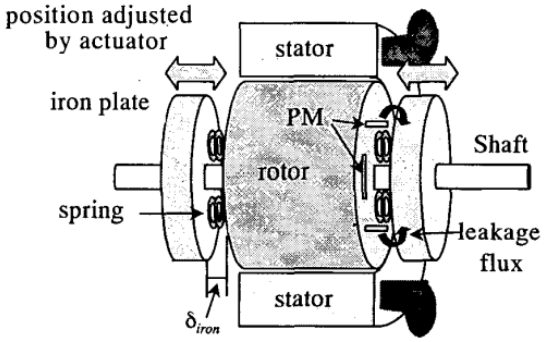

Fig. 1-9: A PMSM with flux-shorting iron plates in the stator [31].

The size adjustment of the flux barriers in the rotor is another mechanical method that is proposed to increase the field-weakening ability of a PMSM. In this machine, iron pieces in the rotor are used to change the size of the flux barriers in the rotor in order to control the leakage flux of machine. Besides the complex mechanical structure, the control of this machine is complicated.

1.2.3 Variable Flux Machines with Low Coercivity Magnets: Memory Machines

A new class of VFMs, named memory machines (MMs) is presented in [32]-[43]. These machines are known for their ability to change the intensity of magnetization and memorize the flux density level in rotor magnets. The application of low coercivity magnets in MMs provides a unique feature of magnet flux controllability using a short-time current pulse without any risk

of the magnet demagnetization, as the rotor magnets can be re-magnetized. The MMS can be categorized based on the type of supply that is used to change the rotor magnetization levels.

1.2.3.1 Hybrid-Excited (DC-Excited) Memory Machines

The concept of DC-excited MM is based on the fact that the magnetization level of magnets in the motor can be regulated by a temporary DC current pulse and be automatically memorized. DC coils in the stator or the rotor of these machines are used to demagnetize or re-magnetize the low coercivity magnets in this machines. In [32], a DC-excited MM is proposed and implemented. The configuration of the proposed memory motor is shown in Fig. 1-10, which adopts a five-phase outer-rotor 30/24-pole doubly salient structure.

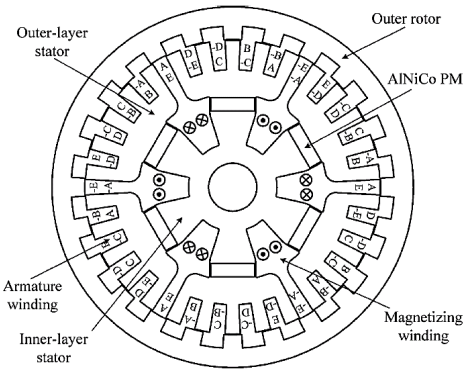

Fig. 1-10: The DC-excited machines with two rotors [32].

Based on an outer rotor doubly salient motor structure, the proposed DC-excited MM can offer effective and efficient online air gap flux control. Hence, it possesses the advantages of mechanical robustness, high efficiency, and wide constant power operation region.

A new topology of hybrid DC-excited MM with both rare-earth and low coercivity magnets in the stator is presented in [33] as shown in Fig. 1-11.

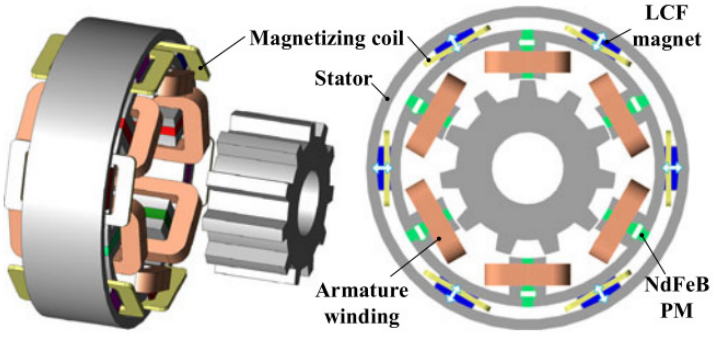

Fig. 1-11: The DC-excited machines with magnets in the stator [33].

In this topology the rare-earth magnets in the stator provide the constant torque in the machine and the low coercivity magnets with the DC coils around them control the flux level in the machine. The rotor of this machine is similar to switch reluctance machines and is simple and rigid which is a great benefit. The DC-excited MMs are complex in terms of structure and manufacturing. Moreover, the DC coils make the control strategy more complicated and in some cases, increase the risk of rare-earth magnet demagnetization.

1.2.3.2 AC-Excited Memory Machines

In AC-excited MMs, the armature windings of the machine provide the magnetic field to magnetize or demagnetize the low coercivity magnets. In this manner, the DC coils are eliminated that makes both configuration and control strategy less complicated.

Hybrid AC-excited MMs are VFMs that use a low coercivity magnet like AlNiCo with a higher coercivity magnet like rare-earth or Ferrite is series or parallel to provide the rotor magnet flux controllability [34]-[37] to improve the torque density of VFM. The higher coercivity magnets provide a constant field whilst the low coercivity magnets offer an additional variable component. The variation of magnet flux is still achievable, and meanwhile, the torque density is boosted thanks to the employment of higher coercivity magnet.

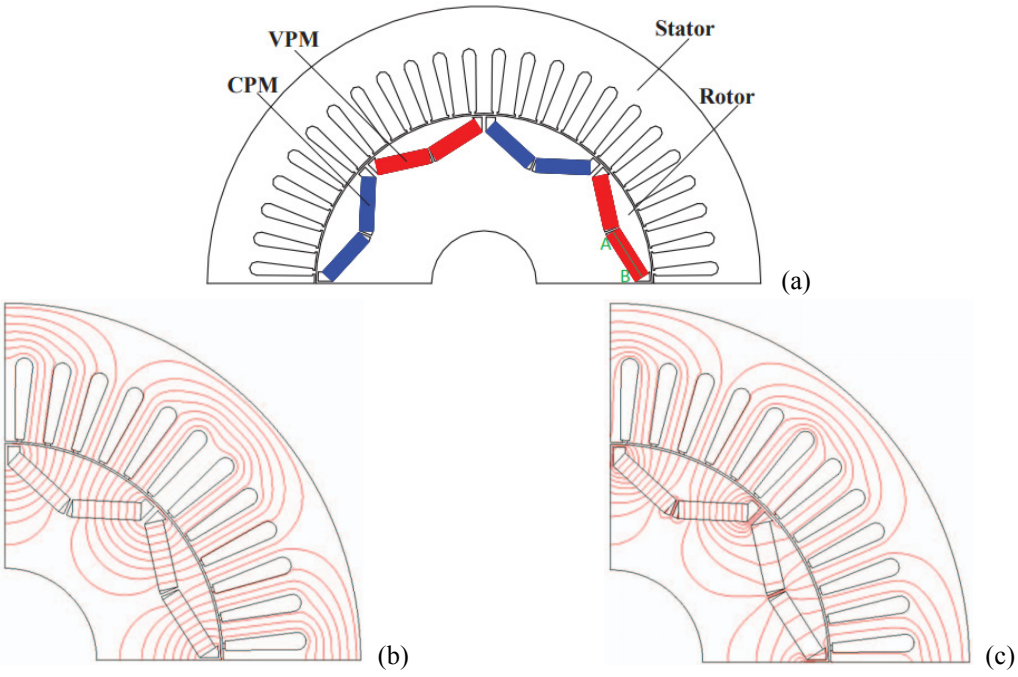

Fig. 1-12: (a): A hybrid AC-excited MM with variable and constant flux magnets in the rotor magnetically in series, (b): open circuit field distributions in fully forward magnetization states, and (c): open circuit field distributions in reverse magnetization states [34].

A hybrid AC-excited MM with series magnets is proposed in [34] as shown in Fig. 1-12. In this design, the variable magnet (VPM in the figure) is used to enhance or reduce the magnetic flux of the rare-earth magnet with constant magnetic flux (CPM in the figure). The open circuit field distributions of this machine while the VPM magnetized in the same direction and opposite to the CPM are shown in Fig. 1-12(b) and Fig. 1-12(c), respectively. According to the field pattern, CPM and VPM are in series magnetically. In this design, the CPM flux can assist the VPM to withstand unintentional demagnetization, and harmful cross-coupling is greatly alleviated. The magnetic field of the high coercivity magnet is added to the low coercivity magnet by making the magnetization direction of the high coercivity magnet into the direction of the low coercivity magnet. Since the operating point on the demagnetizing curve for the low coercivity magnet is higher by the field, the amount of magnetic flux increases and the low coercivity withstands the de-magnetic field generated by load current [35].

A hybrid AC-excited MM with two magnetically in parallel magnets is presented in [35] as shown in Fig. 1-13(a).

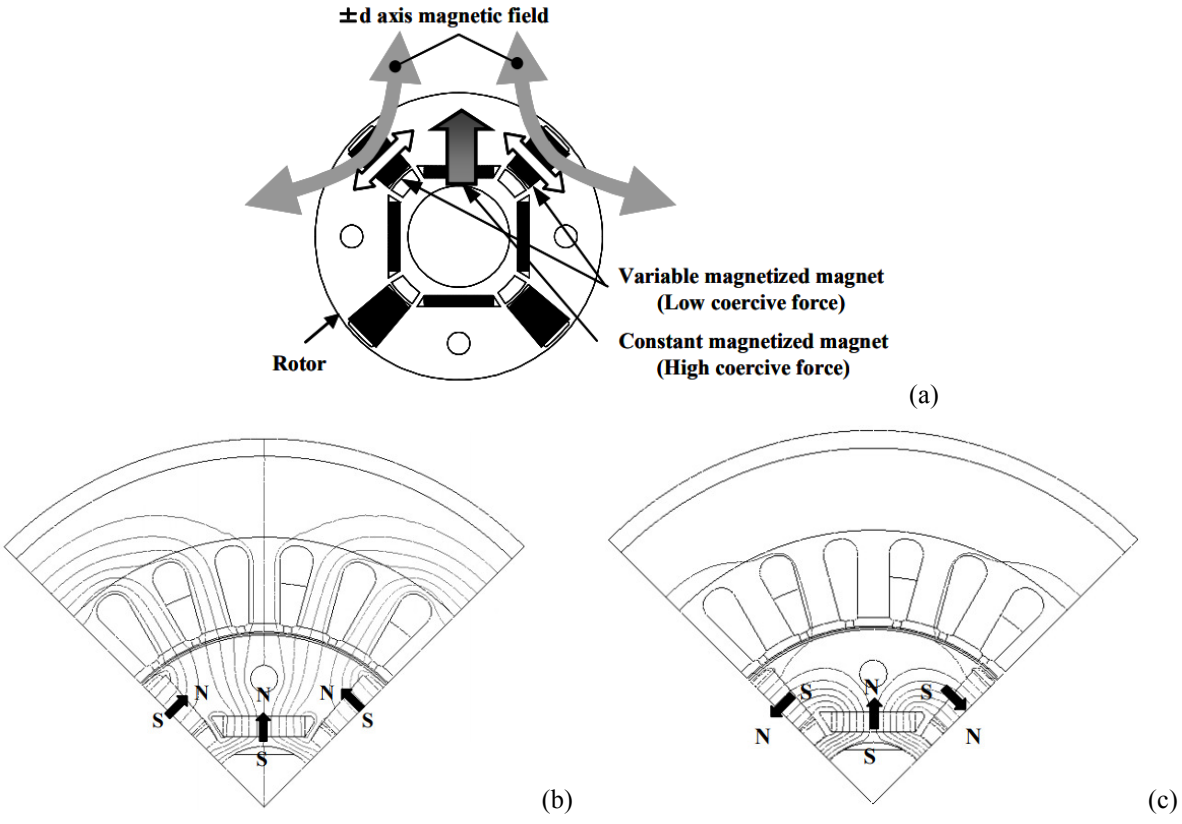

Fig. 1-13: (a): A hybrid AC-excited MM with two magnets in the rotor magnetically in parallel, and magnetic flux distribution at (b): maximum linkage flux, and (c): at minimum linkage magnetic flux [35].

In this machine also, the high coercivity magnets provide the main part of the output torque and the low coercivity magnets flux enhance or reduce the flux linkage of the machine to provide a better field-weakening capability. Fig. 1-13(b) and (c) show the maximum and minimum linkage flux patterns in this machine, respectively. The high and low coercivity magnets are located on the same rotor pole. However, the cross-coupling between the two types of magnets is severe in parallel hybrid AC-excited MM, in which the high coercivity magnets tend to automatically demagnetize the low coercivity magnets [36]. With a parallel magnetic circuit, the total amount of magnetic flux of the magnets becomes the sum of the low coercivity magnet and the high coercivity magnet. Therefore, the variation range of the total magnetic flux can be enlarged. If the polarity of the low coercivity magnet is reversed especially, variation range of the total magnetic flux will be doubled [37]. All the VFMs that have been reviewed in the previous sections are rare-earth based PMSMs or hybrid PMSMs which employ both rare-earth and low coercivity magnets. The low coercivity magnet based PMSMs are not popular due to the high demagnetization risk of the magnets. This type of VFM is proposed in [38]-[43]. A pure low coercivity magnet based AC-magnetized MM was first put forward by V. Ostovic to achieve an extended field-weakening region [38]. The rotor of the proposed MM is built as a sandwich of the trapezoidal AlNiCo magnets, electrical steel, and non-magnetic material, all of which are fixed to a non-magnetic shaft. Memory motors usually require an oversized inverter, as the inverter should be able to re-magnetize the magnets with an armature *d*-axis current pulse. A cross-sectional view of a four-pole MM is shown in Fig. 1-14. Tangentially magnetized PMs with N-poles (red) and S-poles (blue) drive flux Φ_{max} through the air gap into the stator. In addition, the leakage magnet flux near the shaft reduces the air gap flux density [38], which results in a reduction of the machine torque density.

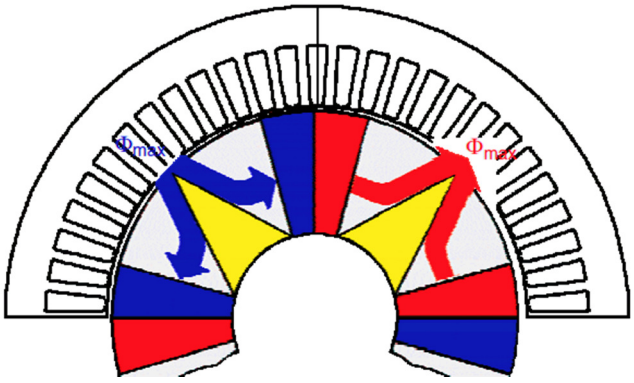

Fig. 1-14: Cross-sectional view of a fully magnetized memory motor [38].

Also, low coercivity magnets that are used in these machines type are normally susceptible to demagnetization. In VFMs with $L_d<L_q$, due to their large L_q, the magnetic field produced by I_q at high-load conditions can unintentionally cause partial demagnetization in the magnets, preventing the maximum torque capability to be achieved. The flux-intensifying designs of VFMs, characterized with $L_d>L_q$, can be employed to reduce the influence of the field-weakening operation (negative I_d), load current effect (I_q) and control the magnetization state stably at high-load conditions [39]. In the flux-intensifying designs, the magnetization of the magnets can be in radial or tangential directions.

Radially magnetized pure low coercivity magnet MM are proposed in [39], [40]. A design approach for a VFM using low coercivity magnets for improved efficiency and extended operating speed range is proposed in [39]. Fig. 1-15 shows a modified rotor structure [39].

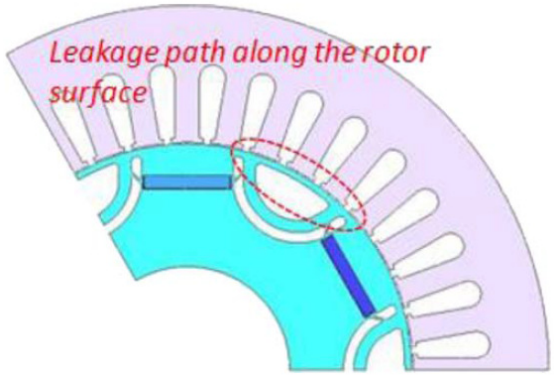

Fig. 1-15: Modified rotor structure with a connecting surface bridge [39].

By adding an additional iron bridge that connects between rotor poles along the rotor surface, a path for magnet leakage flux is formed. The flux barriers in the rotor are particularly designed to obtain another flux-varying capability, and force the armature q-axis flux to rotate in the leakage path to prevent it to go through the low coercivity magnet and demagnetize it. The designed machine shows benefits in increasing efficiency and speed range in the low-torque region.

In radially magnetized PMSMs, the spatial distribution of the stator magneto motive force (MMF) is sinusoidal along the rotation direction, so the flux produced by the magnets will be intensified at the front edge and weakened at the rear edge due to the q-axis flux produced by armature current, leading to a low torque density. This can be avoided by designing the machine with a smaller magnet arc, which leads to a reduction in the machine torque density.

The tangential magnetized design consideration for low coercivity magnet-based VFMs are proposed in [41]-[43]. Therefore, the magnet length can be increased to achieve a higher air gap flux density without exposing the magnets to a demagnetizing field. The armature *q*-axis flux primarily passes along the magnet face instead of going through the magnets as in conventional radial designs. In addition, the magnet length is uniformly exposed to the armature *d*-axis flux. This facilitates the demagnetization and magnetization processes.

A spoke type design of AlNiCo-based VFM is proposed in [34] and shown in Fig. 1-16.

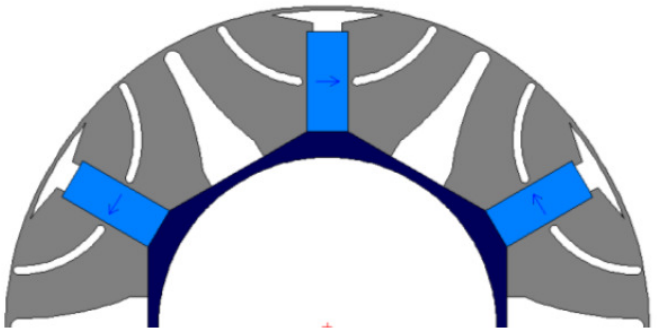

Fig. 1-16: AlNiCo–based VFM with tangential magnetization [42].

Some design considerations are taken into account in this machines to make them more efficient and robust against the magnet partial demagnetization. The un-even air gap length is a way to reduce the no-load back-EMF harmonics and the torque ripple as presented in [41]-[43]. Moreover, the *d*-axis barriers are curved to increase the reluctance of the *q*-axis flux pass which at the same time reduces L_q. The small barriers are added also to increase the saliency ratio and as a result, the torque density of the machine [41]-[43]. To reduce the leakage flux below the magnet, a pair of barriers are inserted below the magnet in [41]. This problem is solved using a non-magnetic hub to connect the rotor core and shaft as reported in [41]-[43]. In addition, an air rib is curved above the magnet to prevent the flux circulation above the magnet and control the pole arc angle as reported in [41]-[43].

1.2.4 Summarizing Different Topologies of Variable Flux Machine

To summarize different categories of VFMs, Table 1-1 shows the drawbacks and benefits of different designs of the VFMs. According to Table 1-1, with the hybrid excitation, and the auxiliary DC coils, the design will be more complicated and at the same time, the control strategy is more intricate. Although, the rotor structure is simple with the DC coils in the stator,

the effects of the DC coils on the machine performance should be analyzed. Moreover, with the DC coils in the rotor, the slip rings and the related problems will be the weak points of the design. The hybrid excitation has negative effects on the torque density of machine. Additionally, the DC coils increase the risk of the rare-earth magnets demagnetization. Both Ohmic and core losses related to the DC coils should be considered and the probability of any short-circuit in the DC coils and its impact on the machine performance should be analyzed.

The mechanical adjustments to control the flux linkage of the machine make the machine structure as well as the control strategy more complicated.

For the VFMs with hybrid magnets, the effects of the high coercivity magnets on the low coercivity magnets and the magnetization and demagnetization procedures should be considered. All the designs that have rare-earth magnets, suffer from the high price fluctuations of these strategic materials. For the pure low coercivity magnet VFMs, the torque density, specifically at field-weakening mode of operation as well as the magnetization and demagnetization procedure should be taken into the account in more depth. Moreover, this family of VFMs does not have the problems related to the hybrid excitation and high coercivity magnets. However, the magnets partial demagnetization in the loaded conditions should be checked.

Table 1-1. Different topologies of variable flux machines, drawbacks and benefits.

<table>
<tr><td colspan="3">Pure Rare-Earth Magnet</td></tr>
<tr><td rowspan="2">Hybrid-Excited</td><td>Series Flux Pass</td><td>[9]-[13]
• Generally simple structure
• Good Flux regulation capability
• High risk of the magnet demagnetization
• Low torque density as a result of hybridization
• More loss related to DC excitation
• Slip ring and its related problem with DC coils in the rotor
• Dependency on the rare-earth magnets
• Complicated control strategy</td></tr>
<tr><td>Parallel Flux Pass</td><td>[15]-[28]
• Good Flux regulation capability
• No risk of the magnet demagnetization
• High torque density
• Complicated structure to prototype and analyze
• More loss related to DC excitation
• Slip ring and its related problem with DC coils in the rotor
• Dependency on the rare-earth magnets
• Complicated control strategy</td></tr>
<tr><td>Mechanical Adjustment</td><td colspan="2">[29]-[31]
• Good Flux regulation capability
• No risk of the magnet demagnetization
• Low torque density and complicated structure to prototype and analyze
• Dependency on the rare-earth magnets and complicated control strategy
• Higher weight as a result of the additional mechanical parts</td></tr>
<tr><td colspan="3">Low Coercivity Magnets, (Memory Machines)</td></tr>
<tr><td>Hybrid-Excited</td><td colspan="2">[32], [33]
• Good Flux regulation capability
• More loss related to DC excitation
• Slip ring and its related problems with DC coils in the rotor
• Dependency on the rare-earth magnets
• Complicated control strategy</td></tr>
<tr><td rowspan="2">AC-Excited</td><td>Hybrid Magnets</td><td>[34]-[37]
• Good Flux regulation capability
• Dependency on the rare-earth magnets
• Problems related to the low coercivity material demagnetization procedure
• More loss related to DC excitation
• Slip ring and its related problem with DC coils in the rotor
• Complicated structure and control</td></tr>
<tr><td>Pure Low Coercivity Magnets</td><td>[38]-[43]
• Good Flux regulation capability
• Independency into the rare-earth magnets
• Simple structure
• Complicated control strategy
• A risk of low coercivity demagnetization
• Low torque density specifically at field-weakening operation</td></tr>
</table>

1.3 Problem Statement

There is currently wide interest in the research and development of "green" traction application driven by electrical machines, such as hybrid and electric vehicles. PMSMs are one the most favorite electrical machine choices because of their high torque density.

A high performance of electrical machine for a wide range of operating condition (torque and speed) is one of the essential features for electrical machines in transportation. This affects the driving range of the vehicle and its battery size. It means with a certain battery size, a motor with higher efficiency can provide a longer driving range.

The high price fluctuation of the rare-earth magnets (as mentioned in section 1.1.1), as well as the low efficiency in the field-weakening mode of operation (as addressed in 1.1.2) are the big concerns in the application of rare-earth PMSMs in industry specifically for transportation electrification. VFMs with AlNiCo magnets are one of the alternatives to solve both of the mentioned problems.

Low coercivity of AlNiCo magnets enables this type of VFM to have higher efficiency and at the same time increases the complexity of the design procedure. The magnet flux control during the magnetization and demagnetization procedures should be studied. An analytical model, and a new analytical design criterion are necessary to have a better understanding of the design procedure. Moreover, an existing AlNiCo-based VFM, and its experimental characterization reveals the drawbacks of the existing machine such as high torque ripple, low torque and power in the field-weakening mode of operation.

1.4 Motivation and Objectives

In order to analyze the spoke type VFM and to improve its design procedure, an analytical model of this machine is necessary. This analytical model should be simple, fast and at the same time should be close to the real machine considering the stator slot effect, and uneven air gap length. Besides, a new design criterion using the analytical model will be developed to design the VFM.

The characterization of the existing AlNiCo-based VFM can provide a better understanding on the benefits and drawbacks of this machine. As the proposed VFM has the ability to work at different magnetization levels, it should be characterized at different magnetization levels. The magnetization and demagnetization procedures needs to be studied both experimentally and

analytically to understand the properties of the efficient magnetization and demagnetization procedures.

Moreover, according to the characterization results, the high torque ripple and magnetization current of the existing spoke type VFM proves the necessity of the design optimization to minimize the torque ripple and magnetizing current of the VFM.

The issue of the decreasing torque and power of the existing VFM in the field-weakening is tackled in this study by designing a new topology of the VFM.

Core losses in electrical machines have a great role in the performance analysis. Core loss measurement and segregation from the other rotational loss components are big concerns. This research will focus on the no-load and loaded core losses of the existing VFM, its measurement and segregation from other components of rotational losses, as well as a method to estimate it.

1.5 Contributions

The followings are the technical output of the presented research work in this thesis.

Journal Papers

1. A. Takbash, M. Ibrahim and P. Pillay, "Design Optimization of a Spoke Type Variable Flux Motor Using AlNiCo Permanent-Magnet for Electrified Transportation", in *IEEE Transactions on Transportation Electrification,* doi: 10.1109/TTE.2018.2817120.
2. A. Takbash, and P. Pillay, "Magnetization and Demagnetization Energy Estimation and Torque Characterization of Variable-Flux Motor", accepted in *IEEE Transactions on Energy Conversion*.
3. A. Takbash, M. Ibrahim, L. Masisi and P. Pillay, "Core Loss Calculation in a Variable Flux Permanent Magnet Machine for Electrified Transportation", accepted in *IEEE Transactions on Transportation Electrification.*

Conference Papers

1. A. Takbash and P. Pillay, "Magnet Design Consideration of a Variable-Flux PM Machine," Accepted for *2016 IEEE Energy Conversion Congress and Exposition (ECCE), Cincinnati, OH,* 2017.
2. A. Takbash and P. Pillay, "Design Optimization of a New Spoke Type Variable-Flux Motor Using AlNiCo Permanent-Magnet," *IEEE International Electric Machines & Derive Conference (IEMDC), Miami, FL,* 2017.
3. A. Takbash, M. Ibrahim and P. Pillay, "Torque ripple reduction of a variable flux motor," *2016*

IEEE Energy Conversion Congress and Exposition (ECCE), Milwaukee, WI, 2016, pp. 1-7.

4. A. Takbash and P. Pillay, "An analytical model for a spoke type variable flux permanent magnet motor in no-load condition," *2016 IEEE Energy Conversion Congress and Exposition (ECCE)*, Milwaukee, WI, 2016, pp. 1-6.
5. A. M. Takbash and P. Pillay, "A modified analytical method for core losses calculation in magnetic laminations for a wide range of frequency and flux density," *2015 IEEE International Electric Machines & Drives Conference (IEMDC)*, Coeur d'Alene, ID, 2015, pp. 1109-1114.
6. L. Masisi, A. Takbash and P. Pillay, "Core loss performance of a new PM machine topology for electric vehicles," *2015 IEEE International Electric Machines & Drives Conference (IEMDC)*, Coeur d'Alene, ID, 2015, pp. 202-207.

1.6 Organization of Dissertation

Chapter 2 presents an analytical model for the spoke type VFM. In this chapter, the main principals of the VFM are discussed, and the analytical model of a spoke type VFM based on an equivalent magnetic circuit of the machine is presented. The effect of stator slots and uneven air gap on the air gap magnetic flux density are modeled. The analytical estimation of the no-load back-EMF, and magnetization current, as well as torque characteristics, are presented. The analytical model is then validated by the FE model results.

An optimization procedure is developed in Chapter 3 to reduce the torque ripple and magnetization current of the existing VFM. A complex multi-objective optimization problem is transferred to a two-level optimization procedure to reduce the torque ripple, and the magnetization current, and to keep the torque mean value within an acceptable range. Moreover, the no-load operating point of the magnet must be considered during the optimization procedure. The optimized design in the chapter is compared with the existing design.

Chapter 4 focuses on the existing design of spoke type VFM with inverted saliency to extract its torque-speed and power-speed characterizations considering the AlNiCo magnet demagnetization. Moreover, a new design of AlNiCo-based radially magnetized VFM with conventional saliency is proposed to keep the promising features of the existing design and enhance the power and torque capabilities of the VFM in the field-weakening region. Moreover, the design is optimized to have minimized torque ripple, and at the same time maximized power and torque capabilities.

Chapter 5 presents the characterization of the existing spoke type VFM at different

magnetization levels. A method is proposed to calculate the required energy for the magnetization and demagnetization of AlNiCo magnets in an existing VFM. A test procedure is also developed to measure the required magnetization and demagnetization energy using the applied current and voltage pulses. The torque performance of the VFM at different magnetization levels is analyzed in this chapter. The test results are compared with the finite element (FE) results to evaluate the effect of magnetization level variations on the torque characteristics. Besides, an analytical method is implemented into the FE model to estimate the core loss of the machine. The core loss is measured experimentally and the proposed method is verified.

Chapter 6 concludes the thesis and proposes the suggested future research.

Chapter 2. Analytical Modeling of the Spoke Type Variable Flux Machine

2.1 Introduction

An analytical model is a powerful tool for the design of electrical machines. It can be iterated to predict the effect of various geometrical parameters on the machine performance, without running FE software. That means a more accurate initial FE model that reduces the design time.

In this chapter, after a brief literature review on analytical modeling of PMSMs, the main principals of the VFM such as the magnet flux control, magnet direction selection, and the general dimensions of the existing VFM are discussed. Moreover, an analytical model of a spoke type VFM based on an equivalent magnetic circuit of the machine is presented. By applying the magnetic equations in the equivalent circuit, the no-load air gap magnetic flux density is calculated. The effect of stator slots on the air gap magnetic flux density is considered and the uneven air gap length is also modeled. The analytical estimation of the no-load back-EMF is presented. A new analytical approach of estimating of magnetization current is proposed. The peak to peak value of the electromagnetic torque of the machine is calculated analytically. The analytical model is then validated by the FE model results.

2.2 Review of Analytical Modeling Methods of Electrical Machines

Various analytical modeling methods have been developed for electrical machines such as *d-q* model, winding function modeling method, lumped parameter modeling, and magnetic equivalent circuit. Nowadays, PMSMs are the preferable alternative in different applications, and as a result, analytical modeling of PMSMs has been recently the subject of research.

A simple method is introduced in [44] to select the magnet shape and dimensions in order to minimize key harmonic components in the machine. The analysis focused on commonly used rotor structures such as rectangular, stepped, and trapezoidal and the model results are verified with test and FE model. The air gap flux density for a trapezoidal magnet is calculated from (2-1) in [44] as

$$B_g(x) = \frac{\mu_0}{(h_m + \delta)} \sum_{n=1,3,\ldots}^{\infty} \left\{ {}^{4H_c h_m}/_{\pi n} \right\} \sin\left({}^{n\pi}/_{2}\right) \sin\left({}^{n\pi x}/_{\tau}\right) \frac{\cos\left({}^{n\pi\alpha_{p2}}/_{2}\right) - \cos\left({}^{n\pi\alpha_{p1}}/_{2}\right)}{\left({}^{n\pi}/_{2}\right)(\alpha_{p2} - \alpha_{p1})} \qquad (2\text{-}1)$$

where h_m, δ, H_c, τ, and α_p are the magnet height, air gap length, magnet coercive field strength, pole pitch, and embrace, respectively.

An analytical technique for predicting the instantaneous magnetic field distribution in the air gap region of radial-field topologies of brushless DC (BLDC) PMSMs, under any specified load condition was developed in [45]-[48]. This technique implicitly accounts for the stator winding current waveform, and the effect of stator slot-openings. The analytical technique is based on the superposition of the field components related to the magnet and the stator excitation. [45] presented a two dimensional (2D) analytical method for predicting the no-load air gap field distribution in both internal and external rotor radial-field motor topologies. This method solves the Laplacian/quasi-Poissonian field equations in polar coordinates, in the annular air gap/magnet region of a multi-pole slot-less motor. The field vectors, $\vec{B}$, and $\vec{H}$ are coupled by [45]

$$\vec{B}_I = \mu_0 \vec{H}_I \quad in\ the\ air\ gap; \qquad (2\text{-}2)$$

$$\vec{B}_{II} = \mu_m \vec{H}_{II} + \mu_0 \vec{M} \quad in\ the\ magnet; \qquad (2\text{-}3)$$

where $\vec{M}$ is the residual magnetization vector, $\mu_m = \mu_{rec}\mu_0$ is the magnet permeability, and μ_{rec} and μ_0 are the relative recoil permeability of the magnet, and air permeability, respectively. In terms of scaler magnetic potential φ can be expressed as [45]

$$\nabla^2 \varphi_I = 0 \quad in\ the\ air\ gap; \qquad (2\text{-}4)$$

$$\nabla^2 \varphi_{II} = \frac{div\vec{M}}{\mu_r} \quad in\ the\ magnet. \qquad (2\text{-}5)$$

The definition of $\vec{M}$ is dependent on the magnet orientation. The magnetic flux distribution in all parts of the machine can be calculated analytically, considering the general solution for the scalar magnetic potential distribution in the air gaps and magnets, and the boundary conditions in different parts of the machine. Fig. 2-1 depicts the magnetic flux density distribution at the stator surface of 6-pole and 12-pole machines using both analytical and FE models.

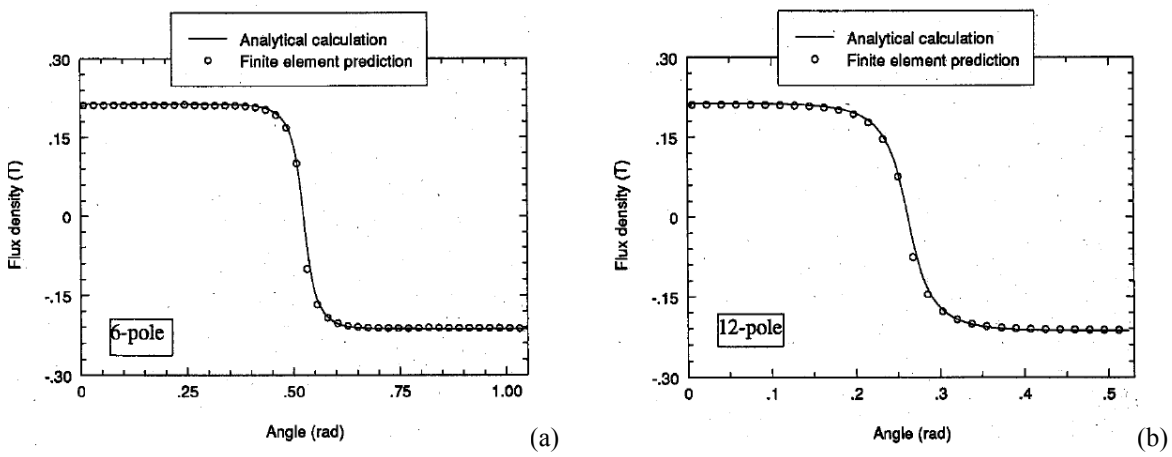

Fig. 2-1: Magnetic flux distribution at the stator surface (a) 6-pole (b) 12-pole [45].

This analysis is extended to the prediction of the armature reaction field produced by the 3-phase stator windings in [46]. As before, the motor model is formulated in polar coordinates to consider the effects of winding current harmonics on the air gap field distribution. The current sheet is distributed such that the current density is uniform along an arc whose length is equal to the slot opening, b_0. The current density distribution is given by [46]

$$J = \begin{cases} \dfrac{i}{b_0} & -\dfrac{b_0}{2R_s} \le \alpha \le \dfrac{b_0}{2R_s} \ \ (over\ the\ slot\ opening) \\ 0 & other\ \alpha \ \ (elsewhere) \end{cases}. \tag{2-6}$$

Considering the effects of stator current, the flux density distribution now has a stepped rectangular waveform.

A method for modeling the effect of the stator slotting on the magnetic field distribution in the air gap/magnet region of the above mentioned BLDC motor is presented in [47]. This enhances the analytical prediction of the open-circuit, armature-reaction, and resultant magnetic field distribution under any specified load condition. The conventional one dimensional (1D) relative permeance model, which is used extensively in the analysis of induction motors and synchronous machines, is inappropriate for PMSMs and a 2D relative permeance function is required. When the stator is slotted, an appropriate Carter's coefficient (K_c) can be included to model the reduction in flux per pole. In the calculation of the field produced by the magnets, the air gap length (g), and stator inner radius (R_{si}) are replaced with g_e, and R_{se} that can be defined as [47]

$$g_e = g + (K_c - 1)\, g' \tag{2-7}$$

$$R_{se} = R_{si} + (K_c - 1)\, g' \tag{2-8}$$

where $g' = g + {}^{h_m}/_{\mu_r}$ is the effective air gap length of the machine.

In [48] the 2D field analysis, in polar coordinates, combines the armature reaction field component, derived from an analytical prediction of the current waveform, with the open circuit field component produced by the magnets. The resultant field can be predicted under any commutation strategy through the analytical determination of the relative temporal and spatial position of the two field components. These analyses are combined in accordance with the time variation of the relative permeance and the back-EMF, and current waveforms to enable the deduction of the resultant instantaneous magnetic field under any load condition and commutation strategy.

[49] presents an analytical method for the computation of open circuit air gap flux density, armature reaction, and on load magnetic field distribution in integer slot winding parallel double excitation and spoke type tangential PMSMs. A 2D exact analytical model of the magnetic field distribution based on the solution of Laplace's and Poisson's equations is established and the results are verified using the FEA solutions. Fig. 2-2 shows the machine model and the boundary conditions of the magnet, where region I represents the air gap, region II the magnets, regions III and V the stator semi-closed slots, region IV a nonmagnetic material under magnets, region VI the rotor slots at the top of permanent magnets, and regions VII and VIII the rotor excitation semi-closed slots.

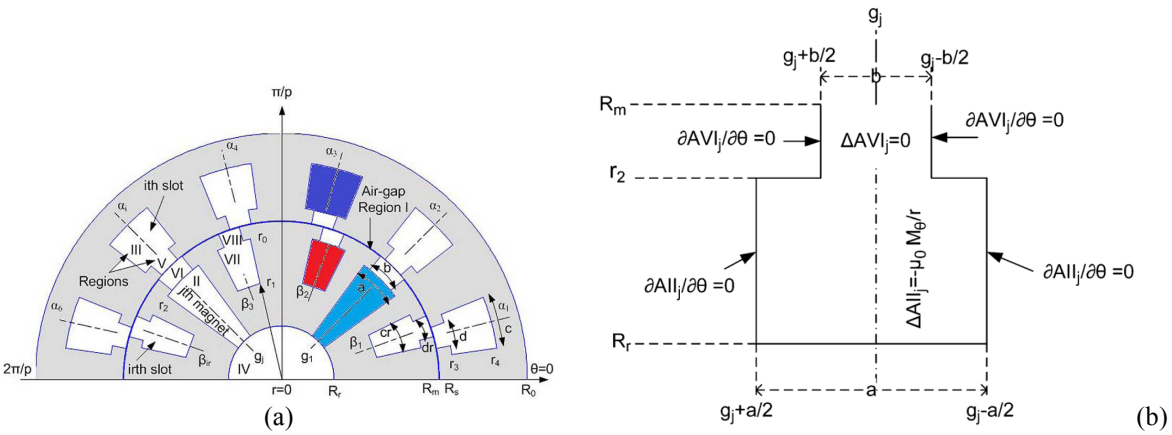

Fig. 2-2: Simplified model of (a): machine, and (b): boundary conditions of rotor slot [49].

The model is formulated in vector potential and 2D polar coordinates. In order to calculate the armature reaction, on load and rotor double excitation magnetic field distribution, the stator

current density in slots is defined by a matrix connection between phase current and stator slots [49]. The number of harmonics is defined carefully, in addition to a proper scaling of the machine model dimensions for good results and to prevent the solution from diverging [49]. When the number of harmonic terms increases, the system of equations written in matrix form becomes ill-conditioned and the solution becomes inaccurate. This problem has been reduced in [49] by including proper scaling down of the machine model dimensions in the radial direction for all regions as

$$r_{scale} = r_{real} 10^{xc}. \tag{2-9}$$

The *xc* is considered to be equal to 1.45 in [49]. This problem, along with the technical complexity are the main drawbacks of this method.

An analytical model of the spoke type motor is established in [50] and the associated Laplace's equations of magnetic scalar potential, and a series of boundary conditions are given. The analytical expressions of the magnet field strength and the flux density in the air gap produced by Ferrite magnets are obtained. The flux density in the air gap region is derived on the basis of equivalent air gap permeance calculation by considering the stator slot opening. Finally, the air gap field distribution and back-EMF of the spoke type machine is analyzed. Fig. 2-3 shows the distributions of flux density in the air gap of the proposed PMSM [50].

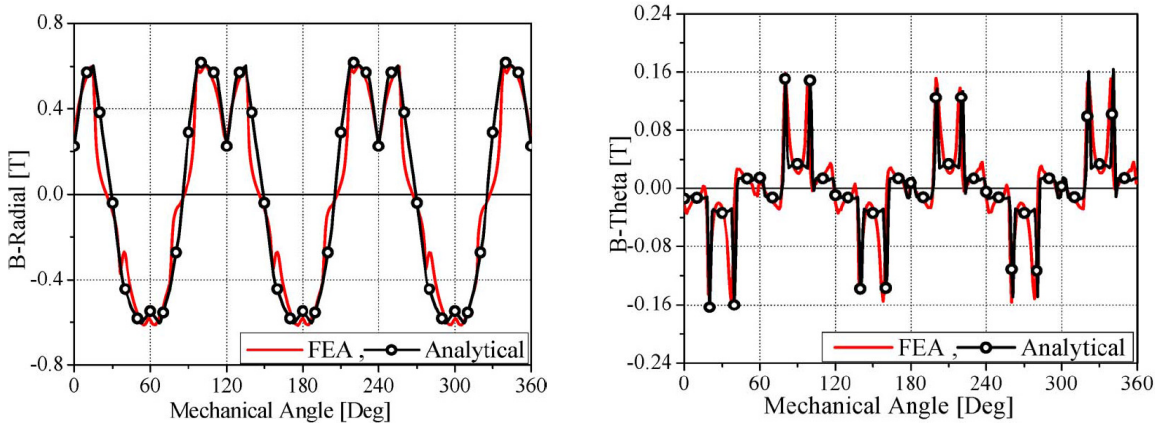

(a) (b)

Fig. 2-3: Result of (a) radial and (b) tangential flux density [50].

Another analytical method is presented in [51] for no-load magnetic field distribution calculation of a spoke type PMSM. The effects of the slots are considered. The air gap flux density distribution and the relative air gap permeance distribution are derived based on a

generalized analytical field solution by the conformal transformation.

The following conditions are assumed for the air gap field analysis [51]:

- The magnetic saturation may affect the magnitude of flux density in the air gap, but will not affect the distribution wave shape. Therefore, for air gap flux density wave shape analysis, the ampere-turn drops in the stator and rotor cores are negligible.
- The depth of the stator slots will not affect the air gap flux density wave shape. Therefore, the stator slots can be considered to be infinitely deep.

The analytical field solutions were used to predict the cogging torque of an 8-pole, 48-slot spoke type PMSM and compared with the FEA results as shown in Fig. 2-4 [51].

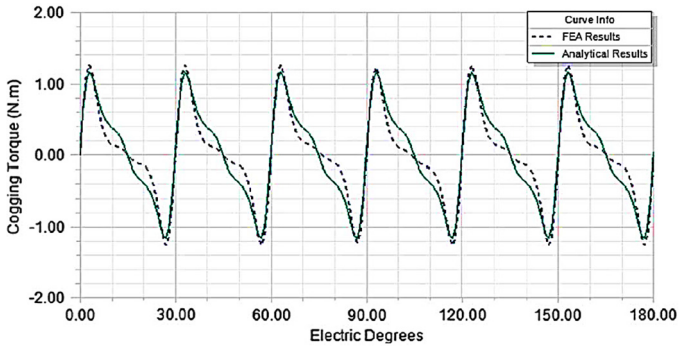

Fig. 2-4: Predicted cogging torque compared with the FEA results of the 8-pole, 48-slot spoke type PMSM [51].

[52] represents the analytical design criteria of a spoke type fractional slot concentrated winding (FSCW) IPMSM, especially with regard to some objectives like the minimization of the magnet volume, maximization of the air gap flux density, and optimization of the split ratio (rotor outer radius/stator back iron width). The constraints are the motor outer dimensions and the maximum copper losses. Optimal designs are achieved when the parameters are selected so as to remain along the maximum flux per magnet volume curve. Various slot/pole configurations are analyzed and compared in order to achieve general considerations about the motor design. Fig. 2-5 shows a simplified model of the flux density distribution in front of a stator tooth, at no load and under load operation.

[53] uses the geometrical and material data which makes it suitable for insertion into design programs, avoiding long FE calculations. The modeling procedure is based on the calculation of the air gap flux density waveform at every time step.

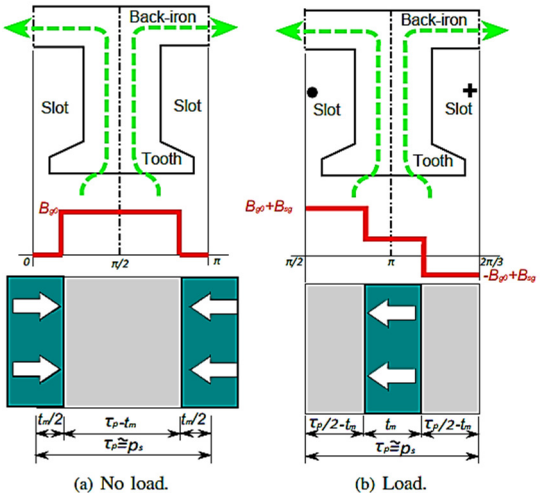

Fig. 2-5: Stator flux density distribution [52].

The waveform is the solution of the Laplacian/quasi–Poissonian field equations in polar coordinates in the air gap, and also accounts for slotting. Fig. 2-6 depicts a comparison of the total torque (comprising of both electromagnetic and cogging) calculated from FEA and the proposed analytical model [53]. Sinusoidal currents are used in the simulation and a torque angle of 30º is used to emphasize the ripple in the torque function.

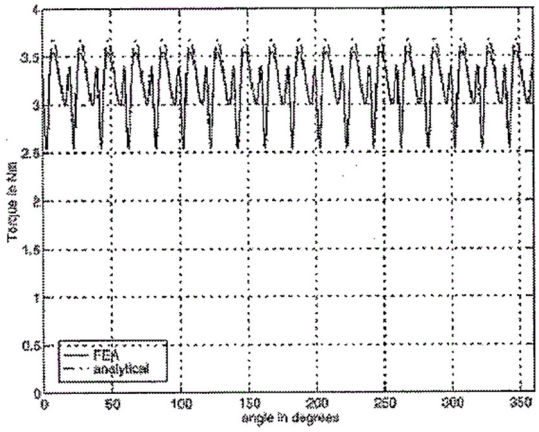

Fig. 2-6: Comparison with FEA for total torque [53].

The relative air gap specific permeance distribution function is derived in [54] considering the effect of slotting. Neglecting the iron saturation, and employing the analytical algorithm for partial differential equations, analytical calculations of no-load air gap magnetic field distribution, armature field distribution, and phase back-EMF, are demonstrated. Subsequently, based on the main circuit topology of a BLDC motor, the field circuit coupling model is developed for the motor, and then the phase current waveforms and the loaded air gap magnetic

field distribution at any instant of time are determined. The instantaneous electromagnetic torque is then computed from the current and the back-EMF. Fig. 2-7(a) presents the effect of the slot on the air gap flux density waveform. Fig. 2-7(b) shows the air gap relative permeance distribution at the center of the air gap.

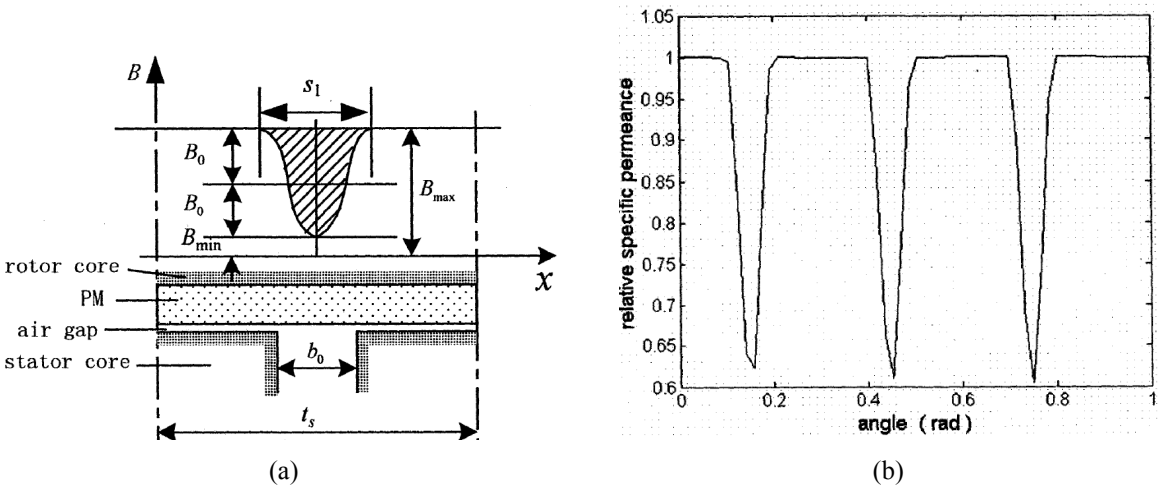

(a) (b)

Fig. 2-7: (a) Distribution of flux density within a tooth pitch and (b) air gap relative specific permeance distribution at center of air gap [54].

As described in this section, most of the analytical methods presented in the literature are based the on the solution of Laplacian/quasi-Poissonian field equations. This method is complex, even when only a small number of harmonics are considered in the analytical model. Another problem with this method is the definition of the boundary conditions. Moreover, when an analytical method is used in the design procedure, it should be fast and at the same time accurate to provide appropriate initial values for other steps.

2.3 AlNiCo Magnet Flux Variation

The low coercive force of AlNiCo magnets provides a unique feature of magnet flux control in the VFM. Fig. 2-8 shows the B-H loop of AlNiCo 9 magnet in the 1st and 2nd quadrants. In a PMSM, the operating point of the magnet at no-load condition can be estimated as the intersection of the air gap line (*PC* line) and the B-H loop in the 2nd quadrant (point A in Fig. 2-8). The slope of the air gap line, the permeance coefficient (*PC*), can be calculated as

$$PC = \frac{t_m A_g \mu_0}{g A_m} \tag{2-10}$$

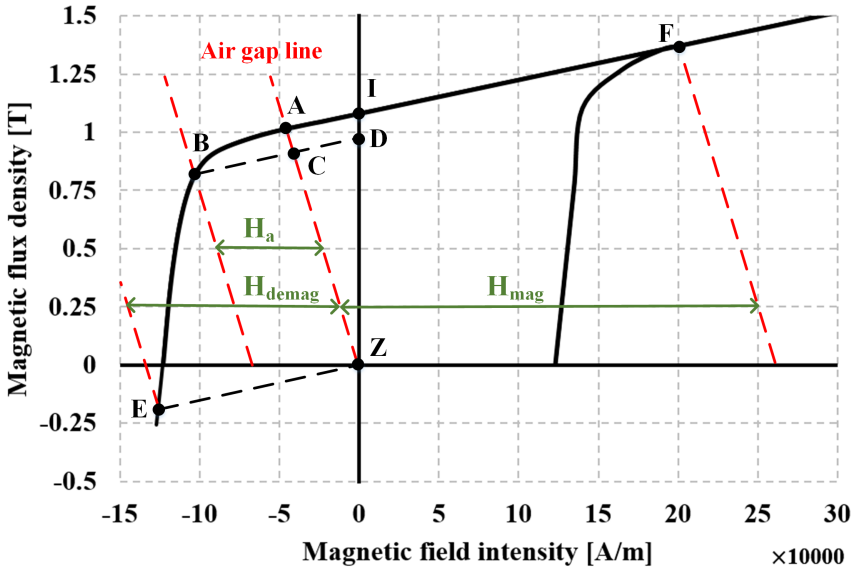

Fig. 2-8: B-H loop for AlNiCo 9.

where A_g, A_m, and g are the air gap and the magnet cross-sectional areas, and the air gap length, respectively. The no-load operating point of the magnet is a function of the magnet and air gap dimensions.

If the armature current produces the external magnetic field of H_a in the magnet, the operating point of the magnet will go to point B in the loaded condition that is below the knee point of the B-H loop in the 2nd quadrant. Once the current is removed, the magnet does not recoil on the same trajectory as the original B-H loop. It recoils on a line with the same slope (recoil permeability) as the linear part of the B-H loop to point C. In this condition, the remnant flux density of the magnet is D, which is less than the fully magnetized condition (I). The magnet is partially demagnetized as a consequence of the demagnetization effect of the armature current. The magnetization level (ML) of the magnet in this condition can be estimated as

$$ML\% = \frac{D}{I} \times 100. \tag{2-11}$$

Based on Fig. 2-8, and using (2-11), to go to each ML, the resultant magnetization or demagnetization current pulse could be estimated based on the external field that is needed. To demagnetize the magnet fully, the operating point of the magnet should be pushed to point E in the 3rd quadrant. To do this, an external demagnetizing field (H_{demag}) is required to be applied using the demagnetizing current (I_{demag}). After removing the demagnetizing current, the magnet recoils to point Z and will be fully demagnetized. To go from point Z to point F, and make the

magnet fully magnetized, an external magnetizing field (H_{mag}) should be produced by applying the magnetization current (I_{mag}). Once the magnetizing current pulse is removed the magnet recoils to point A and will be fully magnetized.

2.4 Existing Variable Flux Machine

The design, manufacturing, as well as the control of a spoke type VFM using AlNiCo 9 magnets, are proposed in [41]-[43]. The existing VFM is used in this chapter to develop the analytical model. To do this, the design principals and the basic dimensions of this design are first reviewed in this section.

2.4.1 Spoke Type Design

Due to the low coercive force of AlNiCo magnets, the armature current and its demagnetizing effect are one of the biggest concerns in the design of the AlNiCo-based VFMs. The armature MMF produces a field that demagnetizes the magnet rear edge in radial-flux design and causes partial demagnetization of magnets that reduces the torque density of the machine. To limit this effect, the magnet arc is reduced that also decreases the torque density of the machine. To solve this problem, a spoke type (tangentially magnetized) design is utilized. For a tangentially magnetized configuration, shown in Fig. 2-9(a), the *q*-axis flux primarily from the armature current passes along the magnet face instead of going through the magnets as in conventional radial designs. With the magnet length increase, the air gap flux density is enhanced without exposing the magnets to a demagnetizing field. In addition, the magnet length is uniformly exposed to the armature *d*-axis flux. This facilitates the demagnetization and magnetization processes. To do the magnetization and demagnetization as described in section 2.3, a chain of *d*-axis pulses is used to create the *d*-axis flux in the machine. For the demagnetization, the produced *d*-axis flux opposes the magnet flux, and for the magnetization, the produced flux enhances the magnet flux. Fig. 2-9(b) and (c) shows the rotor and stator of the prototyped spoke type VFM.

2.4.2 Design Specifications and Dimensions

The existing VFM is a 6-pole machine with 27-slot and fractional windings in the stator [42]. To develop the analytical model, some general dimensions in both rotor and stator as listed in Table 2-1 are required.

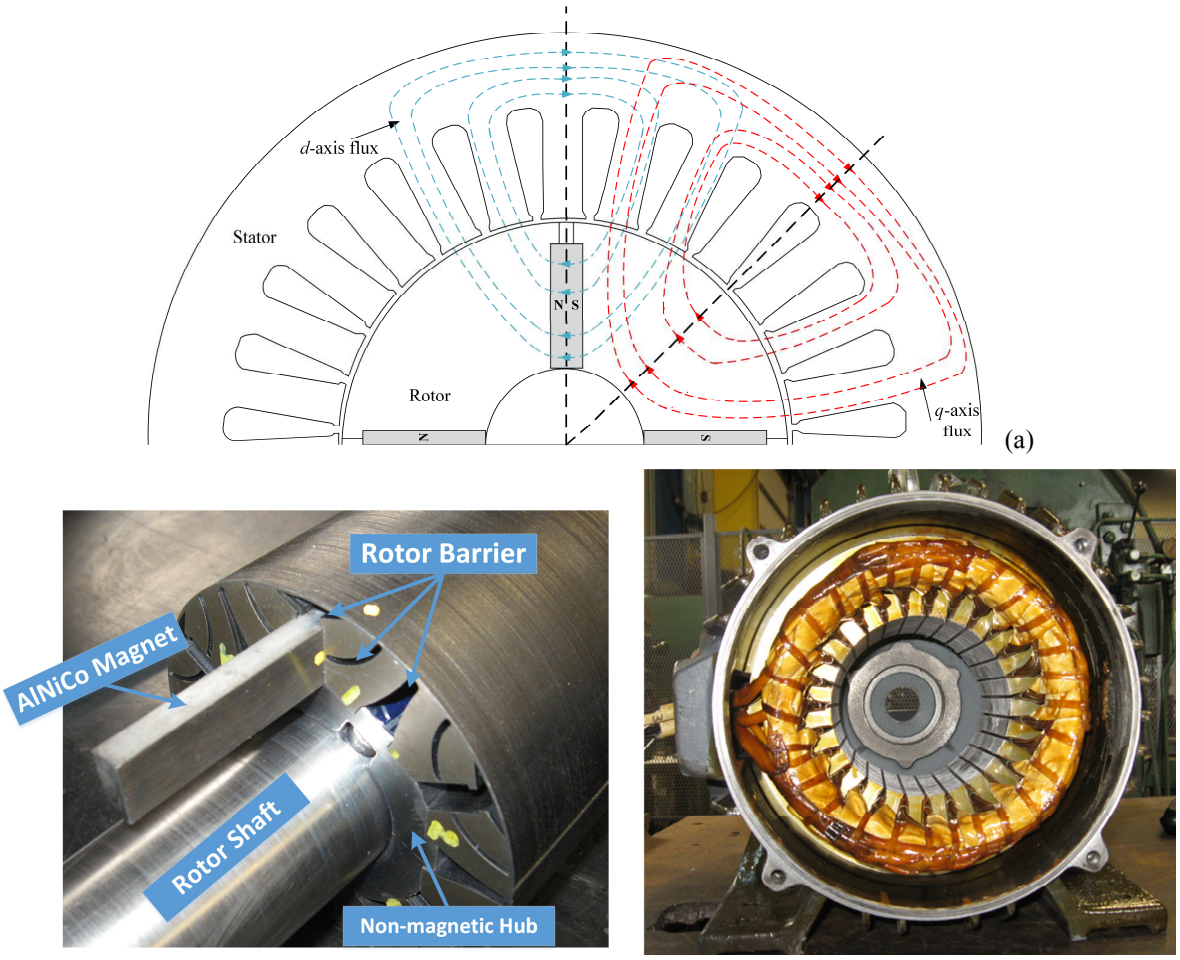

Fig. 2-9: (a): Illustration of *d*- and *q*- axes flux paths in tangentially magnetized PMSM, (b): Prototyped rotor, (c): prototyped stator of spoke type VFM.

Table 2-1. General dimensions of the existing variable flux machine.

Magnet length	14.2 mm	**Air gap length**	0.4 mm-0.75 mm
Magnet thickness	7 mm	**Rotor inner radius**	53.75 mm-54.1 mm
Rotor outer radius	54.5 mm	**Stack length**	120 mm

To have a more accurate analytical model, the effects of the stator slots and teeth should be taken into account. Fig. 2-10 shows the general overview of the prototyped stator lamination of the existing VFM [42].

2.5 Model Implementation

An analytical model based on the equivalent magnetic circuit of the spoke type PMSM is

proposed in this section. The following assumptions are considered in this model:

- The reluctance of iron is negligible.
- The B-H curve of the magnet is linear and the operating point is above the knee of the curve.
- The no-load air gap magnetic flux density (B_{go}) has a square wave distribution.

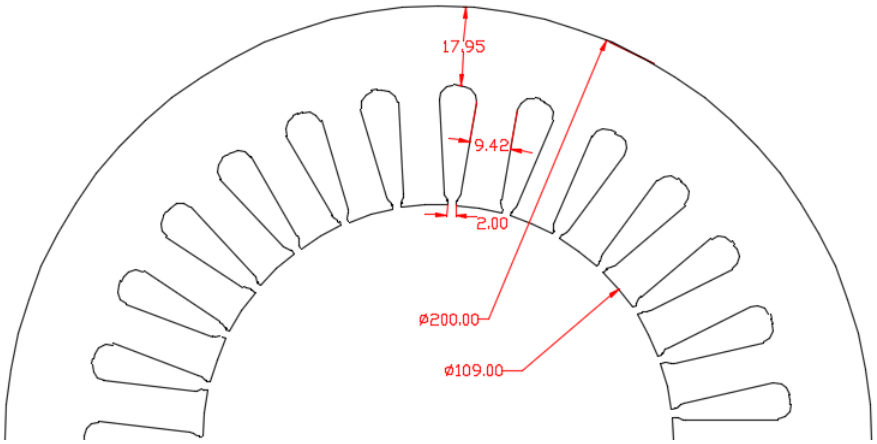

Fig. 2-10: Dimensions of the prototyped stator lamination [42].

Fig. 2-11 shows the equivalent magnetic circuit of the spoke type VFM. According to this figure, the spoke type PMSM can be transformed to an equivalent surface or inset PMSM.

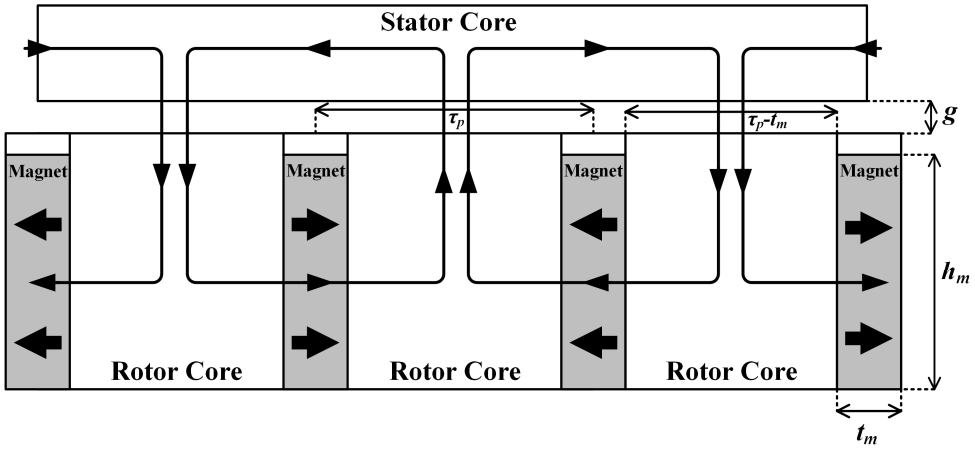

Fig. 2-11: Equivalent magnetic circuit of the spoke type VFM.

2.5.1 Air Gap Magnetic Flux Density in the No-load Condition for Slot-less Stator

The air gap magnetic flux density of the machine in the no-load condition can be estimated using Ampere's law in the flux path in Fig. 2-11, and the relationship between the air gap and the magnet flux density. Based on the equivalent model, the system of equations can be defined

as

$$\begin{cases} B_g A_g = 2B_m A_m \\ 2H_g g + H_m t_m = 2U_s \\ B_g = \mu_0 H_g \\ B_m = B_r + \mu_0 \mu_{rec} H_m \end{cases} \tag{2-12}$$

where H_g and H_m are the air gap magnetic field intensity and the magnet magnetic field intensity. U_s is the stator magnetic potential that can be calculated based on Ampere's law.

In this system of equations, the first equation shows the connection between the magnet and the air gap magnetic flux density. The second equation is driven based on the Ampere's law for the flux that links through the stator, the air gap, the rotor and the magnets. The last two equations show the relationship between the magnetic flux density with the field intensity in the air gap and magnets. A_g and A_m can be calculated as

$$A_g = (\tau_p - t_m) L_{stk} \tag{2-13}$$

$$A_m = h_m L_{stk}. \tag{2-14}$$

$\tau_p = (\pi R_{si}/P)$ is the pole pitch, where R_{si} is the stator inner radius and L_{stk} is the machine stack length. The definition of A_g in (2-13) depicts that no flux line leaves the magnet in the radial direction.

To calculate the air gap magnetic flux density in the no-load condition (B_{g0}), U_s should be considered as zero. Based on (2-12), (2-13), and (2-14), B_{g0} can be calculated as

$$B_{g0} = \frac{2B_r A_m}{(A_g + \frac{4g\mu_{rec} A_m}{t_m})}. \tag{2-15}$$

Fig. 2-12 depicts the no-load air gap magnetic flux density pattern for this machine. It is obvious from Fig. 2-12 that no flux line crosses on the top of the magnet radially to the air gap. Also, this figure shows the main idea of equivalent surface or inset machine that can be assumed for this machine. According to the no-load air gap magnetic flux density, the machine can be transformed to a surface machine with an equivalent magnet length of (τ_p-τ_m) and an equivalent magnet thickness that should be calculated based on the no-load air gap magnetic flux density. The main component of the square shape B_{g0} can be calculated using the Fourier transform as

$$B_{g01} = \frac{4}{\pi} \cos\left(k_m \frac{\pi}{2}\right) B_{g0} \tag{2-16}$$

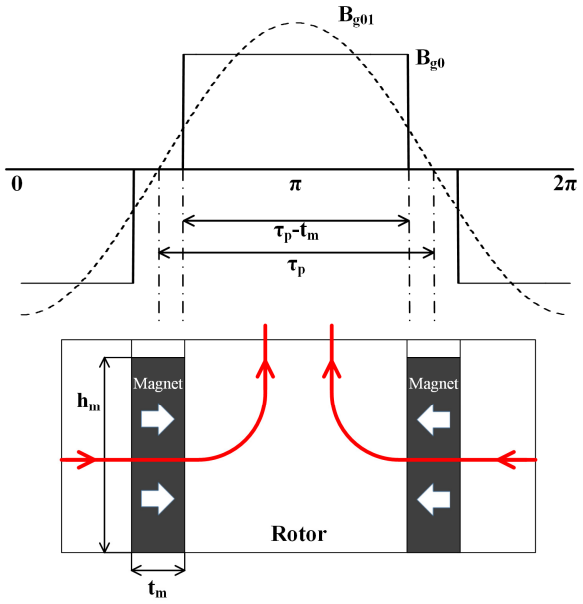

Fig. 2-12: The no-load air gap magnetic flux density pattern.

where $k_m = \frac{t_m}{\tau_p}$. Based on (2-15) and (2-16), the effect of t_m and h_m, on the air gap magnetic flux density at no-load condition can be studied.

The mean value of the torque as a result of the magnet ($T_{PM,mean}$) for a PMSM can be calculated analytically using

$$T_{PM,mean} = 3pK_dK_pK_sB_{go1}LR_roan_{tc}N_{spp}i_a \sin\theta \tag{2-17}$$

where a, n_{tc} and N_{spp} are the number of layers, number of turns for each coil and number of slot per pole per phase. For a 3-phase, 6-pole, and 27-slot VFM with 23 turns in each coil and double layer winding, these parameters are: $a=2$, $n_{tc}=23$, and $N_{spp}=1.5$. i_a and θ are the peak value of phase current and torque angle. K_d, K_p, K_s are the distribution, slot-pitch and skewing factors respectively which can be calculated as

$$K_d = \frac{\sin\left(\frac{N_{spp}\alpha}{2}\right)}{N_{spp}\sin\left(\frac{\alpha}{2}\right)} \tag{2-18}$$

$$K_p = \cos\left(\frac{\gamma_s}{2}\right) \tag{2-19}$$

where α is the slot pitch angle and γ_s is short pitch angle.

2.5.2 Effect of Stator Slots and the Uneven Air gap Length on the Air Gap Magnetic Flux Density

In the real machine, the stator slots cause variations in the effective air gap length of the machine, and as a result the air gap permeance. To enhance the accuracy of the analytical model, this effect should be considered. Fig. 2-13(a) depicts the equivalent model for the rectangular slot.

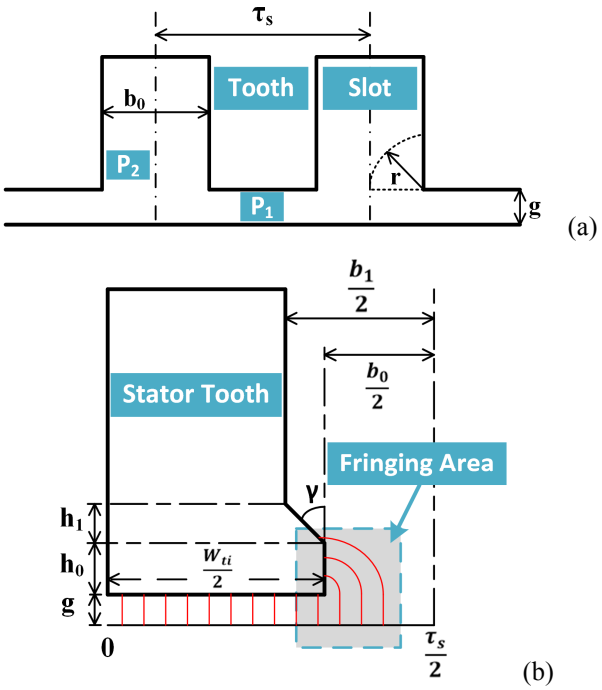

Fig. 2-13: The equivalent model for (a): rectangular slot, (b): trapezoidal slot with fringing.

Based on Fig. 2-13(a), two permeances can be defined for the air gap, one for the tooth area and the other for the slot area as [50]

$$P_1 = \frac{\mu_0(\tau_s - b_0)L_{stk}}{g} \tag{2-20}$$

$$P_2 = \frac{2\mu_0}{\pi}\int_0^{\frac{b_0}{2}} \frac{L_{stk}.dr}{\frac{2g}{\pi}+r} = \frac{2\mu_0 L_{stk}}{\pi}\ln\left(\frac{g+\frac{\pi b_0}{4}}{g}\right) \tag{2-21}$$

where b_o is the slot opening for the rectangular slot and τ_s is the slot pitch. Fig. 2-13(b) shows the flux line distribution for a trapezoidal tooth and slot. To have an accurate model, the fringing should be considered in the model. Fringing occurs because the air in the air gap and the slot area has the same permeability. Therefore, some flux will link through the fringe area as shown

in Fig. 2-13(b). Based on permeance and Fig. 2-13(b), the air gap length function can be defined as [50]

$$g(\theta)=\begin{cases} g & 0 \le R_{si}\theta \le \frac{w_{ti}}{2} \\ g+\frac{\pi}{2}R_{si}\theta & \frac{w_{ti}}{2} \le R_{si}\theta \le \frac{w_{ti}}{2}+h_0 \\ g+\frac{\pi}{2}R_{si}\theta+\gamma(R_{si}\theta-h_0) & \frac{w_{ti}}{2}+h_0 \le R_{si}\theta \le \frac{\tau_s}{2} \end{cases} \quad (2\text{-}22)$$

where w_{ti}, h_0 are tooth inner width and tooth tip thickness and γ is tooth tang angle that can be calculated by

$$\gamma=\frac{\pi}{2}-\tan^{-1}\left(\frac{h_1}{\frac{(b_1-b_0)}{2}}\right) \quad (2\text{-}23)$$

where b_1 and h_1 are the slot width and the tooth tip length, respectively. Based on (2-22), the actual air gap length increases as a result of fringing in the slot regions. The air gap length is maximum in the center of the slot and is constant for the tooth part and increases in the slot area up to the center of the slot and reduces again.

The gradual reduction of the air gap length produces more sinusoidal air gap flux density distribution. The air gap length of the variable flux machine is minimized at the *d*-axis (0.4 mm) and maximize at the *q*-axis (0.75 mm) to reduce the back-EMF harmonics. This is accomplished by shifting the pole arc center up towards the rotor surface [41]. In this way, the air gap length varies between g_{min} and g_{max}. This variation can be modeled either linear or non-linear. In the linear method, the air gap length between 0° to 30° changes linearly between 0.40 mm to 0.75 mm. In the non-linear method, the actual air gap length from the CAD sketch of the existing VFM is used.

Fig. 2-14 depicts the linear and non-linear variation of the air gap length with, and without slot effect consideration for the existing VFM. Based on Fig. 2-14(a), the minimum air gap length is 0.4 mm that occurs in 0, 60°, and 120° and the maximum air gap length is 0.75 mm that occurs in 30° and 90°. In Fig. 2-14(b) it can be seen that the stator slot has a greater effect on the air gap length than an uneven air gap length. The air gap length is maximum in the center of the slot and minimum in the center of the tooth. Based on (2-22) and (2-23), the air gap length in the middle point of the slot depends on the slot width, slot opening, and tooth tip thickness. In this case, the air gap length in the middle of the slot is 37 times greater than the air gap length in the middle of the tooth.

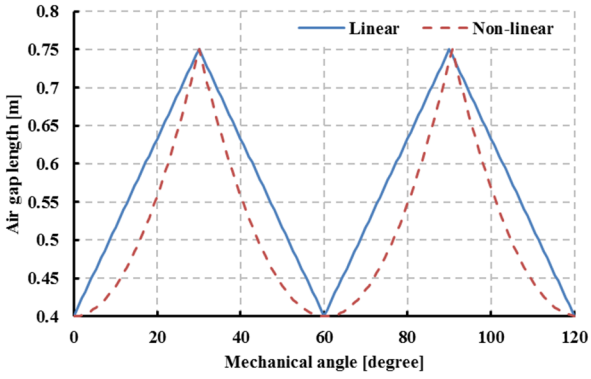

(a)

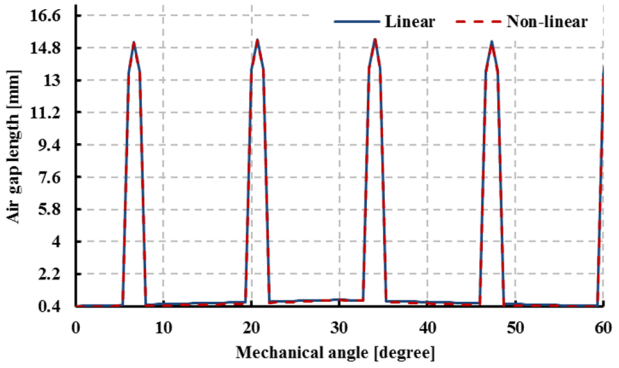

(b)

Fig. 2-14: Air gap length (a): without slot effect, (b): with slot effect.

2.5.3 Back Electro Motive Force Estimation

The no-load back-EMF of the PMSM (e_0) can be calculated based on the no-load air gap magnetic flux (φ_{g0}) and Faraday's law as

$$e_0(t) = -n_{tc}\frac{d\varphi_{g0}}{dt}. \tag{2-24}$$

To calculate φ_{g0}, the winding configuration of the machine should be known. Fig. 2-15 shows the winding configuration for one phase, under one pole of existing 27-slot and 6-pole VFM machine with double layer winding.

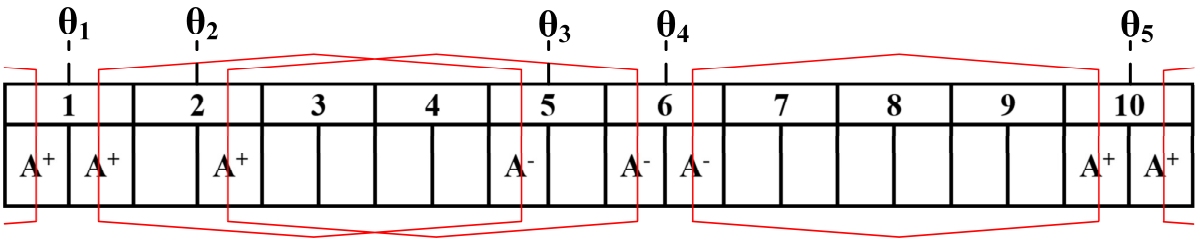

Fig. 2-15: Winding configuration of phase A for one pole for a 27-slot, 6-pole VFM.

The coils are distributed between θ_1 and θ_3, θ_2 and θ_4, and θ_4 and θ_5. Based on this configuration, φ_{g0} for this phase can be calculated as

$$\varphi_{g0}(t) = L_{stk}R_{ro}\left[\int_{\theta_1}^{\theta_3} B_{g0}d\theta + \int_{\theta_2}^{\theta_4} B_{g0}d\theta + \int_{\theta_5}^{\theta_4} B_{g0}d\theta\right]. \quad (2\text{-}25)$$

Phase A also has one coil that starts in θ_1 and goes to the other pole. The effect of this winding is considered in the 3rd term of (2-25) where the first slot of the next pole is counted during the magnetic flux calculation. To calculate φ_{g0} based on (2-25), the B_{g0} should be calculated as a function of angle. To do this, B_{g0} from (2-15), after considering the effects of both stator slots and the uneven air gap, is evaluated using the Fourier transform as a function of θ as

$$B_{g0}(\theta) = \sum_{n=1}^{\infty} a_n \sin(n\theta + \alpha_n). \quad (2\text{-}26)$$

In (2-26), θ is replaced by $(\theta_1\text{-}\omega t)$. Consequently, φ_{g0} (2-25) and e_0 (2-24) can be estimated analytically.

2.5.4 Magnetizing Current

Since the operating principle of VFMs is based on the demagnetization of magnets in the field-weakening mode of operation, the armature winding should also be able to re-magnetize magnets to regain the full torque capability when the motor slows down. In order to fully magnetize the magnets, the magnets operating point has to be pushed beyond the knee of the 1st or 3rd quadrants of the Hysteresis loop. The current at which the magnets saturates is considered the full magnetization current.

Fig. 2-16 shows the equivalent magnetic circuit of the machine during magnetization. In this circuit, I_{mag} is the magnetization current d-axis pulse peak value. $\mathcal{R}_{ri}$, $\mathcal{R}_s$, $\mathcal{R}_g$, and $\mathcal{R}_m$ are the reluctances of the rotor, the stator, the air gap and the magnets, respectively. I_{mag} produces a magnetic flux density of B_m in the magnet.

Based on A_m, the magnetic flux (Φ_m) can be calculated as

$$\Phi_m = B_m A_m. \quad (2\text{-}27)$$

Based on the basic rules of the magnetic circuit

$$\Phi_m(\mathcal{R}_{r1} + \mathcal{R}_{r2} + \mathcal{R}_m + 2\mathcal{R}_g + \mathcal{R}_s) = NI_{mag}. \quad (2\text{-}28)$$

Because of high relative permeability of magnetic steel materials, $\mathcal{R}_{ri}$ and $\mathcal{R}_s$ are negligible.

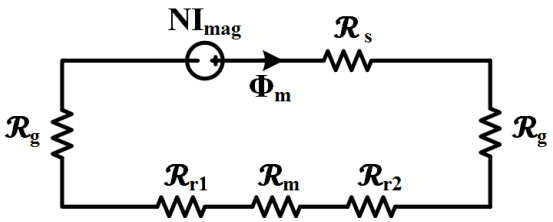

Fig. 2-16: Magnetic equivalent circuit for each pole of VFM during the magnetization.

Also, the number of current carrying turns is $N=aN_{spp}n_{tc}$. Based on (2-27), (2-28) can be written as

$$B_m A_m(\mathcal{R}_m + 2\mathcal{R}_g) = aN_{spp}n_{tc}I_{mag} \tag{2-29}$$

where $\mathcal{R}_m = \frac{t_m}{\mu_{rec}\mu_0 A_m}$ and $\mathcal{R}_g = \frac{g}{\mu_0 A_g}$ and as a result (2-29) is:

$$B_m A_m(\frac{t_m}{\mu_{rec}\mu_0 A_m} + \frac{2g}{\mu_0 A_g}) = aN_{spp}n_{tc}I_{mag} \tag{2-30}$$

and after some simplifications

$$\frac{B_m}{\mu_0}(\frac{t_m}{\mu_{rec}} + \frac{2gA_m}{A_g}) = aN_{spp}n_{tc}I_{mag}. \tag{2-31}$$

Based on (2-13) and (2-14), $\frac{A_m}{A_g} = \frac{h_m}{\tau_p - t_m}$, and as a result I_{mag} can be calculated as

$$I_{mag} = \frac{B_m}{\mu_0 a N_{spp} n_{tc}}\left(\frac{t_m}{\mu_{rec}} + \frac{2gh_m}{\tau_p - t_m}\right). \tag{2-32}$$

Based on (2-32), the magnetization current of the machine can be estimated analytically and the effect of different design parameters such as magnet dimensions and the air gap length on the magnetization current can be evaluated. When the AlNiCo9 is fully magnetized, B_m is 1.5 T. Based on this value and the machine geometry, the estimated magnetization current is 35 A. This is close to the experimental magnetization current of 40 A. The air gap length of the proposed machine changes from 0.4 mm to 0.75 mm and in the magnetization current estimation, the average air gap length is used.

2.5.5 Calculation of Peak to Peak Value of the Torque

The instantaneous electromagnetic torque (T_{el}) can be expressed as the derivative of the co-energy (W') with respect to the rotor-stator position in the air gap as

$$T_{el}(\theta) = \frac{\partial W'}{\partial \theta} | i: constant. \tag{2-33}$$

Also based on the torque definition and Lorentz force, the electromagnet torque can be calculated as

$$T_{el} = \iiint \vec{r} \times (\vec{J} \times \vec{B}) dv. \tag{2-34}$$

where v, $\vec{r}$, $\vec{J}$ are the volume of integration, the vector diagram of the integration volume and the current density vector respectively. (2-34) can be written as the interaction between the magnet flux density and stator current. In other words, the peak to peak value of the electromagnetic torque can be calculated as the summation of the torques produced by the current-field interaction at each slot as [53]

$$\Delta T_{el}(\theta) = L_{stk} R_{ro} \sum_{n=1}^{N_s} \int_0^{b_0} B_{g0}(\omega_1).J(\omega_1) d\omega_1 \tag{2-35}$$

where *J* can be defined as [49]:

$$J(\theta) = \begin{cases} \frac{i_a}{b_0} & \theta \text{ is in a slot and current has the positive direction.} \\ -\frac{i_a}{b_0} & \theta \text{ is in a slot and current has the negative direction.} \\ 0 & \text{out side the slot opening.} \end{cases} \tag{2-36}$$

It should be considered that *J* is similar for all phases.

2.6 Results and Discussion

The results of the analytical model are compared with the FE results in this section.

2.6.1 Air Gap No-load Magnetic Flux Density

As it is mentioned before, the air gap flux density at the no-load condition is the key parameter of the analytical model. Fig. 2-17 depicts the magnetic flux density in the middle of the air gap at the no-load condition, for both analytical and FE models. Fig. 2-17(a) shows the air gap magnetic flux density for the VFM with even air gap length of $g=0.4\ mm$. Fig. 2-17(b), represents the air gap magnetic flux density for the VFM with uneven air gap length, $g_{min}=0.4\ mm$, and $g_{max}=0.75\ mm$. In Fig. 2-17(b), linear and non-linear refer to the linear function of the air gap length and the non-linear function of air gap length, respectively.

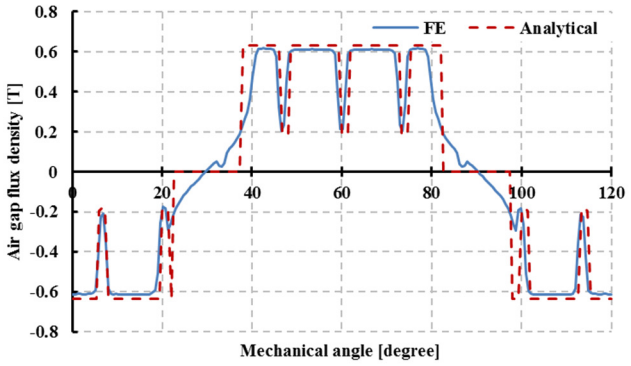

(a)

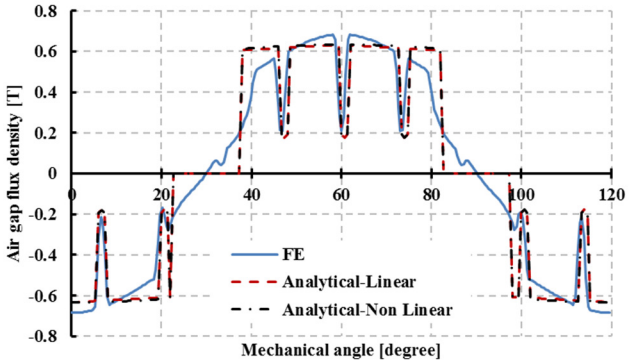

(b)

Fig. 2-17: Air gap magnetic flux density for VFM with (a): the even air gap, (b): the uneven air gap.

Both figures show good agreement between the analytical and FE results. The effect of stator slots can be seen in this figure. The comparison of Fig. 2-17(a) and (b) shows the effect of uneven air gap length on the air gap magnetic flux density waveform. Based on Fig. 2-17(b), the air gap magnetic flux density for both linear and non-linear functions is almost the same because of the dominant effect of the stator slots on the actual air gap length. One of the benefits of this analytical model is the ability to investigate effects of design parameters on the machine characteristics before performing FE analysis.

To estimate the average magnet torque, the maximum value of the main component of the no-load air gap flux density (see (2-17)) should be considered. Based on the results of Fig. 2-17(b), the analytical model show good agreement with the FE model in terms of the main component maximum value. Based on (2-15) and (2-16), the effect of the magnet dimensions and the ML of the magnet can be studied with the analytical model before performing the FE simulation.

Fig. 2-18 demonstrates the effect of the magnet length and the ML of the magnet on the no-load air gap magnetic flux density for an even air gap length.

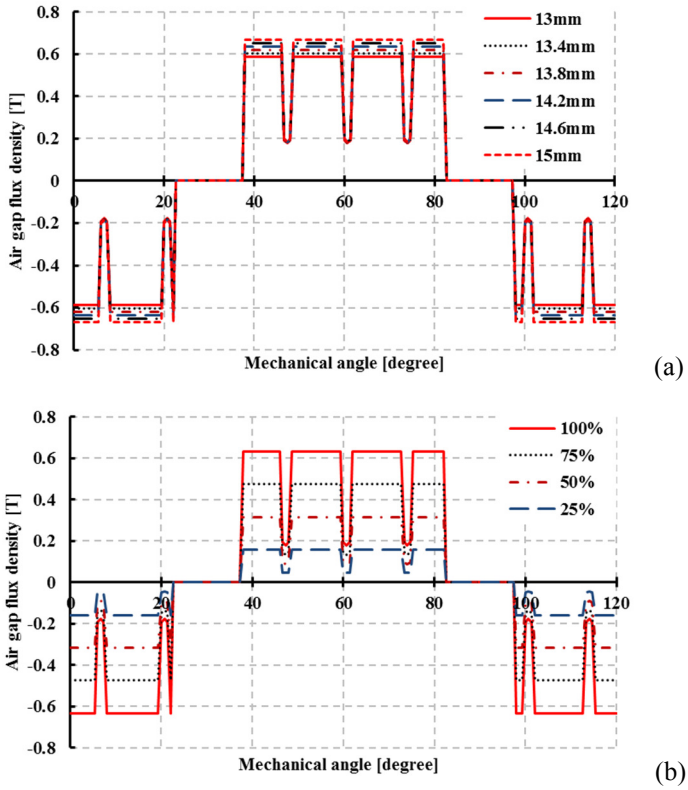

Fig. 2-18: Effect of (a): the magnet length, (b): the ML of the magnet on the air gap magnetic flux density for the VFM with an even air gap (analytical model).

In Fig. 2-18(a), the effect of the magnet length on the air gap flux is clear (see (2-15)) and 15.4% increase in magnet length increases the air gap magnetic flux density by about 14.3%. Based on Fig. 2-18(b), the peak value of the air gap magnetic flux density is a linear function of the ML of the magnet (see (2-15)).

2.6.2 No-load Back-EMF

Fig. 2-19 compares the measured, the FE simulated and the analytically estimated no-load back-EMF when the magnets are fully magnetized. The results of the two models have a good agreement with the experimental results. Based on these results, the fundamental component of the no-load back-EMF, for the experimental, the FE simulation and the analytical results are 195.3 V, 208.6 V and 205.7 V.

The measured back-EMF waveform correlates well with the FE and the analytical predictions with a 6% reduction in the measured RMS voltage. This deviation can be caused by the stresses introduced into the steel due to the lamination cutting.

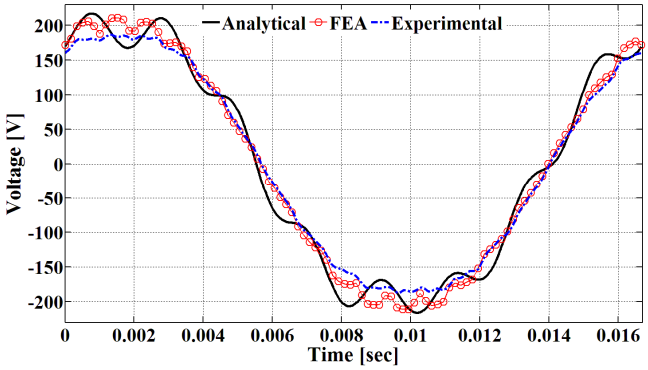

Fig. 2-19: No-load back-EMF for the VFM.

These stresses can affect the lamination properties and they were not considered in the FE simulations. In addition, the reduction of the measured flux linkage can also be attributed to the actual magnet properties, which may differ from the simulated properties in the FE simulation. It should be noted that in the analytical calculation of the no-load back-EMF, only nine harmonics of the air gap magnetic flux density are considered to keep the method fast, simple and at the same time accurate.

2.6.3 Torque vs. Torque Angle Curve and Peak to Peak Value of Torque

The analytical method has the ability to calculate the magnet torque component of the machine. To compare the analytical and FE models results, the reactance torque ($T_{\mathcal{R}}$) of the machine should be deducted from the FE results. To calculate $T_{\mathcal{R}}$ based on FEA, the magnet is replaced with air and the machine reluctance torque is calculated.

Fig. 2-20 compares the mean value of the magnet torque from FE and analytical models for different torque angles. Analytical results show good agreement with FE results. This comparison shows that the analytical model is a reliable tool to do the initial design of the VFM.

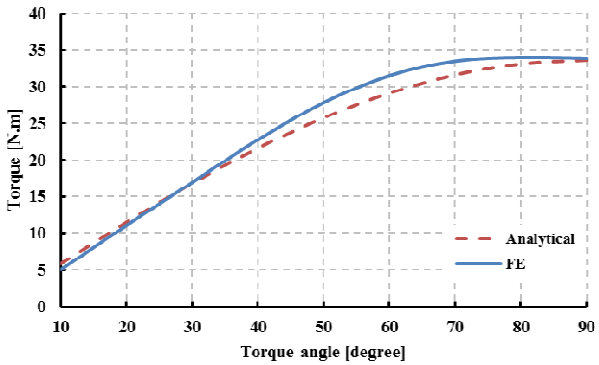

Fig. 2-20: Average magnet torque vs. torque angle.

Fig. 2-21 shows the peak to peak value of the electromagnetic torque for the VFM vs. angle from both analytical and FE models.

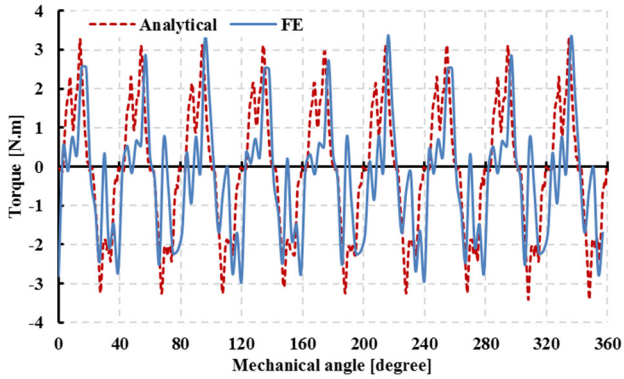

Fig. 2-21: Peak to peak electromagnetic torque for the VFM.

Based on this figure, the torque waveforms of both methods are in good agreement based on their peak to peak values. Fig. 2-22 compares the average magnet torque and peak to peak value of torque vs. the magnet length and the magnet width for both analytical and FE models.

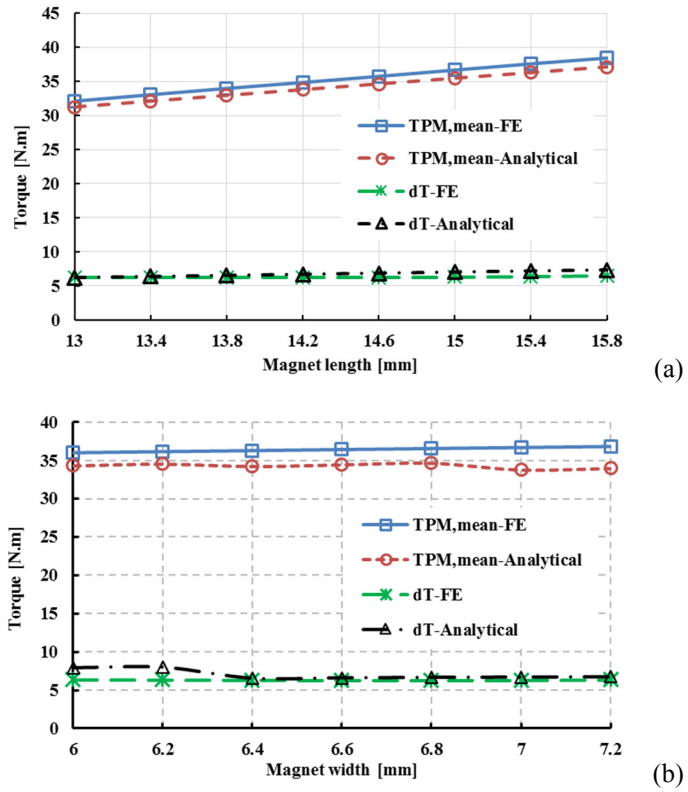

Fig. 2-22: Average magnet torque and torque peak to peak value of the VFM vs. (a): magnet length, (b): magnet width, for both analytical and FE models.

Based on Fig. 2-22(a), the torque mean value is a linear function of magnet length and 21.5% increase in the magnet length will increase the average torque by 18.8%. The reason for this increase can be seen in Fig. 2-18(a) and associated with (2-15). The increase in h_m increases B_{g0} and consequently, enhances $T_{PM,\text{mean}}$. The figure presents good agreement between the FE and the analytical results. The error between these two models, for different magnet lengths, is in the range of 2% to 10%. The same agreement can be seen in Fig. 2-22(b), as the error for torque peak to peak value is in the range of 1% to 5%.

2.7 Conclusion

In this chapter, an analytical model of a spoke type VFM at no-load condition has been discussed. To make this model easy to understand, the basic principles of the VFM such as magnet flux control, the magnet topology selection and the general dimensions of the existing VFM are discussed. While the no-load air gap flux density is used to estimate the torque waveform and the back-EMF of the machine, the effects of stator slots and uneven air gap length were taken into account in the analytical model. Moreover, a new analytical estimation method for the magnetization current of VFM was proposed. Besides, the average magnet torque vs. torque angle and torque peak to peak value are analyzed using the analytical model. Using this analytical model, the effect of different design parameters such as the magnet dimension and ML on the machine performance can be analyzed. The analytical model had been verified by the FE simulation results for all cases. This analytical model can provide an analytical design criterion for VFM based on the magnet torque and magnetization current that is presented in the next chapter.

Chapter 3. Design Optimization of Variable Flux Machines

3.1 Introduction

The recent progress in optimization algorithms and FE software opens a new approach in the design optimization of electrical machines with a complex topology. Design optimization requires analysis of a large number of candidate designs. Therefore, it must be done using a well-defined strategy.

Different types of optimization strategies with different optimization objectives are used for PMSMs as shown in Table 3-1.

Table 3-1. Optimization methods for PMSMs.

Ref.	Machine	Optimization Method	Objectives
[56]	BLDC	Analytical model and FE software	Cogging torque
[57]	IPM	A parallel sensitivity analysis using a second-order response surface methodology followed by a large-scale design optimization based on evolutionary algorithms and FE software	Minimize active material cost, power loss and torque ripple
[58]	Outer rotor PMSM	Improved Tabu search algorithm and FE software	Maximize average torque and efficiency, minimize torque ripple
[59]	SMC claw-pole PMSM	Sizing equation, local sensitivity analysis, global sensitivity analysis, 3D FE software	Minimize the material cost, maximize the output torque, keep the volume constant
[60]	IPM and CWSPMSM	MATLAB scripts includes design equations, magnetic FEA, multi-objective optimization, and simplified structural and thermal design	Maximize efficiency and torque
[61]	SPMSM	Multi-objective optimization method and FE software	Minimize weight and winding temperature, maximize efficiency

In most cases, the design optimization of a PMSM is a multi-dimensional multi-objective problem due to the large number of design parameters, objectives, and constraints. Smart algorithms are used widely to do the design optimization in various types of PMSM [56]-[61].

The design and control of the existing tangentially magnetized VFM is presented in [41]-[43]. While the tangentially magnetized design can achieve high torque at low speeds and high efficiency at higher speeds, the tangentially magnetized rotor design has relatively high torque

ripple ($T_r\%$) compared to surface and conventional interior PMSMs. For the existing VFM, the experimental and FE-based characterizations confirm the high $T_r\%$ and I_{mag}. These can limit the application of the tangentially magnetized VFM in traction drives of electric vehicles. Therefore, an optimization method is developed in this chapter to reduce on $T_r\%$ and I_{mag} of this machine, while the torque mean value is kept within an acceptable range.

In the mentioned works in Table 3-1, all of the objectives can be defined in one FE simulation file. However, for the VFM, torque ripple and magnetization current are defined in two different operating conditions. In this chapter, a complex multi-objective optimization problem is transferred to a two-level optimization procedure to reduce $T_r\%$, and I_{mag}, and to keep the torque mean value (T_{mean}) within an acceptable range (maximum 5% of reduction in comparison with the existing VFM). Moreover, the no-load operating point of the magnet must be considered during the optimization procedure.

The proposed optimization method in this chapter consists of two levels. The first level is selecting the magnet dimensions based on the required values of the magnetization current and the average torque. To do this, an analytical design criterion is proposed. The second level uses the FE software and a Genetic Algorithm (GA) to perform the optimization. Due to the complex relationship between the objectives, firstly, GA is used to reduce $T_r\%$ and keep T_{mean} in the acceptable range. Then I_{mag} and the no-load operating point of the magnet are checked and the final design refinements are applied.

This chapter is organized as follows. In section 3.2, the characterization procedure of the existing VFM is explained. Section 3.3 presents an analytical design criterion for the VFM, which is used to select the magnet dimensions based on the desired values of T_{mean} and I_{mag}. Section 3.4 states the problem and discusses the design optimization limitations. Section 3.5 focuses on the design optimization of the VFM using GA and FE software. In this section, the data structure of the optimization procedure, the main steps and principals are proposed. Moreover, the complete flowchart of the optimization procedure, and also a comparison between the initial design and the optimized one are presented in this section. Section 3.6 concludes this chapter.

3.2 Existing Variable Flux machine Torque and Magnetization Current Characterization

To develop an effective optimization strategy, it is essential to have a general overview of the existing VFM and measure its characteristics accurately. As this machine has the ability to be magnetized and demagnetized, the properties of this procedure and the features of the machine at different MLs should be investigated.

3.2.1 Existing Variable Flux Machine Design Specifications

The design specifications of the existing machine are shown in Table 3-2.

Table 3-2. Specifications of the existing VFM.

Number of poles	6	Magnet material	AlNiCo 9
Number of slots	27	Steel material	M19G29
Stator outer diameter (mm)	200	Saliency ratio (L_d/L_q)	1.6
Axial length (mm)	120	DC bus voltage (V)	600
Magnet width (mm)	7	Rated current (A)	14.14 (peak)
Magnet length (mm)	14.2	Output torque (N.m)	36.8
Active total mass (kg)	23.9	Torque density (N.m/litter)	9.76
Rated speed (rpm)	1150	Air gap length (mm)	0.4-0.75

The air gap length of the VFM is uneven. It is minimized at the *d*-axis (0.4 mm) and maximized at the *q*-axis (0.75 mm) to reduce the back-EMF harmonics and make the air gap flux density more sinusoidal. Moreover, the reduction in the machine core losses and the improvement of the machine performance is reported in [41], [42]. The maximum output torque of the proposed VFM in Table 3-2 is 36.8 N.m that is achieved with the rated peak current of 14.14 A [10 A RMS], and the DC bus voltage of 600 V. Both rotor and stator core are manufactured with M19 G29 as a steel material. For this machine, the base speed is evaluated as 1150 rpm.

3.2.2 Magnetization and Demagnetization Procedure Characterization

In order to apply VFMs in the industrial, and traction applications, the magnetization and demagnetization procedures, as well as the machine features at different MLs, should be studied

in more depth. Moreover, in a specific working strategy, this machine may be subjected to many times of magnetization and demagnetization based on the operating condition (required torque and speed). In this situation, the properties of the magnetization and demagnetization current pulses besides the amount of energy is important, specifically for the electrified transportation applications, where the machine is supplied using a battery and the driving range is important.

3.2.2.1 Why Demagnetization and Magnetization?

The VFM with AlNiCo has great potential as a traction motor in electrified transportation. The application of low coercivity magnets, as well as the spoke type design of this machine, provide the ability of magnetization and demagnetization of the rotor magnets using short-time *d*-axis current pulses that improves the efficiency of the machine in the high-speed region. This short-time *d*-axis current produces negligible loss.

For the conventional rare-earth PMSM, in the field-weakening mode of operation, a permanent demagnetizing current is needed to reduce the magnet flux and keep the back-EMF within the system limitations. This produces Ohmic losses in the machine in addition to the high current from the inverter. In addition, for conventional rare-earth PMSMs, the rotor magnets remains in the fully magnetized state at all operating conditions. At higher speeds, the eddy current loss in the steel laminations increases, as it is proportional to the square of the flux rate of change. This causes a significant increase in the lamination core losses and reduces the machine efficiency at higher speeds. For the VFM with reduced ML, the core losses will be reduced in the higher speed regions. As a result, the VFM can work with high efficiency for a wider range of speed while the conventional rare-earth PMSM suffers from lower efficiency at high-speed region.

3.2.2.2 Magnetization Level Estimation

To calculate the ML of the VFM experimentally, the no-load flux linkage should be estimated. The back-EMF of the VFM while running as a no-load generator is used to estimate the linkage flux in the partial magnetization condition (λ_{fp}) as

$$\lambda_{fp} = \frac{\sqrt{2}V_{n,LL}}{2\sqrt{3}\pi p\frac{N}{60}} \tag{3-1}$$

where $V_{n,LL}$ and N are the RMS value of the line to line no-load back-EMF and rotor speed in

rpm respectively. The ML of the VFM is defined as

$$ML\% = \frac{\lambda_{fp}}{\lambda_{ff}} \times 100 \tag{3-2}$$

where λ_{ff} is the flux linkage of the fully magnetized VFM while it is run as a no-load generator. A DC motor is used to run the VFM as a no-load generator. Table 3-3 shows the value of measured line to line voltage, the speed of the VFM, and the estimated flux linkage.

Table 3-3. Measured speed, line to line voltage, and the resultant flux linkage for VFM.

Speed [rpm]	Line to line voltage [V]	Flux linkage [Wb]
476	94.5	0.52
749.9	148.68	0.52
1138.4	225.63	0.52

Based on the test and FE results, the flux linkage of the fully magnetized VFM is 0.52 Wb and 0.55 Wb, respectively, which shows around 5.8% deviation. The reduction of the measured flux linkage can be attributed to the magnet properties, which may differ from the simulated properties in the FE model.

To do ML estimation in the FE software, the operating point of the magnet should be considered for different operating conditions. Fig. 3-1 shows the typical B-H curve of AlNiCo 9 magnet.

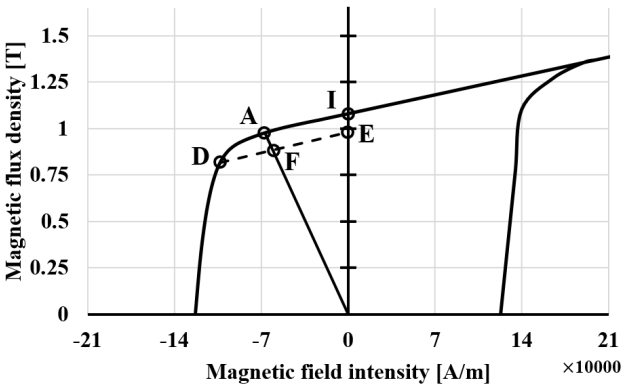

Fig. 3-1: B-H loop of AlNiCo 9 for 1st and 2nd quadrants.

To estimate the *ML(%)* of the magnet, the B-H loop of AlNiCo 9 (Fig. 3-1) in the 1st and 2nd quadrants is used. As can be seen from the magnetic properties of AlNiCo in Fig. 3-1, once the

magnet operating point goes from point A to point D as a result of an external magnetic field, the magnet does not recoil to point A and recoils to point F through line DE that has the same slope as line AI. This means that the magnet is partially demagnetized. To estimate *ML(%)* of the magnet at the operating point F, the magnetic flux density of point E (B_E) can be calculated as

$$\frac{(B_A - B_I)}{H_A} = \frac{(B_D - B_E)}{H_D} \Rightarrow$$
$$B_E = B_D - \frac{H_D (B_A - B_I)}{H_A} \tag{3-3}$$

where B_A, B_I and B_D are the magnetic flux densities at points A, I and D respectively (Fig. 3-1). H_A and H_D are the magnetic field intensities at points A and D. The *ML(%)* can be defined as

$$ML(\%) = \frac{B_E}{B_I} \times 100. \tag{3-4}$$

To estimate the magnet operating point while the demagnetization or magnetization current pulse is applied to the VFM, 8 probes are placed along the magnet in the FE model, to record *B* and *H* during the magnetization/demagnetization procedure (Fig. 3-2).

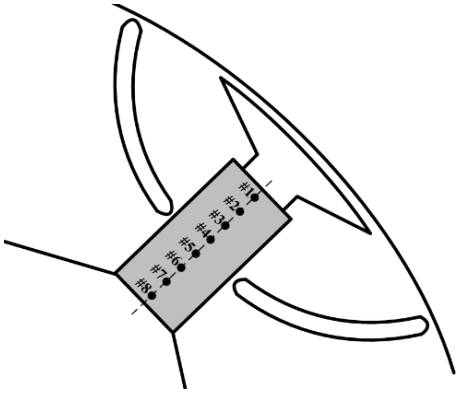

Fig. 3-2: Probes to record *B* and *H* in the FE model.

Based on the recorded data and using (3-3) and (3-4), the *ML(%)* for each point and the average *ML(%)* could be calculated. The mean value of both magnetic flux and field intensity for each probe is calculated over an excitation cycle. These mean values are averaged for 8 probes to have the average magnetic flux density and field intensity in the magnet which is considered as the operating point of the magnet in each working condition.

To clarify this concept, an operating regime is developed for the VFM to check the flux

density of the magnet before, during, and after the demagnetization procedure. Fig. 3-3 shows the magnetic flux density of the magnet recorded by the probes while the VFM works at no-load condition for one cycle and then it is supplied by the demagnetization current of -4 A for one cycle and at the end, it works in no-load condition again for one cycle.

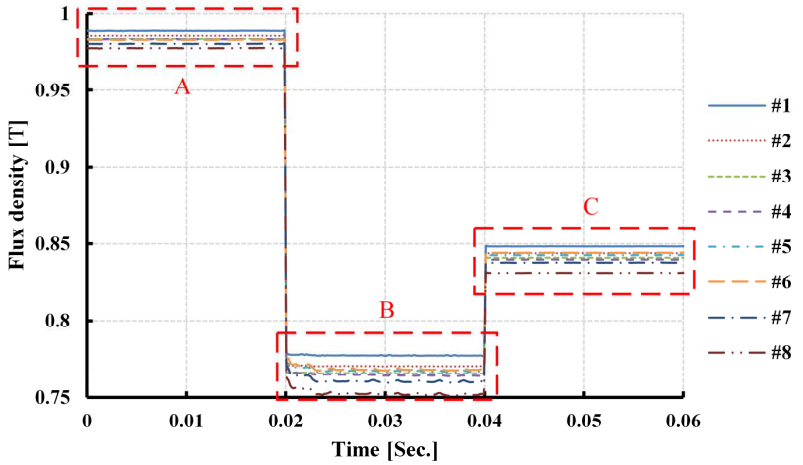

Fig. 3-3: The magnetic flux density of the magnet before (A), during (B), after (C) the application of the demagnetizing current of -4 A (FE results).

In Fig. 3-3, section (A) is the no-load condition before the demagnetization, section (B) shows the magnet flux density during the demagnetization, and section (C) is the no-load condition after removing the demagnetizing current. According to this figure, the magnetic flux density of the magnet is reduced during the demagnetization procedure. After removing the demagnetizing current, the magnetic flux density of magnet increases, but it is still less than the same parameter before the demagnetizing current that shows the demagnetization of the magnet. Table 3-4 shows the mean value of the magnet flux density before, during, and after the -4 A demagnetizing current pulse.

Table 3-4. The mean value of flux density for each probe and the average magnet flux density, before, during, and after the demagnetization procedure (FE results).

Probe No.	Before	During	After
1	0.99 T	0.78 T	0.85 T
2	0.99 T	0.77 T	0.84 T
3	0.98 T	0.77 T	0.84 T
4	0.98 T	0.76 T	0.84 T
5	0.98 T	0.77 T	0.84 T
6	0.98 T	0.77 T	0.84 T
7	0.98 T	0.76 T	0.84 T
8	0.98 T	0.75 T	0.83 T
Average	0.98 T	0.77 T	0.84 T

According to Table 3-4, the average magnetic flux density of the magnet in the no-load condition is 0.98 T, and it shifts to 0.77 T during the demagnetization procedure. After the demagnetization procedure the new operating point of the magnet is 0.84 T. According to these results, the -4 A demagnetizing current demagnetizes the fully magnetized VFM to a ML% of 75%. Moreover, the flux linkage of the machine can be extracted in the FE model that can be used for ML estimation of the VFM. The ratio of the maximum linkage flux of sections (C) and (A) in Table 3-4 gives the ML of the VFM.

3.2.2.3 Magnetization Current

To measure the magnetization current, the fully demagnetized VFM is supplied with a *d*-axis current pulse with controlled amplitude. After each pulse, the machine is run as a no-load generator and based on the RMS value of the no-load back-EMF and the speed, the ML of the machine is measured. According to the experimental results, for the existing VFM, I_{mag}=40 A, that is 2.8 times of the rated current (14.14 A). The FE model of machine also shows that with 40 A *d*-axis magnetization current, the AlNiCo magnets of the existing VFM are fully magnetized. The high required I_{mag} also reveals the necessity for a higher rating inverter and drive system that is undesirable for electrified transportation applications.

3.2.3 Torque Waveform and Torque-Angle Characterization

Torque is one of the important parameters for the machine characterization. The torque-efficiency characteristics [62], the toque-current characteristic [63], and the torque-angle characteristics [64] are measured for the PMSMs. The power versus rotor position is measured for a 27-slot and 6-pole PMSMs in [65]. A static measurement method of the torque waveform and torque angle characteristics of the PMSMs using the potential of the drive system can be interesting to characterize this machines. In this section, the conventional SPWM drive system is used to characterize the VFM machine. This means that the same drive system and equipment that are used to run the VFM are also used to characterize the machine. Hence there is no additional equipment for the machine characterization.

3.2.3.1 Experimental Setup

The FE model of the VFM plays the main role in the optimization procedure. As a result, to verify the FE model, the torque waveform of the VFM are measured experimentally and

compared to the FE results. A drive system based on a power electronic converter with an advanced space vector pulse width modulation (SVPWM) technique is used to control the proposed VFM [43]. The main idea for the static torque waveform measurement is using a constant current vector to supply the locked VFM at the specific rotor position. Fig. 3-4 shows the lock system, the torque transducer, the VFM and the DC dyno.

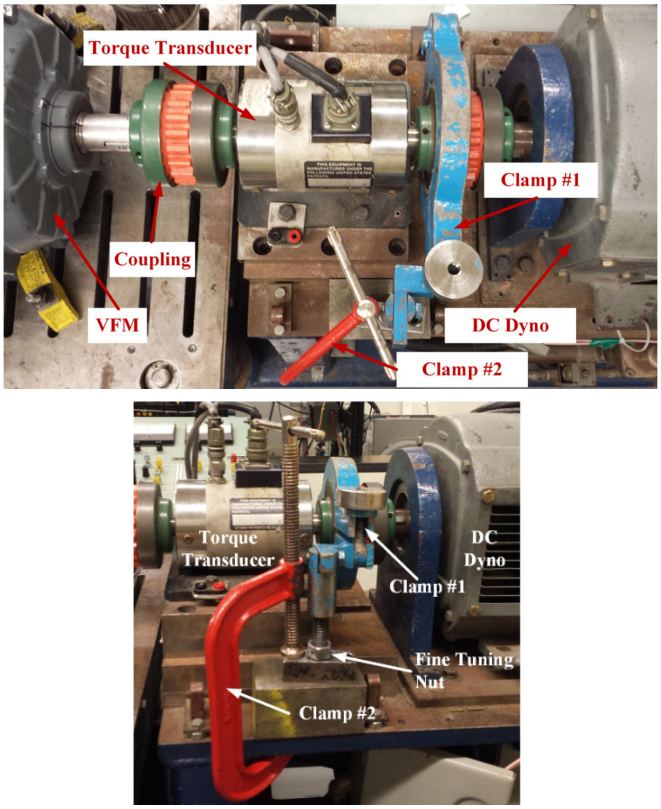

Fig. 3-4: Experimental setup and the mechanical lock system.

In this lock system, the rotor is locked using clamp #1 and clamp #2. With this lock system and based on the encoder resolution, the accuracy of the measurement is around 0.5° electrical ((1/6)° mechanical). This accuracy shows the high potential of this method for precise static measurement of torque waveforms. To measure the torque-angle curves using the SVPWM drive system, the rotor is locked in a fixed position and the torque angle changes are applied by changing the current vector. Based on the load of the machine and the torque angle, I_d and I_q are specified.

To reduce the effect of the switching and the drive system on the torque waveform, both *d*- and *q*- axes currents are monitored to ensure a minimum ripple. During this test, the ripple of

I_d and I_q are maintained less than 1% using the PI controllers of the drive system.

3.2.3.2 Results

Fig. 3-5 compares the measured torque waveforms of the VFM with the FE results for two different operating conditions (maximum power and I_d=0) at a ML of 96%.

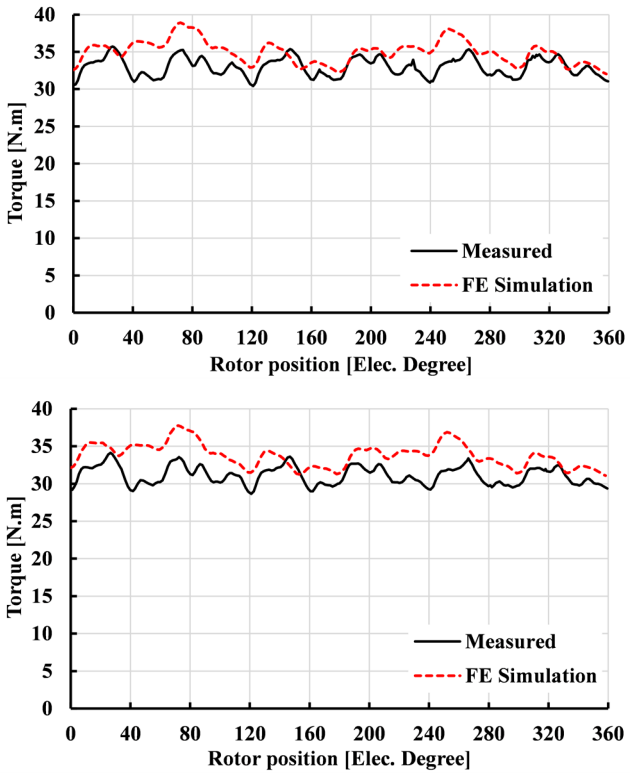

Fig. 3-5: Torque waveforms of the VFM (comparison between measured and FEA results) at rated current and ML of the magnet equal to 96% (a) maximum power point (θ=78°), (b) I_d=0 (θ=90°).

For maximum power, the torque mean values from the FE simulation and the measured results are 34.9 N.m and 33 N.m, respectively that shows 5.5% deviation. For I_q=14.14 A and I_d=0 operating condition, the torque mean values from the FE simulation and the measured results are 33.7 N.m, and 31.1 N.m, respectively that shows 7.6% deviations. According to the results, the FE and measured torque ripple values for the 1st operating condition (θ=78°) are 17.6% and 19.9%, respectively. These values for the 2nd operating condition (θ=90°) are 16% and 19.7% respectively. Besides the difference in the flux linkage values, the accuracy of the measurement equipment, especially the torque transducer can cause a deviation between the measured values and the FE simulation results. The torque transducer was calibrated before doing the torque measurement tests, but the calibration can be affected by the torque ripple of

the machine.

3.3 A Novel Analytical Design Criterion for the Variable Flux Machine

The magnet dimensions in rare-earth PMSMs are selected based on the desired torque and the no-load operating point of the magnet using the *PC*. However, for the VFM, I_{mag} is an important parameter that must be considered during the design procedure. The magnet dimensions of the VFM should be selected based on the desired T_{mean} and I_{mag}. For the VFM, an equivalent magnetic circuit without considering the stator slots effect is used to develop the mathematical model of the machine for the no-load condition. In this model, the iron reluctance is assumed to be negligible.

The no-load air gap flux density, B_{g0}, is a function of the air gap size, magnet dimensions, and properties as explained in (2-15). Based on the definition of A_g and A_m, B_{g0} can be rewritten as

$$B_{g0} = \frac{2B_r h_m}{(\tau_p - t_m + \frac{4g\mu_{rec}h_m}{t_m})}. \tag{3-5}$$

Using the analytical model, I_{mag} can be estimated using (2-32). Based on (3-5), h_m that is necessary to produce the required B_{g0} is

$$h_m = \frac{B_{g0}(\tau_p - t_m)t_m}{(2B_r t_m - 4g\mu_{rec}B_{g0})}. \tag{3-6}$$

Substituting h_m as a function of B_{g0} and t_m in (2-32), I_{mag} is

$$I_{mag} = \frac{B_m}{\mu_0 N_{spp} a n_{tc}}(\frac{t_m}{\mu_{rec}} + \frac{gB_{g0}t_m}{B_r t_m - 2g\mu_{rec}B_{g0}}). \tag{3-7}$$

Rearranging (3-7), t_m can be calculated by solving the following equation

$$k_1 k_2 k_4 t_m^2 + t_m(-k_1 k_2 k_5 + k_1 k_3 B_{go} - k_4 I_{mag}) + k_5 I_{mag} = 0 \tag{3-8}$$

where $k_1 = \frac{B_m}{\mu_0 N_{spp} a n_{tc}}$, $k_2 = \frac{1}{\mu_{rec}}$, $k_3 = g$, $k_4 = B_r$, and $k_5 = 2g\mu_r B_{g0}$. Using (3-8), t_m is calculated based on the required values of B_{g0} and I_{mag}. Considering the estimated t_m and using (3-6) or (3-7), h_m can be calculated.

Fig. 3-6 shows the magnet dimensions for three different desired values of $T_{PM,\text{mean}}$ and I_{mag}.

With constant I_{mag}, to increase $T_{PM,\text{mean}}$ the magnet length should be increased. Moreover, with the constant $T_{PM,\text{mean}}$, to reduce I_{mag} the magnet thickness should be reduced. According to Fig. 3-6, with constant I_{mag}, an 8% increase in h_m increases $T_{PM,\text{mean}}$ by 7%. Moreover, with the constant $T_{PM,\text{mean}}$, an 84% increase in t_m increases I_{mag} by 75%.

It is clear that I_{mag} and $T_{PM,\text{mean}}$ are not completely decoupled and are functions of both h_m and t_m.

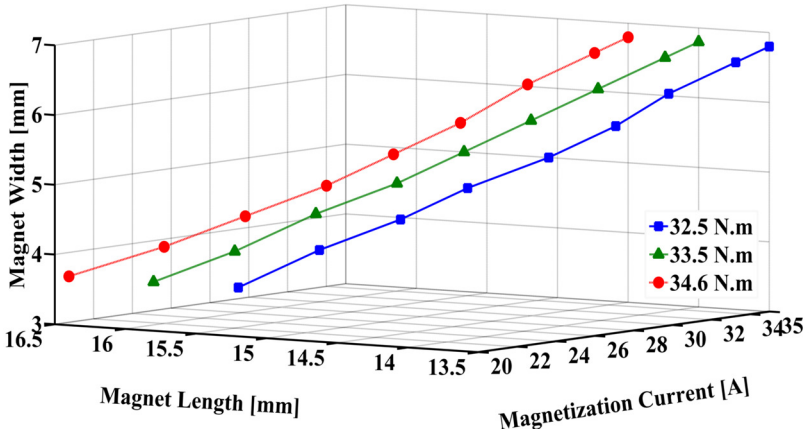

Fig. 3-6: Magnet dimensions as a function of I_{mag} and $T_{PM,\text{mean}}$ (analytical design criterion).

To verify the analytical design criterion, three different VFMs with zero saliency are modeled using the FE software with constant t_m and h_m of 13.6 mm, 14.1 mm and 14.6 mm.

Fig. 3-7 compares the analytical and FE results for the $T_{PM,\text{mean}}$. Based on this figure, both analytical and FE results show acceptable agreements that validate the capability of the analytical design criterion to be used for the design of the VFM. To reduce the magnetization current, the magnet thickness should be reduced. At the same time, the no-load operating point of the magnets in the VFM should be checked.

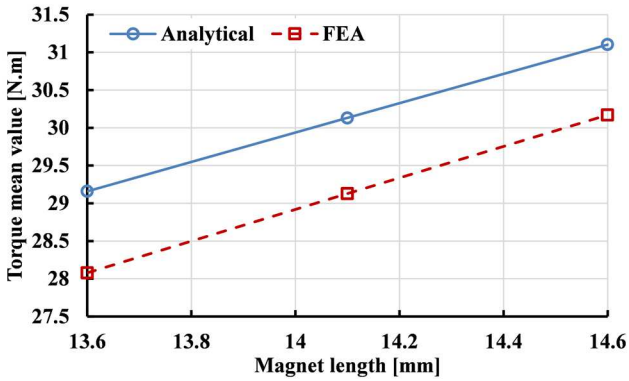

Fig. 3-7: Analytical design criterion verification with FE results.

3.3.1 Magnet Dimensions for the Variable Flux Machine

According to the results provided in section 3.2.2.3, the magnetization current of the machine is larger than the rated current of the machine that implies a higher current rating of the drive system. This optimization procedure aims to optimize the size of the magnet based on the desired value of the magnetization current and torque mean value. Reduced magnetization current, decreases the rating of the drive system which can be economically beneficial in electrified transportation applications. The magnet thickness affects the *PC* and its reduction shifts the AlNiCo magnet no-load operating point towards the knee point of the B-H loop. In other words, the magnetization current reduction can cause partial demagnetization of the rotor magnets even at no-load condition. Fig. 3-8 shows the relationship between the magnetization current and operating point of AlNiCo magnets.

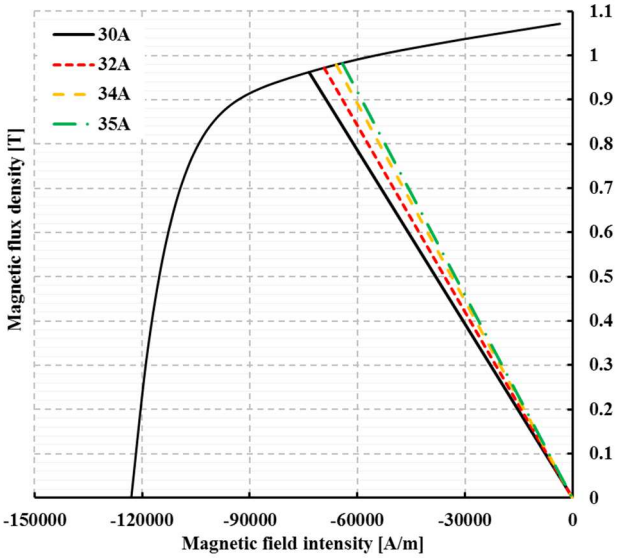

Fig. 3-8: Connection between air gap lines and the magnetization current (FE simulation).

Based on the proposed analytical design criterion and to achieve I_{mag} close to 35 A and T_{mean} close to 36 N.m, the initial magnet length and width for the design optimization procedure are assumed 5.8 mm and 15.4 mm, respectively. The modified magnet dimensions in comparison with the magnet dimensions of the existing VFM (7 mm×14.2 mm) show more than 10% reduction in magnet volume.

3.4 Design Optimization, Problem Statement and Limitations

In order to reduce the prototyping cost, the same stator of the existing VFM is used during

the optimization procedure. However, the similar stator design means a constant number of poles and stator slots, as well as a fixed winding design. As the stator is 27-slot and double layer, the rotor pole number is limited to 6 that is a significant limitation in the design of the new machine. Also, the fixed stator design limits the outer design of the rotor and also the rotor magnetic material. Besides, the voltage and current ratings of machine are kept constant.

3.5 Design Optimization Using Genetic Algorithm and Finite Element Software

The optimization procedure using the GA of the FE software is presented in this section. The main features of the GA and the data structure of the optimization procedure are described.

3.5.1 Data Structure of the FE-Based Optimization Procedure

Fig. 3-9 shows the data structure of the proposed optimization procedure in the FE software [66]. All FE projects have the basic geometry information.

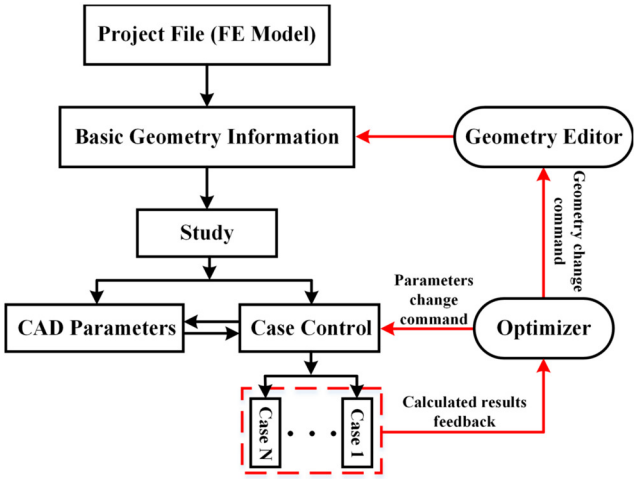

Fig. 3-9: The data structure of the FE based optimization procedure [66].

The CAD model of the machine is parameterized in the geometry editor. Some of these CAD parameters may be selected as optimization parameters to be used during the optimization procedure. In the case control, the optimizer setting is defined, the optimization parameters and their range are selected and the optimization objectives are specified. Based on the number of optimization parameters and their range, some initial cases are defined. An optimization controller uses the optimization engine to generate new cases based on the result of each initial case. As a result, the next set of optimization parameters are calculated and a command is sent to the geometry editor to change the optimization parameters and create the new cases. This

procedure is terminated automatically once the algorithm converges at the desired objectives.

3.5.2 Genetic Algorithm

GA as an evolutionary algorithm works based on the example of the biological evolution and try to breed the optimal solution instead of calculating it. In this algorithm, a group of new generations is generated after crossover, mutation and selection and individuals (genes) with high adaptability remain due to the selection [66].

The Real Number Genetic Algorithms is used in the FE software. In the FE software, the population size, the maximum number of generations, the number of children, step-size parameter and stopping criteria can be defined. Based on the software support recommendations, the appropriate population size and maximum number of generations are equal to the number of optimization parameters×10. The number of children is the number of optimization parameters×4+1. The step-size parameter determines the scale of displacement in the global descent direction of the range where a child is generated. The recommended value for the step-size parameter is 2 [67]. The stopping criterion specifies the number of generations that are used for stopping the optimization calculation. When the adaptability of the best individual through all generations does not change within the generations specified as the stopping criteria, the optimization calculation will end as the calculation has converged. The appropriate value for stopping criteria is the maximum generations/4 [66].

Table 3-5 summarizes the properties of the GA used to solve an optimization problem with 8 optimization parameters.

Table 3-5. The properties of the GA used to solve an optimization problem with 8 optimization parameters.

Parameter	Recommended value
Population size	80
Maximum number of generations	80
Number of children	33
Step-size parameter	2
Stopping criteria	20

3.5.3 Design Optimization Considering Torque Ripple and Torque Mean Value

The proposed optimization procedure is focused on a group of objectives at different operating conditions. In this section, the optimization procedure considering T_{mean} and T_r% and

using FE software and GA is presented while the magnet dimensions are constant. Moreover, the main steps and rules of this procedure are presented.

3.5.3.1 Initial Design

The existing VFM (Fig. 3-10) with new magnet dimension obtained from the analytical design criterion is selected as the initial design to start the optimization.

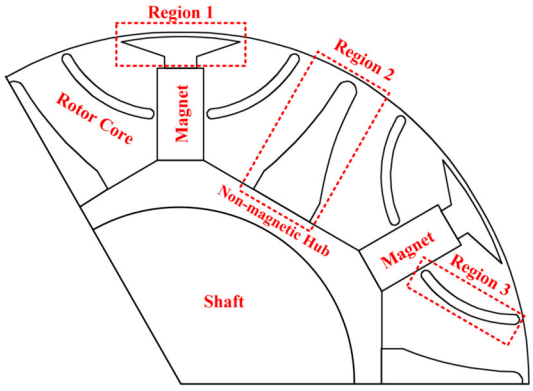

Fig. 3-10: Initial VFM topology (FE simulation).

Based on the FE simulation, three regions are selected to apply modifications to reduce $T_r\%$ and at the same time to keep T_{mean} within an acceptable range. Region 1 is an air rib above the magnet that is limiting the circulating flux on top of the magnet. The thickness of the steel layer above the air rib is chosen as small as possible which ensures its saturation during the normal operation of the VFM. The geometry of the rib specifies the rotor pole arc angle (θ_p) and controls the magnetic flux linkage and leakage. Region 2 is the main barrier of the rotor that is carved to limit the q-axis flux effects on the magnet to prevent the demagnetization of the low coercivity AlNiCo magnets during the normal operation. Region 3 is the small barriers in the rotor that divide the rotor core area into two magnetically separated areas to obtain a better control of the magnetic flux distribution in the rotor. They also limit the demagnetization effect of the q-axis magnetic flux and enhance the saliency ratio of the machine.

3.5.3.2 Parametrizing the FE Model

The geometry editor of the FE software has an in-built capability to define the CAD parameters like the length of a line, the angle between two lines, the clearance between two lines, etc. Several parameters are defined in the rotor to control the shape and the relative position of the corresponding sections. These parameters are shown in Fig. 3-11.

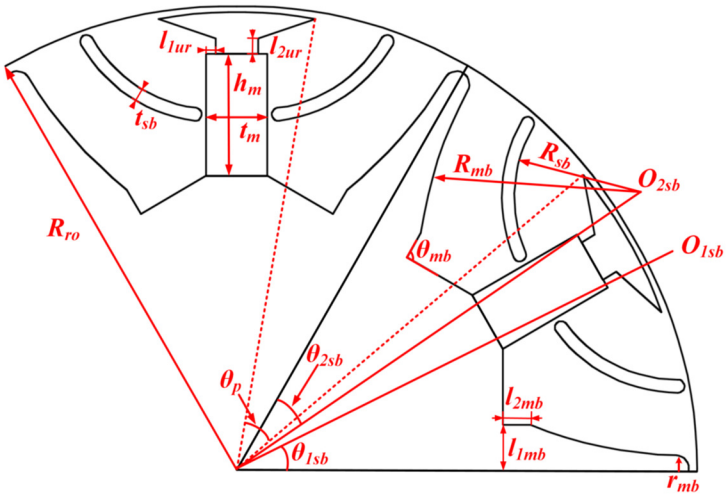

Fig. 3-11: Defined geometrical parameters in the FE model of the VFM.

Five parameters are defined in region 2 in Fig. 3-11, to modify the shape of the main barrier (*mb*) as, l_{1mb}, l_{2mb}, r_{mb}, R_{mb}, and θ_{mb}. Four parameters are considered in region 3 of Fig. 3-110, to control the shape of the small barriers (*sb*) as θ_{1sb}, θ_{2sb}, R_{sb}, and t_{sb}. Three parameters are defined in region 1 of Fig. 3-11, to change the shape of the upper rib (*ur*) as l_{1ur}, l_{2ur}, and θ_p. Table III shows a list of geometrical parameters that are defined in the FE model.

Table 3-6. The list of geometric parameter defined in the FE model.

t_m	Magnet thickness	θ_p	Pole arc angle
h_m	Magnet length	l_{1mb}	Main barrier horizontal Length
l_{1ur}	Upper rib horizontal length	l_{2mb}	Main barrier vertical length
l_{2ur}	Upper rib vertical length	r_{mb}	Main barrier upper radius
t_{sb}	Small barrier thickness	R_{mb}	Main barrier radius
θ_{1sb}, θ_{2sb}	Small barrier angle	θ_{mb}	Main barrier angle
R_{sb}	Small barrier radius	R_{ro}	Rotor outer radius

All parameters can be defined to be dependent on one master parameter from the same type or can be independent of one another. For example, for the small barriers in one pole, θ_{1sb} and θ_{2sb} are defined. θ_{1sb} can be defined as the master parameter and θ_{2sb} can be defined to be dependent on θ_{1sb}. These two parameters can be also defined with no connection. Based on the FE results, a small difference between the small barrier angles of one pole helps to reduce the torque ripple.

3.5.3.3 *Optimization Parameter Selection*

To select the optimization parameters, their effect on $T_r\%$ and T_{mean} must be studied. These parameters are varied within specified ranges and the variation of $T_r\%$ and T_{mean} are monitored. Fig. 3-12 shows the effect of l_{1mb} and l_{2mb} (main barrier shape) on both $T_r\%$ and T_{mean}.

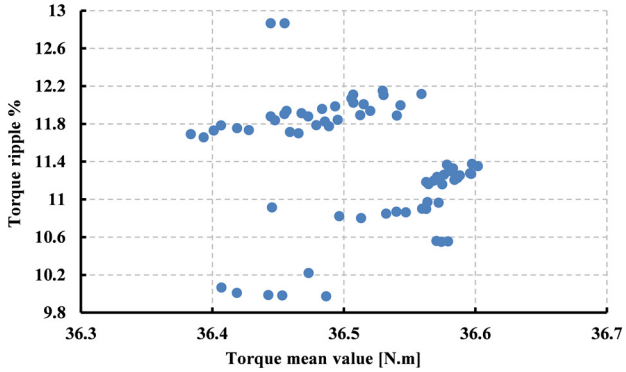

Fig. 3-12: Effect of l_{1mb} and l_{2mb} on $T_r\%$ and T_{mean}.

Based on Fig. 3-12, $T_r\%$ is reduced from 12.9% to less than 9.9%. This range of change shows the effectiveness of the main barrier shape.

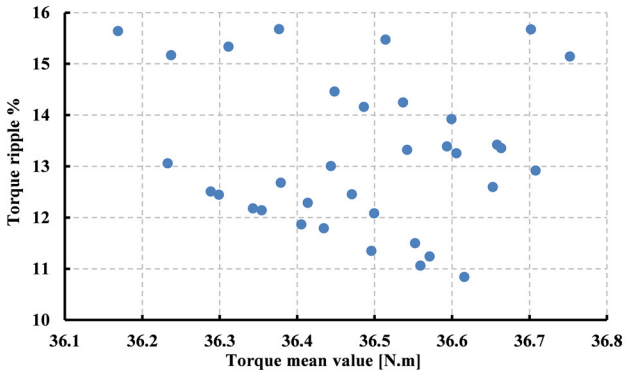

Fig. 3-13: Effect of θ_{1sb} and θ_{2sb} on $T_r\%$ and T_{mean}.

Fig. 3-13 shows the effect of θ_{1sb} and θ_{2sb} on both $T_r\%$ and T_{mean}. According to Fig. 3-13, $T_r\%$ is reduced from 15.8% to less than 11%. Moreover, Fig. 3-12 and Fig. 3-13 show that T_{mean} does not change with the mentioned parameters and this design objective is dependent on the magnet dimensions especially the magnet length. FE simulations show a small difference between these two parameters will cause $T_r\%$ reduction. Using the FE results, the parameters related to the pole arc angle, the small barrier angle, the upper rib shape, and the main barrier shape are selected to optimize the rotor design.

3.5.3.4 Initial Range Definition for the Optimization Parameter

After selecting the optimization parameters, their range of change must be defined to obtain better results. For the first optimization problem, this range is defined based on the magnetic and mechanical features of the VFM. To define the initial range of change for R_{mb}, the no-load magnetic flux lines as shown in Fig. 3-14 are considered.

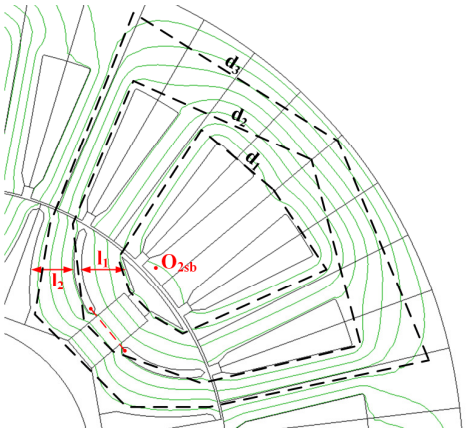

Fig. 3-14: Rage definition for R_{mb} based on the no-load magnetic flux lines.

As shown in this figure, the small barriers in each pole create two magnetically separated flux paths on each side of the magnet. Based on the FE simulation results, to reduce T_r%, R_{mb} should be selected to obtain equal reluctances for two flux paths. To fulfill the equal reluctances in these two areas ($\mathcal{R}_1$ and $\mathcal{R}_2$), (3-9) must be valid:

$$\Re_1 = \Re_2 \Rightarrow \frac{(\frac{(d_1+d_2)}{2\mu_r}+t_m+g)}{l_1} = \frac{(\frac{(d_2+d_3)}{2\mu_r}+t_m+g)}{l_2} \tag{3-9}$$

where d_1, d_2, and d_3 are the average magnetic path lengths without considering the magnet thickness as well as air gap length, and l_1 and l_2 are the magnetic path widths. The air gap length will affect the machine performance, but for this analysis, the air gap is kept constant and its effect in comparison with other parameters like t_m is negligible. Based on the center of the main barrier arc (point O_{sb} in Fig. 3-11), l_1 and l_2, the initial range of change for R_{mb} can be selected.

Fig. 3-15 shows the effect of pole arc angle on both T_{mean} and T_r%. According to this figure, a reduction of θ_p increases T_r%. On the other hand, increasing θ_p causes a reduction in T_{mean} as a result of the reduced flux leakage. Based on the FE simulation, $\theta_{p,\min}=38^\circ$ and $\theta_{p,\max}=44^\circ$ is set as the initial range for θ_p.

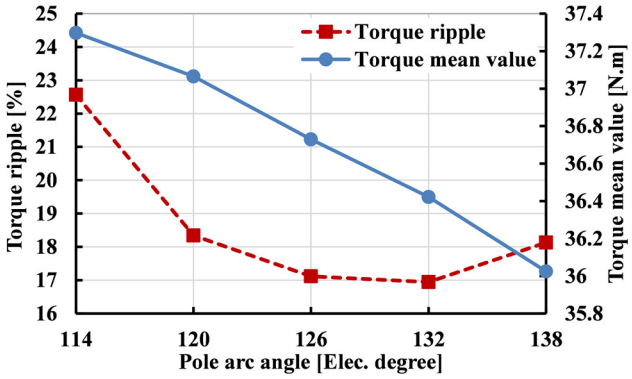

Fig. 3-15: Effect of θ_p on both T_r% and T_{mean} value (FE simulation).

To specify the range of change for the upper rib geometrical parameters, magnetic properties, and mechanical limits must be considered. Based on Fig. 3-16, an increase in l_{1ur} reduces the size of region 1 that causes more leakage flux above the magnet. A larger l_{2ur} reduces the size of region 2 that results in higher leakage flux above the magnet and non-uniformity in the magnetic flux density distribution.

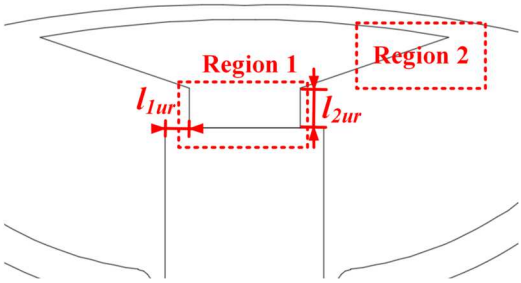

Fig. 3-16: The upper rib optimization parameters.

The range of these two parameters is decided based on a constant t_m, and mechanical and magnetic considerations. The minimum and maximum values for these two optimization parameters are 0.7 mm and 1.5 mm, respectively.

3.5.3.5 Applying Genetic Algorithm

To begin the optimization procedure, a group of initial cases is defined based on the optimization parameters and their range. To define the initial cases, the best cases of the other optimization problems and the value of the optimization parameters in those cases are considered. To find the best cases in this step, the GA is applied several times. Different combinations of optimization parameters are considered and each combination creates one

optimization problem. After solving each optimization problem, the best designs in term of torque ripple are considered as initial cases for other optimization problems with new optimization parameters and ranges. In this manner, a wide variety of parametric parameters are considered that helps to find the overall best design and prevent the selection of the local minima.

To reduce the overall time of solution for each optimization problem, the FE simulation is done for one electrical cycle, while the number of steps for each cycle is 50. With this number of steps, $T_r\%$ is lower though it provides a correct overview about all the cases. In the final evaluation of the best case for each optimization problem, the number of steps for each cycle is increased to 200. Fig. 3-17 shows $T_r\%$ and T_{mean} values for one optimization problem with five optimization parameters. According to Fig. 3-17, the selected magnet dimensions guarantees T_{mean} within the specified range (less than 3% change of T_{mean}). Moreover, seven cases with $T_r\%<9\%$ are selected as initial designs for the optimization.

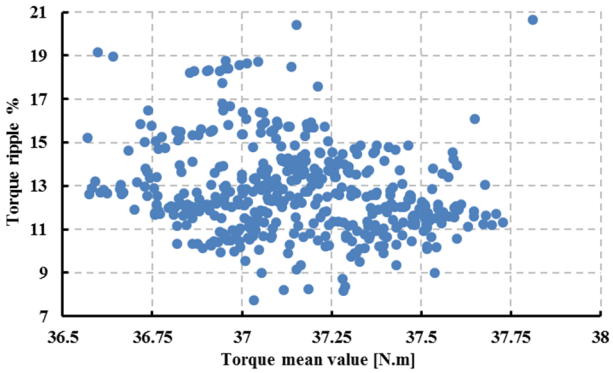

Fig. 3-17: $T_r\%$ and T_{mean} for all cases of one optimization problem.

The best case in this optimization procedure has 7.74% torque ripple once the optimization is done with 50 steps for one cycle. $T_r\%$ is 10.42% when the number of steps increases to 200.

3.5.3.6 Best Case Selection

Twenty designs as the best cases of the first step are selected for the second step of the optimization. To select one of these designs, the base speed of the machine at the different levels of the magnet magnetization is estimated and compared with the existing VFM. One of the main advantages of the VFM is that the AlNiCo magnet flux can change with a short time *d*-axis current pulse and the machine can work in the field-weakening mode of operation with reduced permanent demagnetizing current. So, the base speed of the machine at different MLs

is a parameter that is used in this step to select one case. The base speed of the machine depends on the back-EMF as well as L_d and L_q. Once the barrier shapes of machine change, L_d and L_q change and the base speed will change. The base speed of the optimized case should be greater than or equal to the same parameter of the existing VFM. To estimate the torque-speed characteristic of each design at each ML the mesh data of each simulation file is used by the FE software to simulate the VFM at different operating points. Fig. 3-18 shows the variation of the base speed at different levels of the magnet magnetization for different designs.

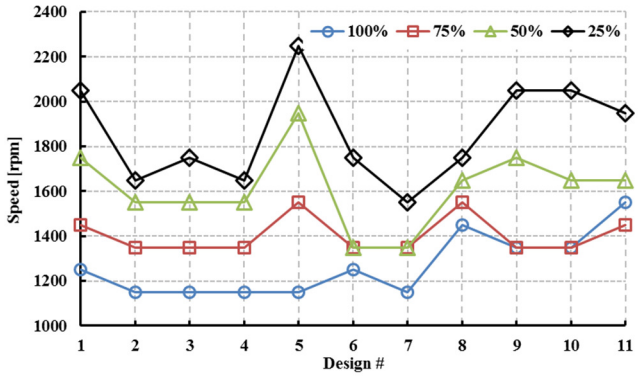

Fig. 3-18: Variation of the base speed for different designs at different levels of magnetization.

Design #1 is the existing VFM. Based on this figure, design #5 is selected since it fulfills the optimization objectives.

Table 3-7 shows the optimization parameters used to develop design #5 and their range.

Table 3-7. Optimization parameters used to develop design #5 and their range.

Geometric parameter	Range	Geometric parameter	Range
l_{1ur}	1-2 mm	θ_p	41°-44°
l_{2ur}	1.5-2.5 mm	l_{1mb}	4-6 mm
θ_{1sb}	26°-27°	l_{2mb}	3-5 mm
θ_{2sb}	26°-27°	R_{mb}	24.5-25.5 mm

Table 3-8. Comparison of the optimization parameters between design #1 and design #5.

Geometric parameter	Design #1	Design #5	Geometric parameter	Design #1	Design #5
t_m	7 mm	5.8 mm	θ_{2sb}	27.26°	26.50°
h_m	14.2 mm	15.4 mm	θ_p	40°	44°
l_{1ur}	1 mm	1.7 mm	l_{1mb}	5 mm	5.5 mm
l_{2ur}	1.65 mm	2.4 mm	l_{2mb}	3.3 mm	4 mm
θ_{1sb}	27.26°	26.75°	R_{mb}	47.21 mm	25.21 mm

Table 3-8 shows the optimization parameters used to develop design #5 and compares them with the same parameters in design #1. For design #5, $T_r\%=9.52\%$ and $T_{mean}=37.33\ N.m$. In comparison with design #1, it shows more than 50% reduction in $T_r\%$ and 2% increase in T_{mean}.

3.5.4 Magnetization Current Examination and Final Design Refinement

The magnet dimensions are kept constant during the previous step of design optimization. This step examines I_{mag} and the magnet no-load operating point for design #5 and modifies the magnet dimensions to fulfill the objectives. In order to estimate I_{mag} in the FE model, the VFM is supplied by a magnetizing *d*-axis current with an increasing amplitude until the magnet reaches the saturation flux density. The current at which the magnet saturates is considered as I_{mag}.

3.5.4.1 New Magnet Dimensions

To reduce I_{mag} in this step of the magnetization procedure, the effect of the magnet dimensions on the magnet operating points at different loading conditions, the magnet dimensions are investigated. To do this, the magnet dimensions are varied within a small range around the selected magnet dimensions in section 3.3.1 [$h_m=14.7\ mm$ and $t_m=5.6\ mm$].

3.5.4.1.1 Effect of d- and q-axes Flux on the Magnet Operating Point

Based on the experimental results and the FE simulations, the armature current affects *ML(%)* of AlNiCo magnets in the VFM machine. To study this effect, *d*- and *q*-axis flux lines should be considered. To consider the *d*-axis flux, the armature current is assumed to be zero and the flux is only as a result of AlNiCo magnets. To investigate the effect of *q*-axis flux lines, the magnets are replaced with air and the VFM is supplied with pure I_q.

Fig. 3-19 shows the *d*-axis and *q*-axis magnetic flux vector of the VFM using the FE simulation. In Fig. 3-19(a), two small red arrows show the magnetization direction of the magnet. Moreover, the black arrows show the magnetic flux path in both the rotor and the stator. Based on this figure, the magnetic flux paths are predictable based on the rotor configuration (shape of small and big barriers). If the machine is supplied with *d*-axis current and the magnet is replaced with the air for all poles, the magnetic flux pattern is as shown in Fig. 3-19(a) and its direction changes with the current direction. Based on Fig. 3-19(b), for the *q*-axis current, the magnetic flux pattern is not predictable.

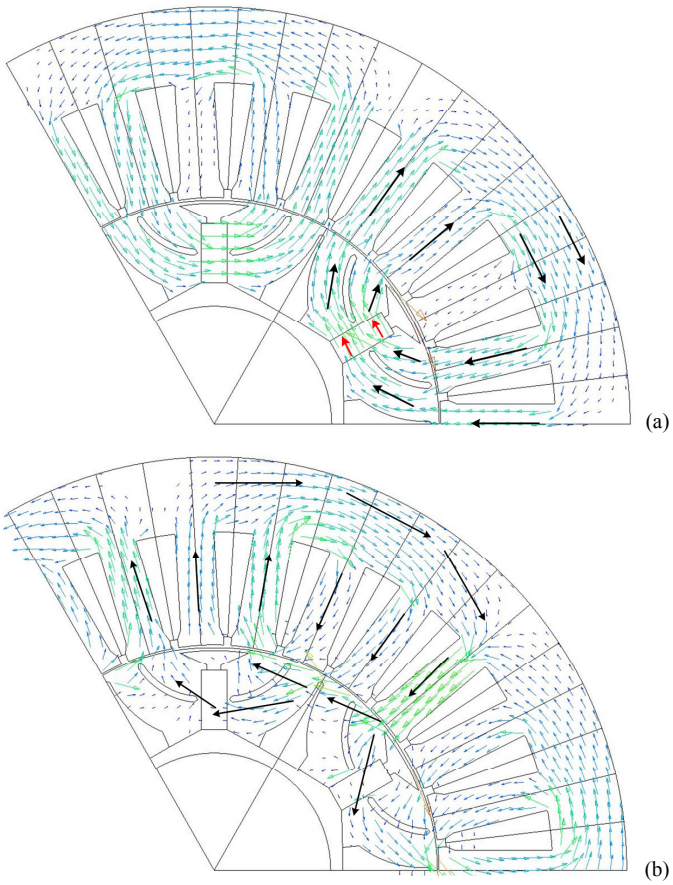

Fig. 3-19: (a): *d*-axis, (b): *q*-axis magnetic flux vectors (FE simulation).

Based on this figure, the *q*-axis flux is the main source of the non-uniformity of the magnetic flux density in the rotor at the loaded condition and it is clear that magnetic flux lines have the tendency to go through part of the magnet and affects its flux density through the magnets. According to this figure, the pure *q*-axis current in the armature is an extreme condition regarding the demagnetization of the magnets. This operating condition is one of the conditions that should be taken into account during the magnet dimension selection.

Fig. 3-20 shows the magnetic flux pattern in the rotor when the fully magnetized VFM is supplied with a pure *q*-axis armature current. In Fig. 3-20, the red arrows show the magnetization direction of the magnets. The non-uniform magnetic flux pattern of Fig. 3-20 can be described based on the magnetic flux patterns of Fig. 3-19(b). The effects of *q*-axis current on the flux pattern in the magnets and in the specified areas (dashed boxes) are clear. In those areas, the *q*-axis magnetic flux arrows oppose the magnetic flux arrows as a result of the magnets. In the lower parts of the magnets, this effect is obvious.

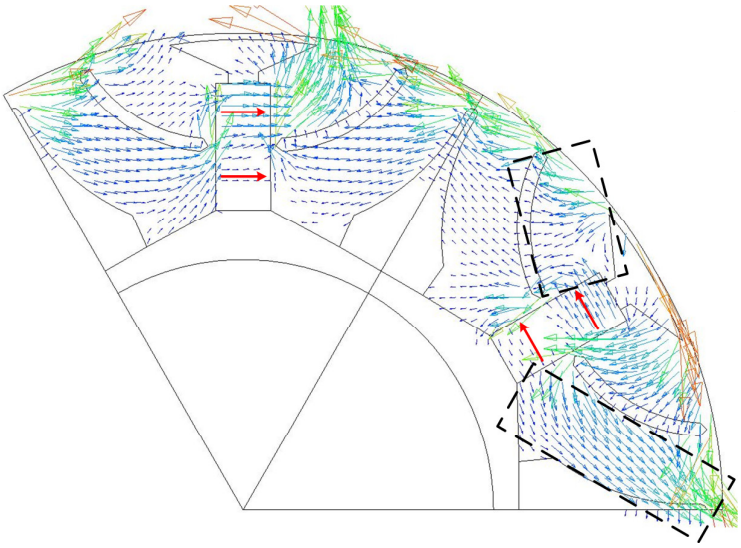

Fig. 3-20: The magnetic flux pattern in the rotor of the VFM with *q*-axis armature current and AlNiCo 9 magnets.

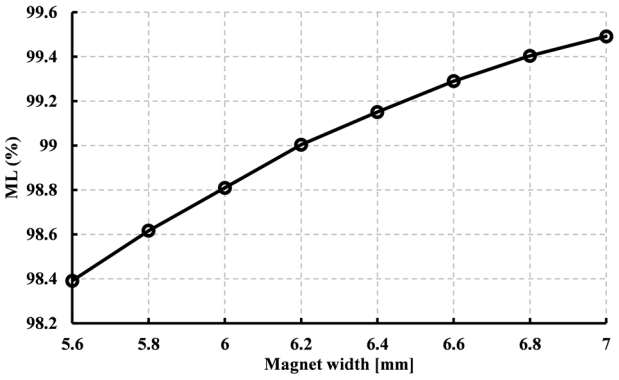

Fig. 3-21: Effect of (a): the magnet width, and (b): the magnet length, on the *ML(%)* of the magnet at no-load condition (FE simulation).

3.5.4.1.2 No-load Condition

The operating point of the magnet at the no-load condition is related to the magnet and the air gap dimensions. Fig. 3-21 shows the effect of the magnet width and the magnet length on

the *ML(%)* of the magnet at the no-load condition. For Fig. 3-21(a), the magnet length is assumed to be constant. With an increase in the magnet thickness, the *ML(%)* is enhanced. Based on this figure, a 25% increase in t_m increases the *ML(%)* by 1%. This increase in t_m increases I_{mag} from 33 A to 40 A. In Fig. 3-21(b), the magnet width is assumed to be constant. According to this figure, the *ML(%)* is an incremental function of h_m with a very small slope that means h_m does not have too much effect on the *ML(%)* at the no-load condition.

3.5.4.1.3 Loaded Condition (Pure q-axis Current Pulse)

The proposed VFM is a spoke type to reduce the effect of *q*-axis flux on *ML(%)* of the magnet. This section analyses the effect of *q*-axis flux on the *ML(%)* for different magnet dimensions. Fig. 3-22 shows the effect of the magnet width and the magnet length on the *ML(%)* when the machine is supplied with pure I_q current.

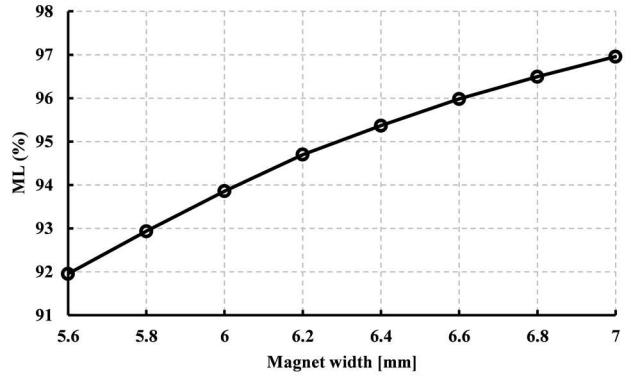

Fig. 3-22: Effect of (a): the magnet width, (b): the magnet length, on the *ML(%)* of the magnet for the VFM that is supplied with *Iq* (FE simulation).

For Fig. 3-22(a), with an increase in the magnet width, the *ML(%)* is enhanced. Based on this figure, a 25% increase in the magnet width increases the *ML(%)* by more than 5% and in comparison with Fig. 3-22(a), it is obvious that the magnet width has a large effect on the

ML(%) of the magnet when the machine is supplied with I_q. Based on Fig. 3-22(b), an increase in the magnet length reduces the ML of the magnet at the mentioned operating condition and a 5% increase in the magnet length reduces the *ML(%)* by 1.5%.

3.5.4.1.4 Summarizing the Results and the Magnet Dimensions Selection

According to Fig. 3-21(a) and Fig. 3-22(a), when t_m increases the *ML(%)* of the magnet at both no-load and loaded conditions are improved, and t_m also has a greater effect on the loaded condition. Moreover, an increase in t_m will increase I_{mag}. This means that to select t_m, a tradeoff should be considered between the *ML(%)* of the magnet at the no-load condition and I_{mag}. Based on FE simulations, $T_{PM,mean}$ increases with an increase in the magnet length and based on Fig. 3-21(b) and Fig. 3-22(b), the *ML(%)* of the magnet in both loading conditions decreases. This means that a tradeoff should be considered between the *ML(%)* of the magnet in the loaded condition and $T_{PM,mean}$ for the magnet length selection. Using Fig. 3-21 and Fig. 3-22, the magnet thickness is selected at 6.2 mm to have *ML(%)* more than 99% and 95% at the no-load condition and when the motor is supplied with I_q, respectively.

Fig. 3-23 shows the effect of magnet length on *ML(%)* of the magnet when the VFM is supplied with pure I_q.

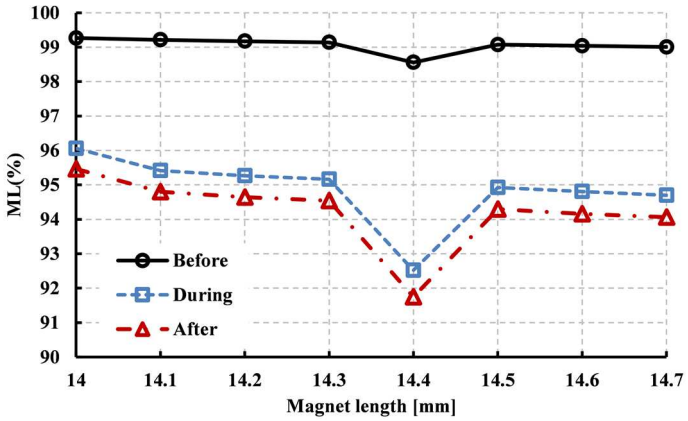

Fig. 3-23: Effect of magnet length, on *ML(%)* of the magnet at different operating points for t_m=6.2 mm (FE simulation).

Before and after the I_q current pulse is the no-load condition. Based on this figure, for $h_m<14.3$ *mm*, *ML(%)* at the no-load condition before the pulse is more than 99%. Moreover, as a result of rated I_q, *ML(%)* will be more than 95% during the pulse and 94.5% at the no-load condition after the pulse. Also, with $h_m=14.4$ *mm*, there is a larger drop in *ML(%)* at different

operating conditions. To have a tradeoff between *ML(%)* and $T_{PM,mean}$, h_m is selected to be 14.3 mm.

3.5.4.2 Selection of Optimization Parameters and Initial Range

In this step of optimization, the optimization parameters must be selected so that they do not have a negative effect on I_{mag} and the no-load operating point of the magnet. According to the FE simulations, l_{1ur}, l_{2ur}, l_{1sb} and l_{2sb} (Fig. 3-24) are chosen. The range of change for l_{1sb} and l_{2sb} is defined based on both the mechanical and magnetic considerations. The minimum value for each of these parameters is defined based on the cutting and mechanical limitations of the laminations.

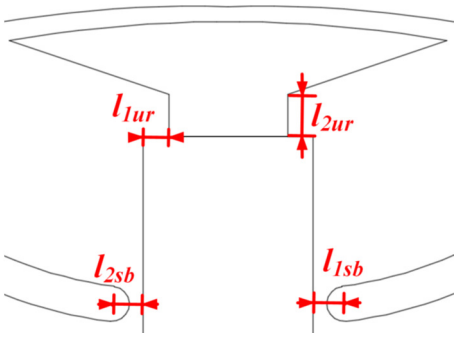

Fig. 3-24: New optimization parameters with the minimum negative effect on Imag and the no-load operating point of the magnet.

Moreover, the clearance between the magnet and the small barrier cannot increase more than a maximum value since it causes non-uniformity in the magnetic flux density distribution. These two parameters are defined independently in the range of $l_{isb,\min}=1.6\ mm$ and $l_{isb,max}=3\ mm$.

3.5.4.3 Applying Genetic Algorithm

The optimization parameters and their ranges are specified and the initial cases are defined manually to minimize T_r% as the objective function. For the first three optimization problems, all four optimization parameters are selected. To solve each optimization problem, based on the initial cases, more than 40 generations of the GA are applied to modify the design. After 20 times of using GA to optimize the model with different sets of optimization parameters, the T_r% variation is almost zero. Therefore, the obtained design at this stage is selected as the optimized design.

3.5.5 Flowchart of the Optimization Procedure

Fig. 3-25 shows the overall flowchart of the optimization procedure. As shown in Fig. 3-25, the optimization procedure consists of two levels. The magnet dimensions are selected using the analytical design criterion in the first level (block (1) in the flowchart). The FE software and the GA are used to perform the optimization in the second level (blocks (2) to (13) in the flowchart). In this level, the existing topology of the VFM with new magnet dimensions from the first level is selected as the initial design.

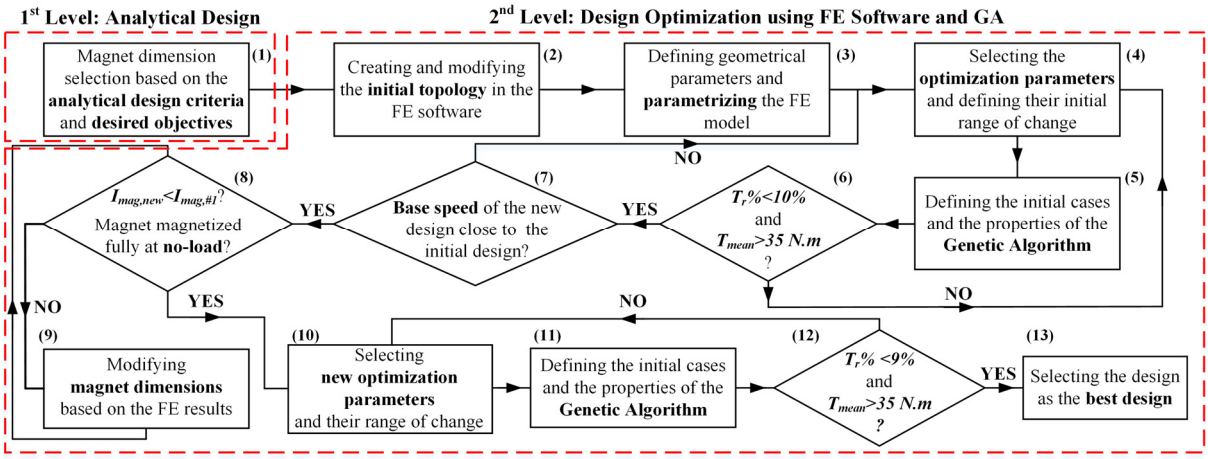

Fig. 3-25: The overallflow chart of the optimization procedure.

As explained in block (3), the FE model is parameterized. In block (4) the optimization parameters and their range are defined to create the optimization problem. In block (5), the properties of the GA are selected and the optimization objectives are defined. Block (6) checks the best case of the optimization problem. If the best case fulfills the objectives, the design will be selected for the next step. Otherwise, the procedure will go back to block (4) to define a new set of optimization parameters, and as a result, a new optimization problem. The selected designs in block (6) are checked in block (7) to select one design to go for checking the magnetization current and the no-load operating point of the magnet that happens in block (8). If the selected design doesn't fulfill the required values of magnetization current and no-load magnet operating point, the magnet dimensions are slightly modified as explained in block (9) and then the procedure will go to block (8) to recheck I_{mag} and the magnet operating point in the no-load condition. Otherwise, the procedure will go to block (10) to continue the T_r% reduction with lower negative effects of I_{mag}. In block (10), new optimization parameters with

lower negative effects on the magnetization current are selected to perform the optimization procedure. The range of these parameters and the properties of GA are defined in block (11). Block (12) checks the design objectives for the best case of each optimization problem. If the case doesn't meet the required optimization objectives, the procedure goes back to block (10) to select a new set of optimization parameters. The case that fulfills the optimization objectives is selected as the best case in (13).

3.5.6 Optimized Design, Results, and Discussion

Fig. 3-26 shows the rotor topology of the existing VFM and the optimized design. The differences between these two designs are in the magnet dimensions, the main barrier shape, the rotor pole arc angle, the upper rib shape and the small barriers angle. The magnet dimensions for the existing VFM are 7 mm×14.2 mm while for the optimized case are 6.2 mm×14.3 mm. Based on a similar stack length (120 mm). The optimized design shows more than 11% reduction in the magnet volume.

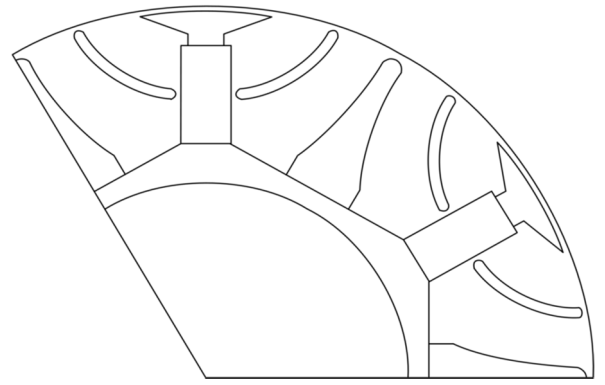

(a)

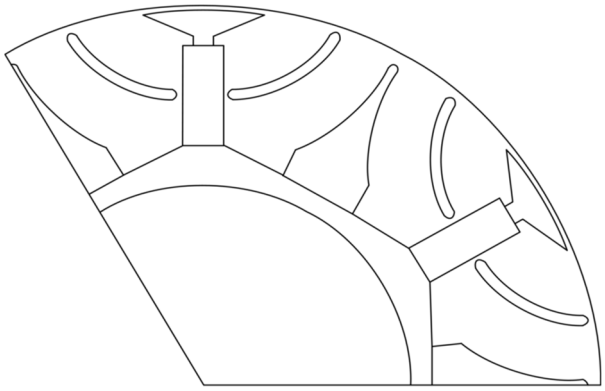

(b)

Fig. 3-26: Rotor topology (a): the existing VFM, and (b): the optimized design.

In this topology, the rotor core is attached to the shaft using a non-magnetic hub. For both existing and optimized designs, the ribs above the magnets and the main barrier, as well as the small barriers, keep the rotor components together. In the optimization procedure, to select the range of change for each geometric parameter, the minimum is selected based on the existing design. Based on Fig. 3-26 , the rib thickness for the optimized design is larger than the existing design that improves the mechanical integrity of the optimized design.

Fig. 3-27 shows the torque waveform for both designs at full load and 100% magnetization level. According to Fig. 3-27, T_{mean} for the initial, and the optimized designs are 36.7 N.m, and 35.1 N.m, respectively. The peak to peak value of torque for the initial and the optimized designs are 7.2 N.m, and 2.9 N.m, respectively. As a result, T_r% is 19.5% for the initial case and 8.3% for the optimized design. These values show a 4.4% reduction in T_{mean} and more than 57% reduction in T_r% for the optimized case.

Fig. 3-28 compares the no-load phase back-EMF of both designs. The RMS values of the phase no-load back-EMF for the initial and the optimized cases are 124.3 V and 119.8 V, respectively that shows 3.7% reduction for the optimized design.

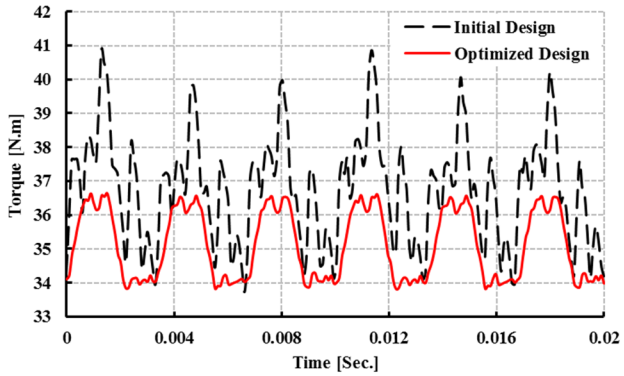

Fig. 3-27: Comparison of the torque waveform for the initial design and the optimized design.

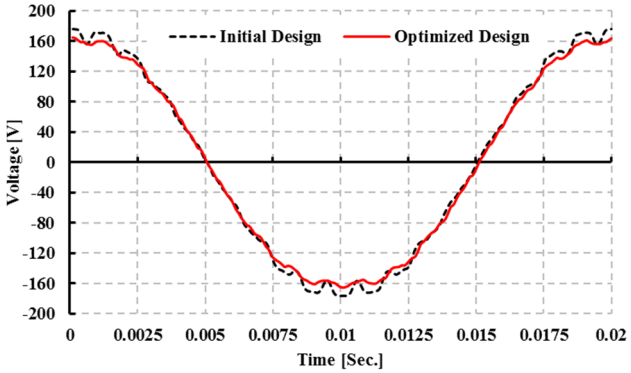

Fig. 3-28: Comparison of the no-load phase back-EMF for the initial design and the optimized design.

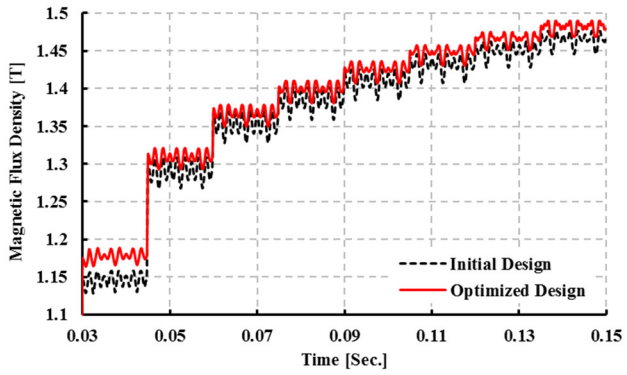

Fig. 3-29: Comparison between the initial design and the optimized design, the average flux density of the magnet during the magnetization procedure.

Fig. 3-29 shows the average flux density of the magnet during the magnetization procedure. Based on this figure, the same amplitude of magnetization current produces more magnetic flux density in the magnets of the optimized design. Thus, the optimized rotor requires lower magnetization current. Based on the FE simulation and test, I_{mag}=40 A for the initial design. Based on the FE simulation, I_{mag}=35 A for the optimized design which shows more than 12.5% reduction.

3.6 Conclusion

A two-level design optimization method for a spoke type VFM with AlNiCo 9 magnets was presented in this chapter. To do the optimization, the characteristics of the existing VFM were reviewed and the problem and its limitations were also discussed. A measurement technique was developed to measure the torque waveform and verify the FE model of the VFM. An optimization strategy was proposed to reduce $T_r\%$ to less than 10% and reduce I_{mag} by 12.5% and maintain T_{mean} close to the torque mean value of the existing VFM. Moreover, the no-load magnet operating point was examined for the optimized cases. An analytical design criterion was proposed to estimate the magnet dimensions based on the desired values of T_{mean} and I_{mag} and was verified using FE results. The application of GA as an optimizer was discussed and the main guidelines were presented. The main rules for optimization parameters selection and their range definitions were proposed. The GA was applied to find the cases with reduced torque ripple and the torque mean value close to the existing VFM. The magnet dimensions of the best case were modified to reduce the magnetization current and also keep the AlNiCo magnets fully magnetized at the no-load conditions. After performing the optimization, the optimized case

with 11% reduction in the magnet volume, 57% reduction in the torque ripple, 4.4% reduction in the torque mean value and 12.5% reduction in the magnetization current is chosen.

Chapter 4. Design of an AlNiCo-Based Variable Flux Machine with Enhanced Power at the High-Speed Region

4.1 INTRODUCTION

The application of low coercivity magnets provides the ability of magnetization and demagnetization of the rotor magnets using a short-time *d*-axis current pulse that improves the efficiency of the machine in the high-speed region. This short-time *d*-axis current produces a negligible loss. For the conventional rare-earth PMSM, in the field-weakening mode of operation, a permanent demagnetizing current is needed to reduce the magnet flux and keep the terminal voltage within the system limitations. For the VFM with reduced ML, the core losses are also reduced in the high-speed region. As a result, the VFM can work with high efficiency for a wider range of speed while the conventional rare-earth PMSM suffers from lower efficiency at high-speed. [68] reports 30% loss reduction for the urban driving cycle of an electric vehicle (EV) using a VFM.

According to the value of *d* and *q* axes inductances, the saliency ratio (χ) is defined. The conventional PMSMs are designed with $L_d<L_q$ that causes the positive reluctance torque in the field-weakening operation. However, due to the large L_q, the *q*-axis armature field is quit high specifically at higher currents which can lead to the low coercivity magnet demagnetization in the VFMs.

The flux intensifying designs with $L_d>L_q$ (inverted saliency designs) have been proposed in [39]-[41], [69] to reduce the demagnetizing effect of the *q*-axis armature current. Due to the machine inverted saliency, the reluctance torque in the field-weakening region is negative which leads to torque and power capabilities reduction in that region.

The characterization of the torque-speed envelope is an important step in the design of PMSMs, specifically for the field-weakening mode of operation [41], [70], [71].

[40] presents the torque-speed characteristics of a VFM with flux intensifying design, considering constant L_d and L_q. [69] proposes a flux intensifying design of a PMSM and compares the torque-speed characteristics of this design with a conventional PMSM design. [39] shows the torque-speed envelop of a VFM with inverted saliency at MLs from 100% to 0% with 25% intervals.

As the VFM has the capability of operating at different MLs, the torque-speed envelope characterization method should be able to consider the demagnetization of the magnets, and the variation of L_d and L_q based on the operating condition.

This chapter focuses on a new design of AlNiCo-based radially magnetized VFM with conventional saliency to keep the promising features of the VFM and enhance its power and torque capabilities in the field-weakening region. To achieve this, a VFM is designed with interior magnets positioned to keep the fully magnetized condition at no-load, withstand the demagnetizing effect of *q*-axis armature flux, and be able to get demagnetized and re-magnetized using the *d*-axis current pulse. Moreover, the design is optimized to have minimized torque ripple, and at the same time maximized power and torque capabilities.

In this chapter, the torque-speed characterization method considering the demagnetization of AlNiCo magnets is proposed in Section 4.2. Section 4.3 discusses the design of a tangentially magnetized VFM. Section 4.4 shows the FE-based optimization of the proposed tangentially magnetized VFM. Section 4.5 presents the optimized radially magnetized design and compares it with the initial design. Section 4.6 concludes the chapter.

4.2 Torque-Speed Characterization Considering the AlNiCo Magnets Demagnetization

The torque-speed characteristics of the AlNiCo-based VFM are calculated using the inductance, and flux linkage matrices from the FE model of the machine, as well as the *dq* model equations. According to the *dq* model of the PMSM, the output torque (T) of the machine is represented using

$$T(I_d, I_q) = 3\frac{P}{2}\left(\lambda_m(I_d, I_q) + \left(L_d(I_d, I_q) - L_q(I_d, I_q)\right)I_d\right)I_q \tag{4-1}$$

where I_d and I_q are *d* and *q* axes currents, respectively. L_d and L_q are *d* and *q* axes inductances in H, respectively. λ_m and P are the magnetic flux produced by the magnets in Wb and the number of pole pairs. In (4-1), L_d, L_q, and λ_m are considered as functions of the current vector. To calculate the torque matrix for each operating condition, the matrices of *dq* inductances and magnet flux from the FE software are used.

The *d* and *q* axes voltages (V_d and V_q) of this machine are then represented as

$$V_d(I_d, I_q) = R_s I_d - \omega L_q(I_d, I_q) I_q \tag{4-2}$$

$$V_q(I_d, I_q) = R_s I_q + \omega \lambda_m(I_d, I_q) + \omega L_d(I_d, I_q) I_d. \tag{4-3}$$

R_s and ω are the stator resistance in Ohm, and the rotor electrical speed in rad/sec, respectively. The amplitude of both voltage and current vectors (V_s, I_s) based on the value of their *d* and *q* axes components are

$$V_s = \sqrt{V_d^2 + V_q^2} \tag{4-4}$$

$$I_s = \sqrt{I_d^2 + I_q^2}. \tag{4-5}$$

Based on (4-2) and (4-5), the PMSM terminal voltage is dependent on the rotor speed, and the voltage limit of the drive system should be considered for operation above the base speed. The maximum achievable voltage on the machine phases is a function of the DC bus voltage (V_{DC}) as

$$V_m = \frac{V_{DC}}{\sqrt{3}}. \tag{4-6}$$

To develop the torque-speed characteristics below the base speed of the machine, the maximum value of the torque matrix is considered. For a speed above the base speed of the machine, the voltage limitation should also be considered as

$$V_s \leq V_m. \tag{4-7}$$

This means that the torque matrix is estimated only for the current vectors which fulfill the voltage limit of (4-7), and then the maximum torque is extracted for the considered speed.

To operate above the base speed in the field-weakening region, the PMSM should be supplied with a negative *d*-axis current. For the AlNiCo-based VFM, as the negative *d*-axis current has a demagnetizing effect, the maximum allowable demagnetization of the magnets should be taken into account to develop the torque-speed envelope. Using the demagnetization characteristics of the VFM at each ML, and considering the maximum allowable demagnetization, a limit for the negative *d*-axis current (I_{dm}) can be defined. For example, the 90% allowable demagnetization for a fully magnetized condition means that the VFM can be

supplied with a negative *d*-axis current that reduces the ML to 90% during the field-weakening. As a result, the *d*-axis current limitation can be defined as

$$\left|I_d\right| \le \left|I_{dm}\right|. \tag{4-8}$$

The torque matrix above the base speed is developed only for the current vectors which fulfill (4-7) and (4-8), and the maximum torque is extracted for the considered speed.

4.2.1 Torque-Speed Characteristics for the Existing VFM

To develop the torque-speed characteristics of the existing VFM at each ML, the FE model of this machine is used and the L_d and L_q matrices as a function of the current vector amplitude and angle are extracted. The torque angle changes between 45° to 180°. I_d is positive between 45° to 90° and is negative between 90° to 180°. Fig. 4-1 shows L_d and L_q of the existing VFM in fully magnetized condition from FE simulation.

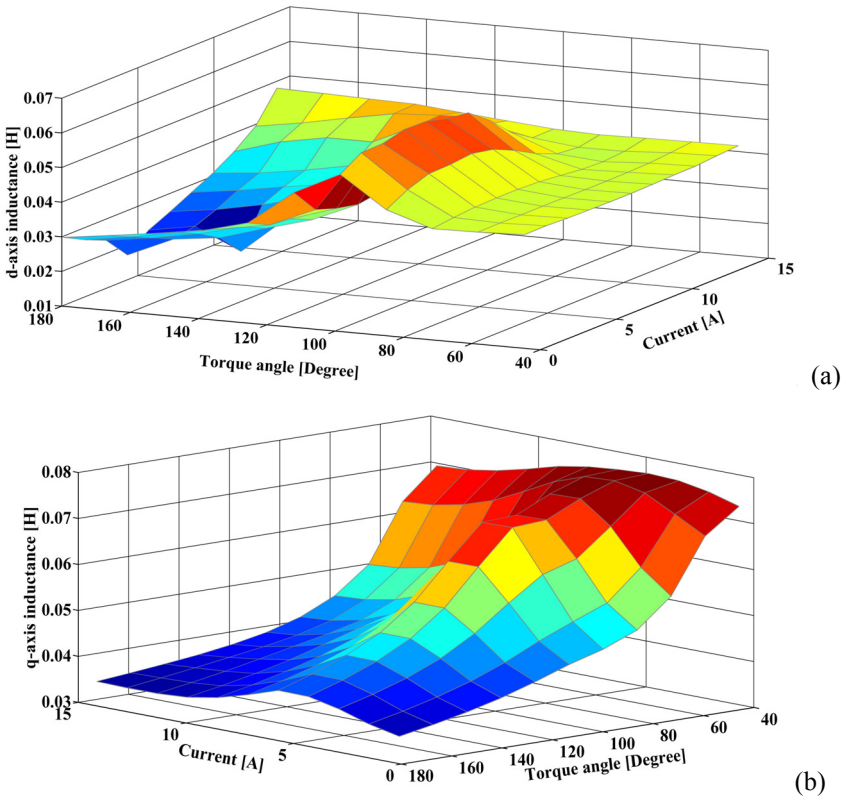

Fig. 4-1: Inductances as a function of current vector amplitude and angle for fully magnetized VFM, (a): *d*-axis inductance, (b): *q*-axis inductance, (FE results).

According to Fig. 4-1, both L_d and L_q vary with the current vector and the assumption of constant inductance with current may cause error in the performance analysis of the machine.

In this machine, L_d varies between 12.4 mH to 63.1 mH and L_q changes between 35.1 mH to 71.7 mH in the proposed range of the current vector. Moreover, the comparison between Fig. 4-1(a) and (b) shows that the existing VFM has the inverted saliency in the maximum power point region.

Fig. 4-2 shows the effects of the current vector on the magnet flux (λ_m).

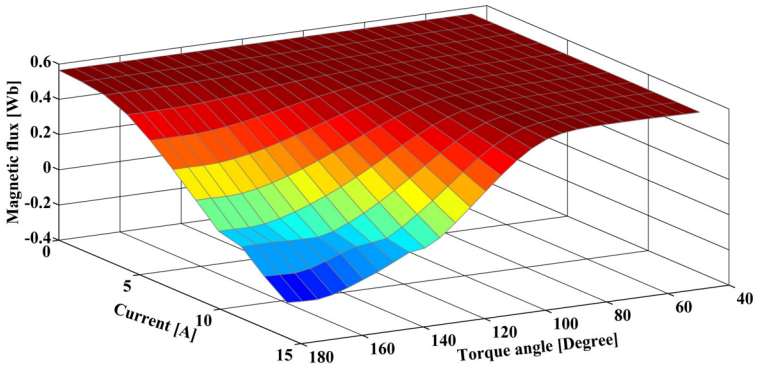

Fig. 4-2: Magnet flux as a function of current vector amplitude and angle for the fully magnetized VFM, (FE results).

To develop $\lambda_m(I_d, I_q)$ characteristic, the VFM is supplied with different current vectors, and the amplitude of the magnet flux is obtained after the current is removed. For torque angles less than 90°, as the *d*-axis current is positive, the magnet flux is constant. For toque angles larger than 90°, the *d*-axis current is negative and it has the demagnetization effect. This effect is enhanced when the current is increased. This means at larger current and torque angle values the magnet is more demagnetized. At some operating points, the magnet flux is negative, which means that the negative *d*-axis current not only demagnetizes the magnet, but also magnetize it in the other direction. Fig. 4-3 presents the demagnetization characteristics of the existing VFM at different MLs.

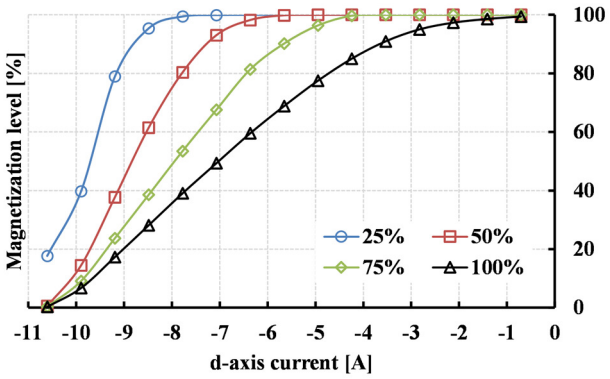

Fig. 4-3: Demagnetization characteristics of the existing VFM at different MLs, (FE results).

According to this figure, the fully magnetized VFM is partially demagnetized with a small negative *d*-axis current and is fully demagnetized with a demagnetizing *d*-axis current pulse of -10.6 A. Moreover, at lower MLs, more current is needed to demagnetize the machine and as a result the maximum allowable negative *d*-axis current increases. For instance, if the maximum allowable demagnetization in each level of magnetization considered 90%, the maximum negative *d*-axis current for 100%, 75%, 50%, and 25% MLs are -3.5 A, -5.6 A, -7.3 A, and -8.7 A, respectively.

Fig. 4-4 shows the torque-speed and power-speed characteristics of the existing VFM for the allowable demagnetization of 95% considering the AlNiCo magnets demagnetization.

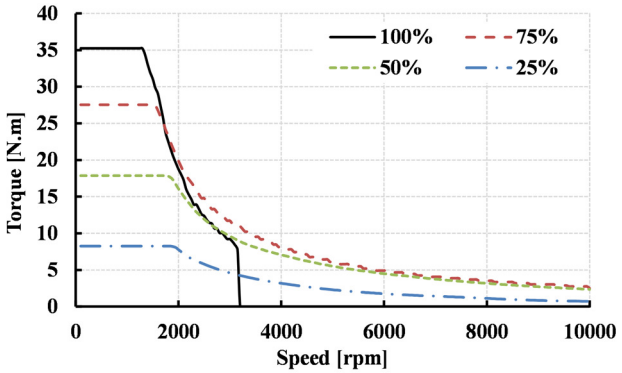

(a)

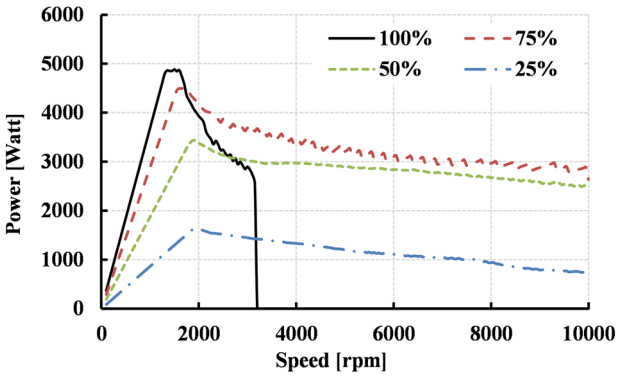

(b)

Fig. 4-4: (a): Torque-speed characteristic, and (b): Power-speed characteristic of the existing VFM at different MLs, with 95% allowable demagnetization (proposed method).

Based on Fig. 4-4, for the fully magnetized VFM and for speeds more than 3150 rpm, there is no operating condition (current vector) that fulfills the voltage and *d*-axis current limits. To operate at higher speeds with the fully magnetized machine, the maximum allowable negative *d*-axis current should be increased to reduce the magnet flux and as a result, meet the voltage limit. At the same time, this increase is not helpful as Fig. 4-4(b) shows that the output power

of a fully magnetized VFM after 2000 rpm is less than the output power at MLs of 75% and 50%. According to Fig. 4-4(b), the output power of the existing VFM decreases above the base speed which is more severe for the fully magnetized machine. For example, the existing VFM at the speed of 10000 rpm loses 42% of its maximum power that occurs at 1700 rpm. The main reason for this power drop is the inverted saliency of this machine. According to (4-1), $L_d > L_q$ results in the negative reluctance torque for $I_d < 0$, This reduces the total torque of the machine for speeds above the base speed. As the existing VFM is interior PMSM with spoke-type topology, it has high torque ripple as measured and reported in section 3.2.3. The high torque ripple may limit the application of electrical motors in industries. As a result, the torque ripple is a parameter that is considered during the design and optimization of the new VFM.

4.3 Radially Magnetized Topology of Variable Flux Machine

The stator of the new design is the same as the existing VFM, 27-slot, 6-pole with double layer winding. As the AlNiCo magnet can be demagnetized easily, the rotor replacement of this machine is less complicated in comparison with rare-earth PMSMs. On the other hand, the fixed stator design limits the rotor design, in term of the number of poles and outer diameter.

4.3.1 Magnet Orientation

To design a VFM with an enhanced torque and power capabilities at the field-weakening region, a 6-pole design of rotor with radially magnetized interior magnet is selected as this design can provide a positive reluctance torque in the field-weakening region.

Fig. 4-5 shows one pole of the rotor of the radially magnetized machine. The magnet shape is an important factor in the PMSM design as it affects the magnet price.

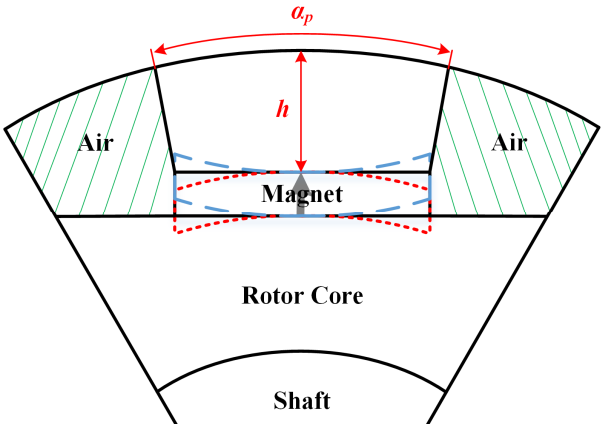

Fig. 4-5: Radially magnetized variable flux motor.

Three topologies of the magnet, concave-up (dashed blue line), concave-down (dotted red line) and rectangular magnets (solid black line) are shown in Fig. 4-5 as the possible choices. The V-shape magnet topology can be considered as a concave-up magnet with more depth and a barrier in the middle of the magnet. Due to the low coercivity of AlNiCo magnet, the VFM should be designed to be fully magnetized in the no-load condition. FE analysis shows that for both concave magnets, the edges of the magnet will be partially demagnetized in the no-load condition, which reduces the overall ML and torque capability of the VFM. Moreover, in the concave-up design, with an increase in the curve radius, the partial demagnetization is more severe. Besides, the design with rectangular magnet shows more promising results in term of the magnet operating point in the no-load condition. As the rectangular shape of the magnet is the basic shape of magnet that is provided by magnet manufacturers, this shape is also economically preferable.

4.3.2 Barrier shape

The barrier dimensions affect parameters like torque mean value, torque ripple, I_{mag}, L_q, and L_d. To have a better understanding of the barrier shape in the proposed topology, Fig. 4-6 shows d and q axes flux lines in this topology.

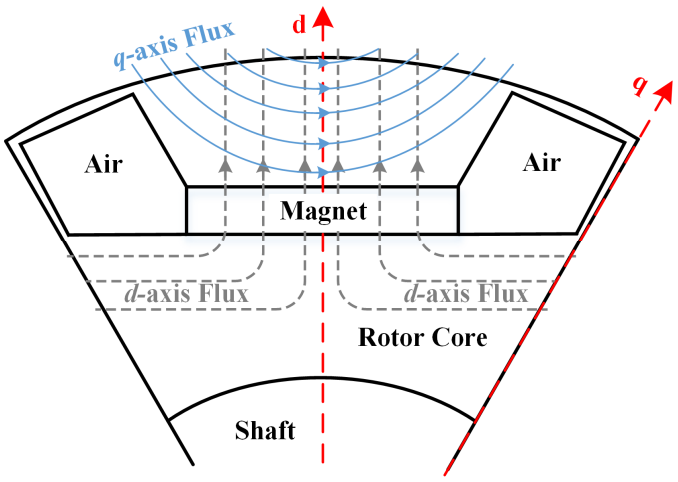

Fig. 4-6: d and q axes flux lines in the radially magnetized design.

The main role of the barriers on both sides of the magnet is to reduce the leakage flux. It can also be seen from Fig. 4-6 that the magnets are buried at a relatively larger depth from the rotor surface in order to allow the q-axis armature flux to flow through the steel area above the magnet, thus reducing the irreversible demagnetization effects of the armature q-axis current

component. As shown in Fig. 4-5, the pole arc angle (θ_p) is defined based on the shape of the barriers. θ_p affect the flux linkage of the machine and as a result, the torque mean value. Moreover, its effect on the torque ripple of the machine is reported in section 3.5.3.4. With the reduction of θ_p, the d-axis armature flux coming from the stator to the rotor is reduced. This means higher current is required to magnetize or demagnetize the magnet, which is not preferable in VFMs. Besides, as it is clear in Fig. 4-6, θ_p affects the reluctance of d-axis flux path and as a result L_d in this topology of the VFM.

The barrier shape and h (as defined in Fig. 4-5) affect the reluctance of the q-axis flux path and as a result L_q. The clearance between the barriers and the rotor surface affects the torque ripple of the machine that will be discussed in more depth in section 4.3.3.

4.3.3 Magnet and Air Gap Dimensions

Due to the armature reaction, the edge of the magnets can get partially demagnetized [40]. The magnitude of this distorting effect varies with the spatial distribution of the stator MMF that is related to the stator design, current phase, magnet dimensions, air gap length, and the magnet position (h), shown in Fig. 4-5.

To select the magnet dimensions for the VFM, as explained in section 3.3, the full load torque and the magnetizing current of the machine should be considered. Besides, the no-load operating point of magnet should be also considered. Fig. 4-7 shows the B-H curve of AlNiCo 9 magnet at different MLs and the no-load operating point of the magnet. Based on Fig. 4-7, the no-load operating point of the magnet for fully magnetized magnet [point (1)] is the intersection of the air gap line (PC line), and the B-H loop in the second quadrant.

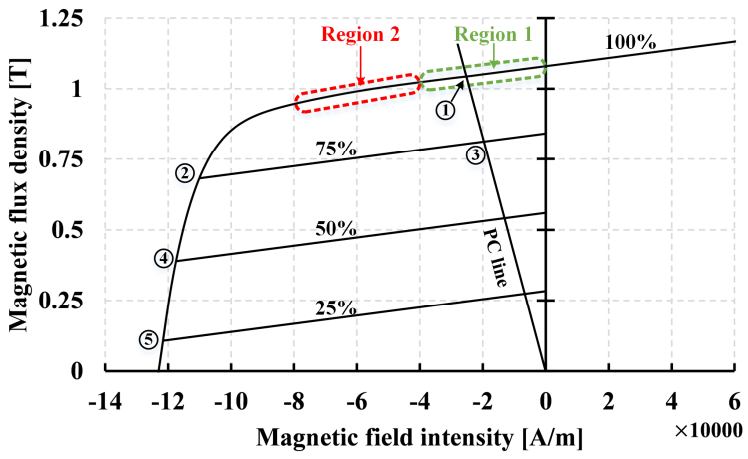

Fig. 4-7: B-H curve of AlNiCo 9 at different MLs and the magnet operating point.

According to (2-10), the no-load operating point of the magnet is a function of the magnet and air gap dimensions. To prevent the partial demagnetization, the magnet and air gap dimensions should be selected to keep the no-load operating point of the magnet within region 1 in Fig. 4-7. Lower magnet thickness, which results in a lower I_{mag}, decreases the absolute value of *PC* and move the no-load operating point towards region 2. In region 2, the risk of magnet partial demagnetization increases.

For the new design, the air gap length is initially assumed to be 0.50 mm. An increase in the air gap length reduces the absolute value of *PC*, which moves the no-load operating point of the magnet towards region 2 in Fig. 4-7, and results in the partial demagnetization of the magnet. Besides, the higher air gap length increases the air gap reluctance which causes flux linkage reduction, as well as an increase in I_{mag}.

As the stator dimensions and winding design are kept constant, the maximum limit of the magnetization current for the new design is considered the same as the existing VFM, 40 A. According to the mentioned design objectives and to provide the same rated torque as the existing VFM, the variation ranges for both the magnet length and the magnet thickness are defined as 24 mm$<h_m<$26 mm and 4 mm$<t_m<$5 mm. Within the mentioned ranges of the magnet dimensions, the resultant VFM will operate with a rated torque close to 36 N.m and $I_{mag} \leq 40\ A$ and the magnet is almost fully magnetized in the no-load condition. FE simulations show that the reduction of the magnet thickness to less than 4 mm decreases I_{mag}, but causes the magnet to be partially demagnetized in both no-load and loaded conditions. The clearance between the magnet and the rotor outer surface (*h* in Fig. 4-5), affects the ML of the VFM in both no-load and loaded conditions. Fig. 4-8 shows the effect of *h* in mm on the *ML%* of the magnet at the no-load condition for a design with the rectangular magnet and fixed dimensions.

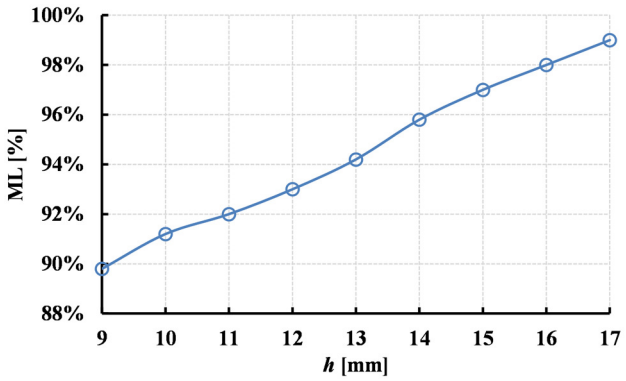

Fig. 4-8: *ML%* of magnet vs. *h* (FE simulation).

Based on Fig. 4-8, once the magnet shifts toward the rotor outer surface, the operating point of the magnet moves below the knee point of the magnet in the second quadrant of the B-H loop. According to the FE results, with $h=17\ mm$, the magnets are almost fully magnetized in the no-load condition.

4.4 FE-based Design optimization

In this section, the optimizer and FE software presented in section 3.5 are used to perform the optimization procedure. The properties of the GA integrated in the FE software are explained in section 3.5.2

4.4.1 Optimization Objectives

According to the characterization of the existing VFM, the new machine should have less torque ripple, the similar average torque close to the existing one, and a better torque capability in the field-weakening operating condition. Moreover, the magnetization current and the no-load operating point of the magnet should be controlled. The objective for T_r is defined as $T_r\%$<7.5%, and the torque mean value objective is defined as 36 N.m<T_{mean}<38 N.m.

To make the control of the radially magnetized VFM easier, the VFM is assumed to operate with pure I_q before the base speed and the negative I_d component will be considered for operation above the base speed. As the current rotor topology provides a positive reluctance torque in the field-weakening region (L_q>L_d), the maximum torque of the machine is checked for the best cases of the optimization problems.

4.4.2 Optimization Parameters

To perform the optimization in the FE software, the CAD model of the machine is parameterized and the geometric parameters are used as the optimization parameters. Fig. 4-9 shows the defined optimization parameters in the FE model.

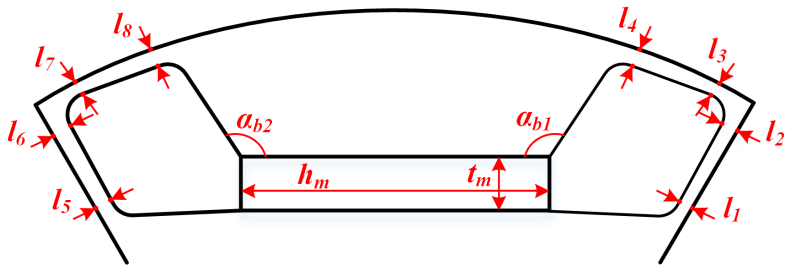

Fig. 4-9: Optimization parameters.

Except for magnet length and width, the other parameters are related to the barrier shapes. Defining five parameters for each barrier provides a great flexibility and a very wide range for the shape of the barriers.

α_{b1} and α_{b1} are defined as the angle between the magnet and the barriers which specify θ_p. The initial range for the mentioned angles is defined as $95^{\circ}<\alpha_{bi}<115^{\circ}$. Based on the FE simulations, for angles larger than 115°, the risk of the partial demagnetization of the magnets increases. Also, angles less than 95°, limit the flux linkage and increase I_{mag}.

l_1, l_2, l_5, l_6 are parameters that define the clearance between the two barriers in two adjacent rotor pole. The clearance between the two adjacent barriers is important as it can change the reluctance of the flux path for both *d* and *q* axes flux. Moreover, some part of magnetizing and demagnetizing flux pass through this area that will not be effective. Besides, the magnetic considerations, the mechanical considerations should be taken into account. As a result, the minimum and maximum values for these parameters are considered 0.5 mm and 1.5 mm, respectively. With l_3, l_4, l_7, l_8, the clearance between the barriers and the outer surface of the rotor is specified. According to the FE simulations, this clearance affects the $T_r\%$. Moreover, this area should be saturated to prevent any circulating flux in the rotor. This area also has an important role to enhance the design mechanically so it can be suitable for high-speed applications. According to the mentioned considerations, the minimum and maximum values for these parameters are 0.5 mm and 1.5 mm, respectively.

The magnet dimensions are also considered during the optimization procedure. The range of change for these parameters are defined based on the required I_{mag} and T_{mean} and also regarding the ML of the magnet at no-load condition. According to the FE simulation, with 24 mm$<h_m<$26 mm and 4 mm$<t_m<$5 mm, the design fulfills the expected I_{mag} and T_{mean}.

During the optimization procedure, the air gap length of the machine is kept constant as 0.5 mm that is a reasonable value for this size of machines.

4.4.3 Applying Genetic Algorithm

To perform the optimization, a group of initial cases is necessary to be defined. The number of initial cases depends on the number of optimization parameters. The initial cases of each optimization problem are defined using the best cases of the previous optimization problems. This means that the optimization procedure is done several times to prevent the selection of local minima. Moreover, different combinations of optimization parameters are selected to have

a more comprehensive optimization procedure. Fig. 4-10 shows the T_r% and T_{mean} for one optimization problem with 230 initial cases and 1000 of evaluated cases. The best cases in terms of T_r% and T_{mean} are considered as the initial cases for other optimization problems.

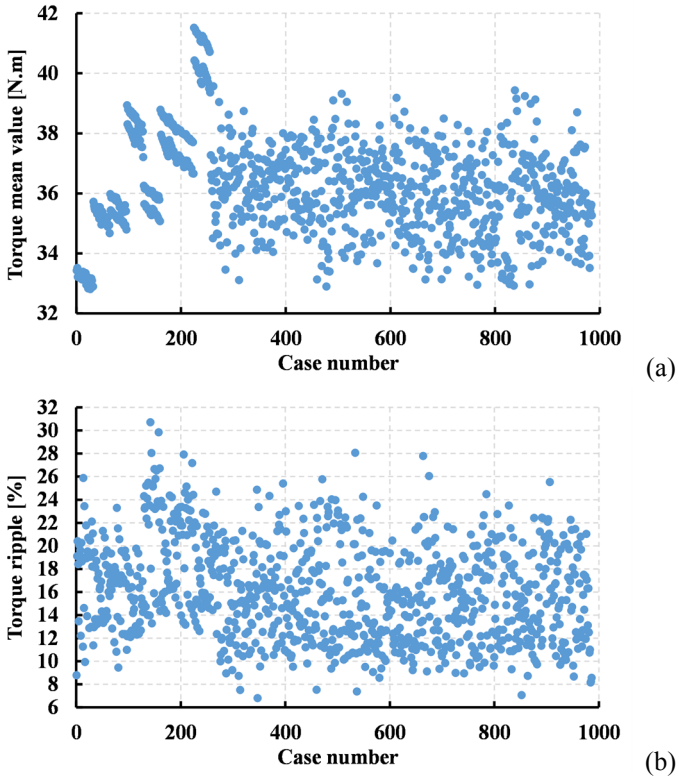

Fig. 4-10: T_r% and T_{mean} for an optimization problem (FE results).

4.4.4 Optimized Design Selection

87 best cases with T_r%<7% and 34 N.m<T_{mean}<38 N.m are selected to evaluate the maximum power, magnetization current, and maximum reluctance torque.

The proposed method to evaluate the torque-speed, and power-speed characteristics of PMSMs in section 4.2 requires simulating many cases, which is time-consuming. A rough method considering constant L_q to evaluate the maximum power of a design is proposed. As the proposed radially magnetized VFM is supplied with pure I_q for speeds less than the base speed, the voltage equations of (4-2) and (4-3) can be written as

$$V_d(I_d = 0) = -\omega L_q I_q \tag{4-9}$$

$$V_q(I_d = 0) = R_s I_q + \omega \lambda_m. \tag{4-10}$$

According to (4-9) and (4-10), $V_s(I_d=0)$ is

$$V_s(I_d=0)=\sqrt{(-\omega L_q I_q)^2+(R_s I_q+\omega\lambda_m)^2}. \tag{4-11}$$

Using (4-11), L_q can be calculated as

$$L_q=\frac{\sqrt{(V_s(I_d=0))^2-(R_s I_q+\omega\lambda_m)^2}}{\omega I_q}. \tag{4-12}$$

To evaluate the base speed of the VFM, V_s in (4-11) is replaced with V_m from (4-6), and ω is replaced with ω_{base} as

$$V_m=\sqrt{(-\omega_{base} L_q I_q)^2+(R_s I_q+\omega_{base}\lambda_m)^2} \tag{4-13}$$

Based on (4-13), and neglecting $R_s I_q$, ω_{base} is

$$\omega_{base}\simeq\frac{V_m}{\sqrt{(L_q I_q)^2+(\lambda_m)^2}}. \tag{4-14}$$

The estimated maximum power of the VFM can be estimated as

$$P_{\max}=T_{mean}\times\omega_{base} \tag{4-15}$$

where T_{mean} is the torque mean value from the FE simulation. Moreover, the produced reluctance torque of each design at a specific angle in the field-weakening region is estimated using FE results. Table 4-1 lists the best ten cases according to the design requirements. To select one of the proposed designs as the best design, the method proposed in section 4.2 is used to develop the torque-speed and power-speed characteristics of all ten selected designs.

Table 4-1. Specification of the best designs.

Case #	**1**	**2**	**3**	**4**	**5**	**6**	**7**	**8**	**9**	**10**
T_{mean} **[N.m]**	36.7	36	35.6	34.1	35.8	36.2	36.5	36.5	36.3	36.4
T_r**%**	5.5	6	5.6	5.3	6.1	5.8	5.8	5.6	5.8	5.3
ω_{base} **[rad/s]**	308.6	311.2	304.1	313.1	306.1	303.8	309.4	306.5	307.5	308.2
P_{max} **[Watt]**	3766.1	3733.7	3609.3	3563	3656	3667	3766	3732	3717	3735
T_{relm} **[N.m]**	21.8	22.7	24.6	21.8	23.5	24	22.1	23.1	24.35	23.1

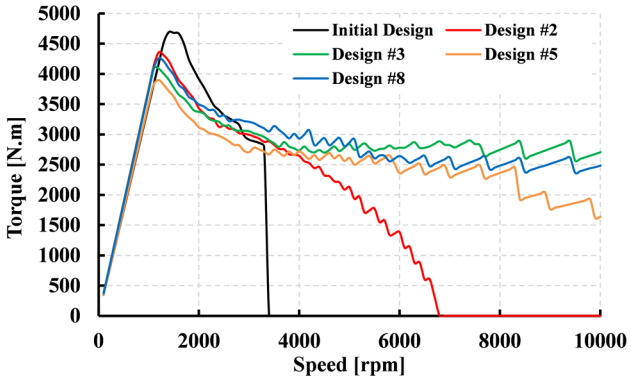

Fig. 4-11: Power-speed characterization of the best designs (proposed method).

Fig. 4-11 shows the power-speed characteristics of the selected cases and compares it with the initial design. According to Fig. 4-11, the radially magnetized designs have larger operating speed range in comparison with the initial design. Moreover, the initial design has a higher base speed and maximum power. As it can be seen, even between the optimized designs, the operating range is limited according to the design parameters [Designs # 2 and 5]. Based on the maximum power and the operating range, design #8 is selected as the best one.

4.5 Optimized Design, Results, and Discussion

Fig. 4-12 shows the rotor topology of the optimized design. According to this figure, the proposed radially magnetized VFM has a simple rotor topology. The red arrows in this figure show the magnetization direction of AlNiCo 9 magnets.

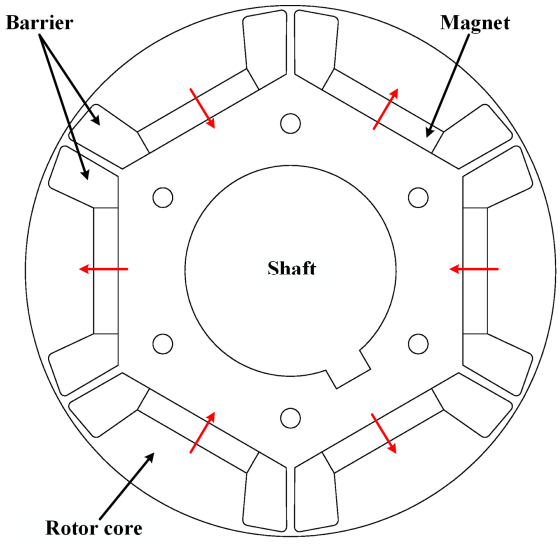

Fig. 4-12: Rotor topology of the optimized radially magnetized design.

Moreover, unlike the existing VFM where the rotor core is attached to the shaft using a non-magnetic hub, in the proposed design the rotor core is connected to the shaft using a key way. Besides, to fix the rotor laminations six holes are carved in the rotor core. These holes are on the *q*-axis of the rotor and do not affect the magnetic flux pattern in the rotor at different operating conditions. The magnet dimensions of the new and existing designs are 5 mm×25.75 mm×120 mm and 7 mm×14.1 mm×120 mm, respectively. These values show 31% increase in the magnet volume for the new design. The main reason for the magnet dimension increase in the new design is to prevent the partial demagnetization of the magnet due to the armature *q*-axis flux.

To check the operating point of the magnets, five probes are placed in the middle of the magnet in the FE model. Fig. 4-13 shows the magnetic flux lines in the proposed VFM and the magnetic flux density of the magnet at the no-load condition. Based on this figure, the radial pattern of the flux lines as a result of the magnet is clear.

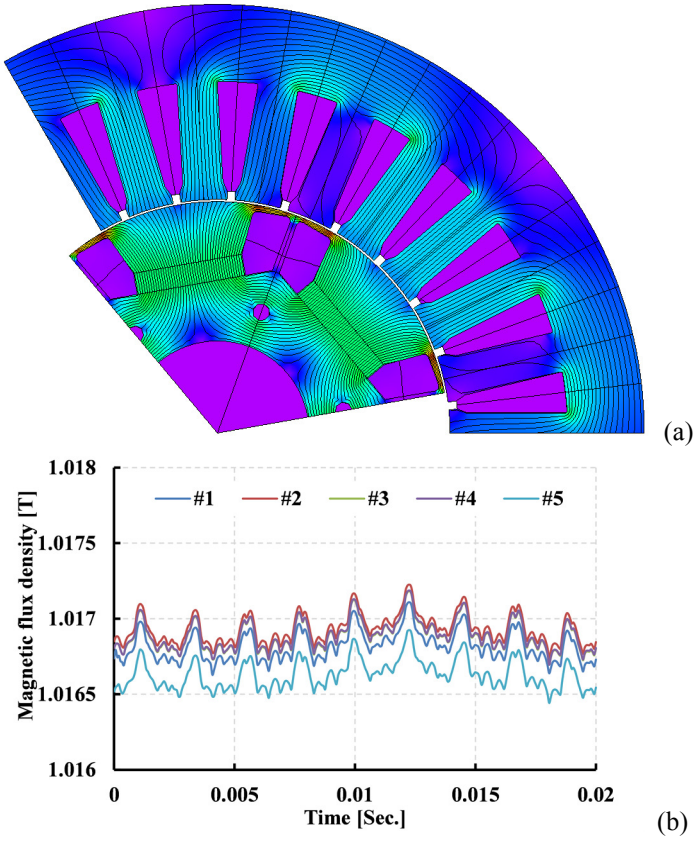

Fig. 4-13: Fully magnetized optimized radially magnetized VFM, (a) No-load magnetic flux line, (b) No-load magnetic flux density in the center of the magnet (FE results).

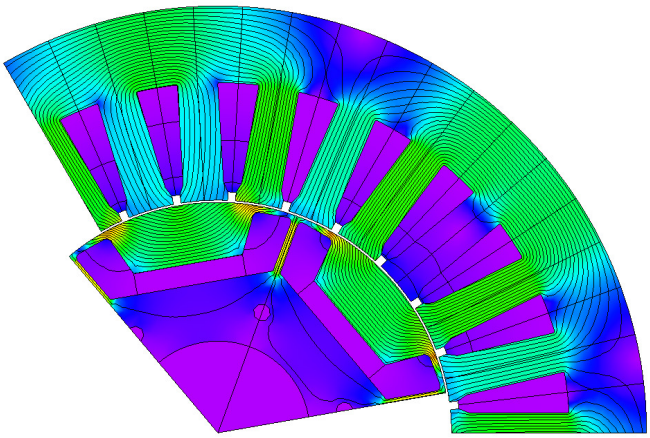

Fig. 4-14: Fully magnetized optimized radially magnetized VFM, *q*-axis flux lines (FE results).

Moreover, based on Fig. 4-13(a), the ML of the magnet is more than 99% at no-load. To check the impact of the *q*-axis flux of the armature, the magnet is replaced with air, and the machine is supplied with I_q=14.14 A. The resultant *q*-axis flux lines in the optimized radially magnetized VFM are shown in Fig. 4-14. Based on Fig. 4-14, the *q*-axis flux lines do not pass through the magnet that shows the precise design of magnet position and dimensions, as well as the barrier shapes. This prevents the demagnetization of the magnet in the loaded condition. Moreover, the *q*-axis flux lines pass through the upper area of the rotor core, and the area between the two adjacent barriers are saturated.

Fig. 4-15(a) shows the magnetic flux lines pattern when the proposed VFM at full-load condition (I_q=14.14 A). To check the impact of the armature current on the ML of the machine, the proposed VFM is supplied with I_q=14.14 A and then run for one cycle at the no-load condition. The magnetic flux density of the magnet is shown in Fig. 4-15(b). According to this figure, the machine keeps its ML after loading. Based on the FE results, the no-load flux linkage of the machine after removing I_q is 0.50 Wb that shows the ML of the VFM is 98%. This means that the demagnetizing effect of the *q*-axis flux is minimized as a result of the appropriate design of the proposed machine.

To check the demagnetization and magnetization procedures and also the required current, an operation strategy is defined in the FE simulation, as shown in Fig. 4-16. In this strategy, the proposed VFM is run at no-load condition for one cycle [period (1) in Fig. 4-16] to show that the machine is fully magnetized. Then the demagnetizing current pulse is applied to the machine [period (2) in Fig. 4-16].

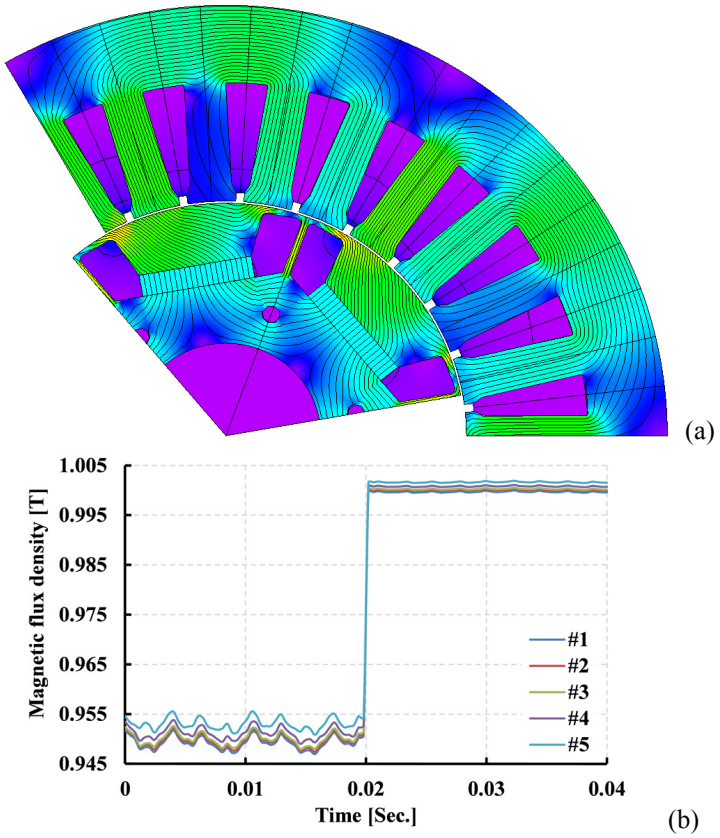

Fig. 4-15: Fully magnetized radially magnetized VFM, (a): full-load (I_q=14.14 A) magnetic flux lines pattern, (b): magnetic flux density in the center of the magnet during and after the full-load condition (FE results).

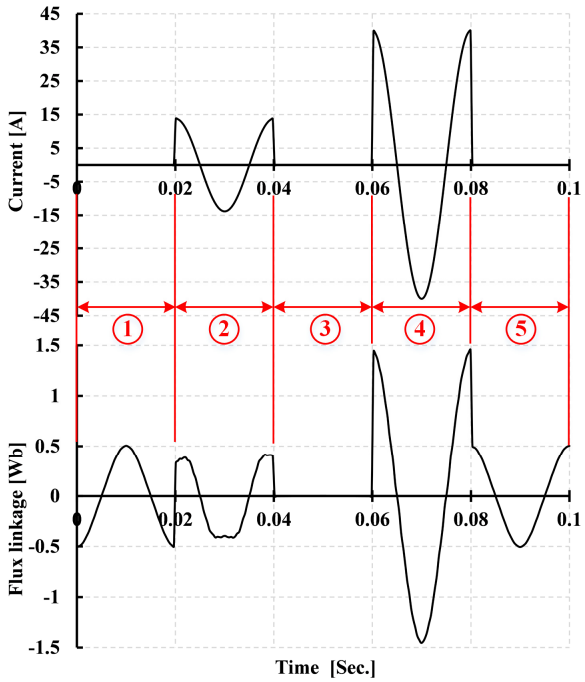

Fig. 4-16: Phase current and flux linkage for magnetization and demagnetization procedures (FE results).

The VFM is run again at no-load condition for one cycle [period (3) in Fig. 4-16] to check the effect of the demagnetizing pulse on the magnet operating point and consequently on the machine flux linkage. The magnetizing current pulse is then injected to the VFM [period (4) in Fig. 4-16] and the machine is run again at no-load condition for one cycle to check the ML of the magnet after the magnetizing pulse [(5) in Fig. 4-16]. In Fig. 4-16, the VFM is fully demagnetized in part (3) as a result of the demagnetization current of -13.8 A in part (2), and it is fully magnetized in part (5) as a result of the magnetization current of 40 A in part (4).

Fig. 4-17 compares the torque waveform of the optimized and initial designs. Based on Fig. 4-17, T_{mean} for initial and optimized designs are 36.7 N.m and 36.6 N.m, respectively. Moreover, the peak to peak value of torque for the initial and optimized designs are 7.2 N.m and 2.2 N.m, respectively.

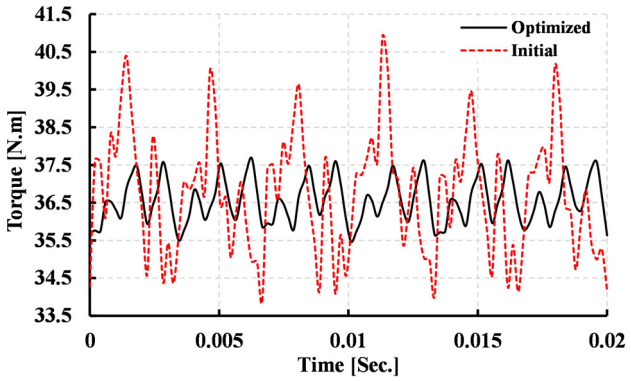

Fig. 4-17: Comparison of the torque waveform between the initial and optimized designs (FE results).

As a result, T_r% of initial and optimized designs are 19.6% and 6%, respectively. This shows 70% reduction in T_r% for the optimized design while T_{mean} is almost constant for both designs.

Fig. 4-18 compares the no-load back-EMF of the initial and optimized designs at a speed of 1000 rpm. According to Fig. 4-18, the optimized design has less no-load back-EMF in comparison with the initial case, as the RMS value of the no-load back-EMF for the initial and optimized designs are 124.5 V, and 109.9 V, respectively, which shows 11.8% reduction in the optimized design. According to the FE results, the peak value of the no-load linkage flux are 0.56 Wb and 0.51 Wb for the initial and optimized designs, which shows 9% reduction. Besides, Fig. 4-18 shows a higher 3rd harmonic content in the optimized design. Table 4-2 compares the harmonic content of the no-load back-EMF between the optimized and initial designs.

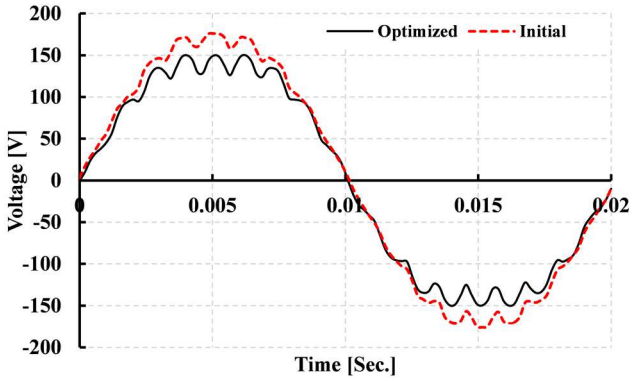

Fig. 4-18: Comparison of the no-load back-EMF between the initial and optimized designs (FE results).

Table 4-2. No-load back-EMF harmonics in [V] (FE results).

	1	3	5	7	9	11	13
Initial design	175.1	4.9	2.6	1.9	1	1.1	1.5
Optimized design	154.7	11.9	1.6	0.9	0.1	0.1	0.3

Based on the FE result, the 3rd harmonic of the no-load back-EMF is increased in the optimized design. In term of total harmonic distortion of the no-load back-EMF, this parameter is 7.4% for the initial case and 10.3% for the optimized design. For the initial case, the harmonic content of the no-load back-EMF is lower as a result of the uneven air gap length. For the optimized case, the air gap length is even and equal to 0.5 mm.

To have an overview regarding the saliency, Fig. 4-19 shows that torque-angle characteristics of the initial and optimized designs at ML of 100%.

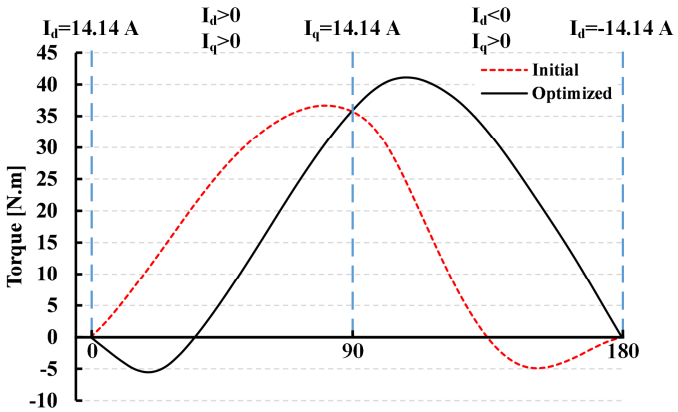

Fig. 4-19: Comparison of the torque-angle characteristics between the initial and optimized designs at 100% ML (FE results).

According to this figure, the inverted saliency of the initial design enhances the torque of the machine in the region where I_d >0. Both designs have the same torque mean value at I_q=14.14 A. In the region of I_d<0, T_{mean} of the initial design decreases while this parameter increases for the optimized design till the current angle of maximum torque is reached.

Fig. 4-20 compares the demagnetization characteristics of the initial and optimized design at a ML of 100%.

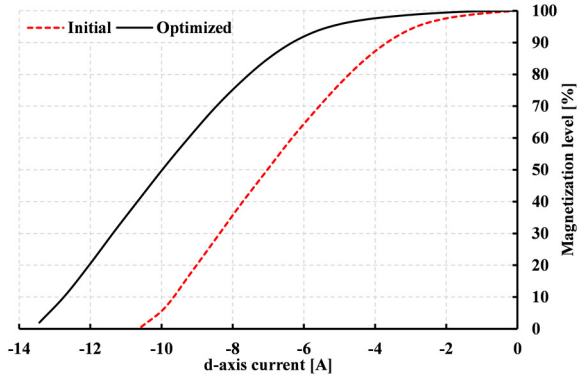

Fig. 4-20: Comparison of the demagnetization characteristics between the initial and optimized designs (FE results).

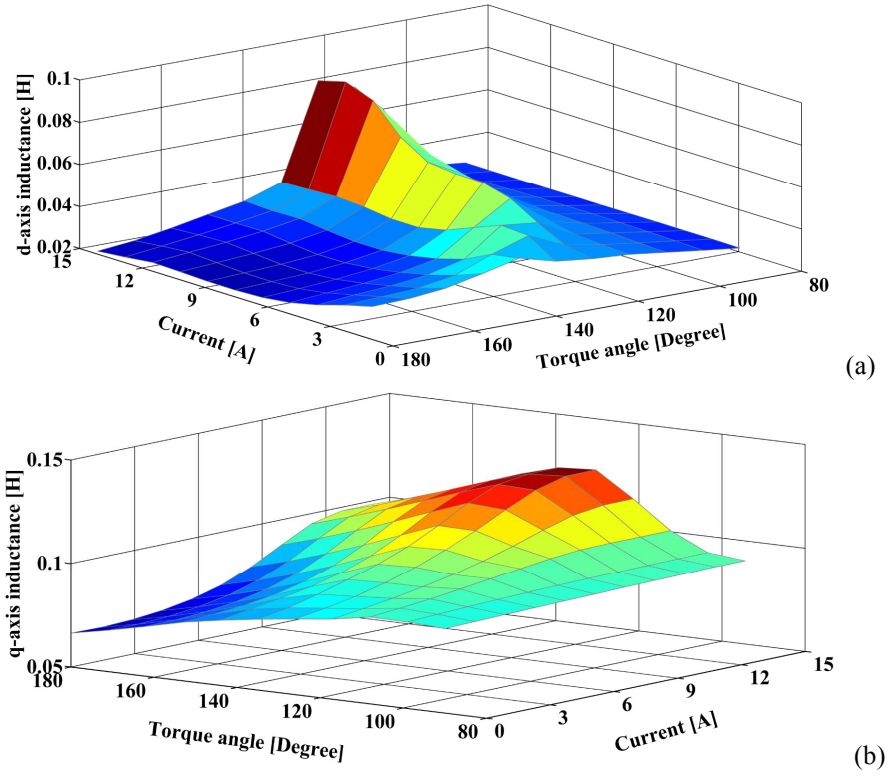

Fig. 4-21: Inductances as a function of current vector amplitude and angle for optimized radially magnetized VFM at fully magnetized condition, (a): *d*-axis inductance, (b): *q*-axis inductance, (FE results).

Based on Fig. 4-20, to reach a specific ML, the optimized design needs more current to be demagnetized. The demagnetization current to make the VFM fully demagnetized for the existing VFM is -10.6 A and for the optimized VFM is -13.8 A. According to Fig. 4-20, for a specified allowable demagnetization level in the field-weakening region, a higher negative *d*-axis current can be applied to the optimized case. This provides a higher power capability for the optimized case at higher speeds.

Fig. 4-21 shows L_d and L_q of the optimized radially magnetized VFM in fully magnetized condition. According to Fig. 4-21, both L_d and L_q vary with the current vector and for most of the operating range, $L_q > L_d$. In the optimized radially magnetized VFM, L_d varies between 21.5 mH to 86.5 mH and L_q changes between 66 mH to 128.5 mH in the proposed range of the current vector.

Fig. 4-22 shows the effects of the current vector on the magnet flux (λ_m) of the optimized radially magnetized VFM.

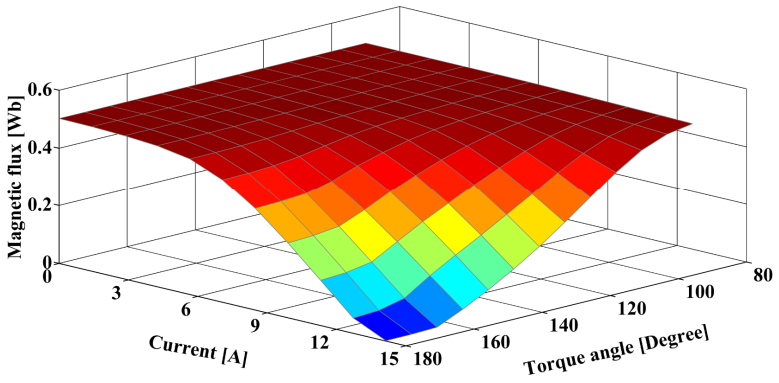

Fig. 4-22: Magnet flux as a function of current vector amplitude and angle for optimized radially magnetized VFM at fully magnetized condition, (FE results).

According to Fig. 4-22, the demagnetizing effect of the armature current in the field-weakening region is clear. Moreover, a comparison between Fig. 4-2 and Fig. 4-22 shows that this demagnetizing effect is reduced for the optimized radially magnetized design, which justify the results of Fig. 4-20.

Fig. 4-23 compares the torque-speed characteristics of the initial and optimized VFMs at different MLs using the proposed method in section 4.2. According to Fig. 4-23, and based on the drive system limits, it is clear that the fully magnetized optimized radially magnetized VFM can operate at a wider range of speed. As the optimized design has a higher torque capability as a result of the positive reluctance torque in the field-weakening operation, it can produce

more torque at the lower MLs. Besides, as the stator topology is fixed, the rotor topology modifications in the optimized design results in a lower base speed in comparison with the initial case.

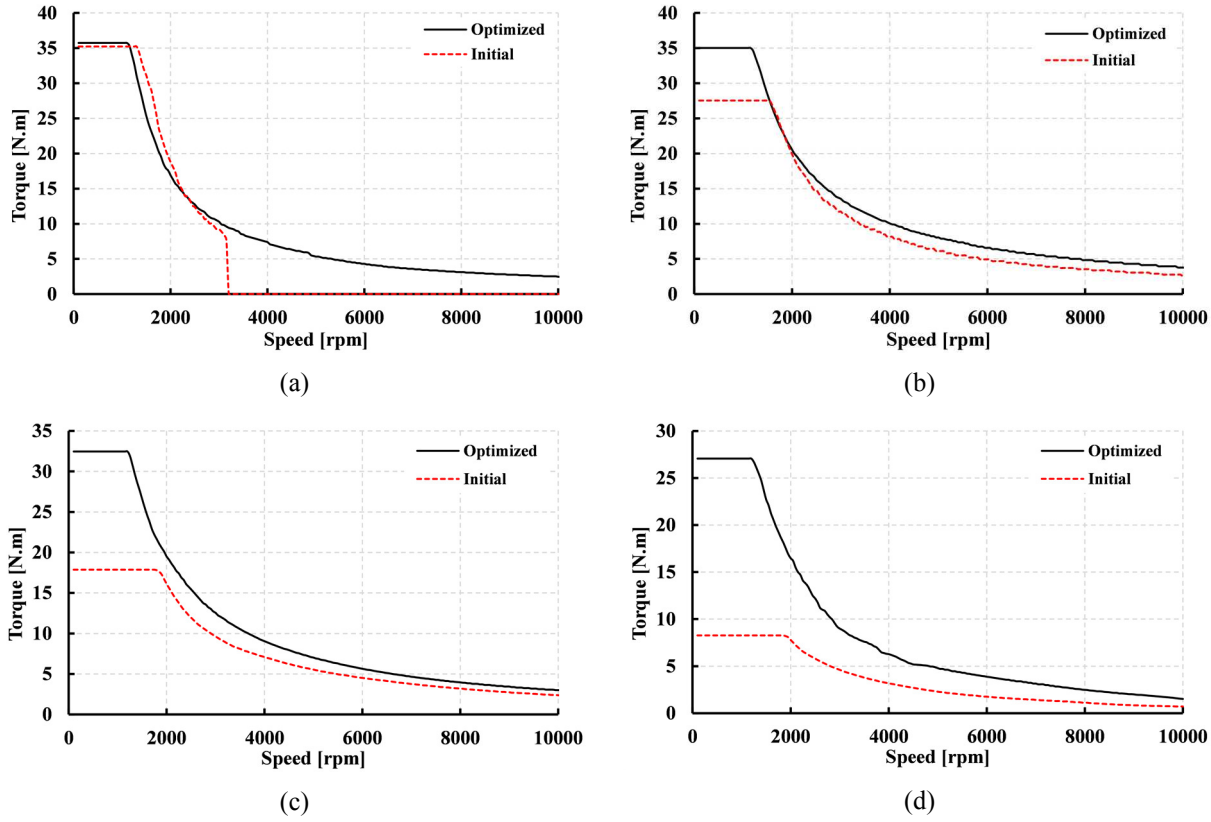

Fig. 4-23: Comparison of the torque-speed characteristics between the initial and optimized designs at ML of (a) 100%, (b): 75%, (c): 50%, and (d): 25% (proposed method).

Fig. 4-24 shows the power-speed characteristics of both initial and optimized designs. According to Fig. 4-24, the optimized design provides higher power for the high-speed region. Moreover, at lower MLs, the optimized design has a higher power in comparison with the initial design. At a ML of 75%, the power-speed characteristic is almost constant for the optimized design in the high-speed region. Fig. 4-23 also shows that having a positive reluctance torque in the field-weakening region helps to have a constant power at the high-speed region. The maximum developed power (at ML of 100%) of the initial machine is higher than the optimized design as the base speed of the initial case is larger than the optimized design.

Fig. 4-25 shows the efficiency map of optimized radially magnetized VFM at different MLs developed using the FE software for efficiencies higher than 85%. According to this figure, at a ML of 100%, the proposed VFM provides high efficiency at the low-speed region and low

efficiency at the high-speed region.

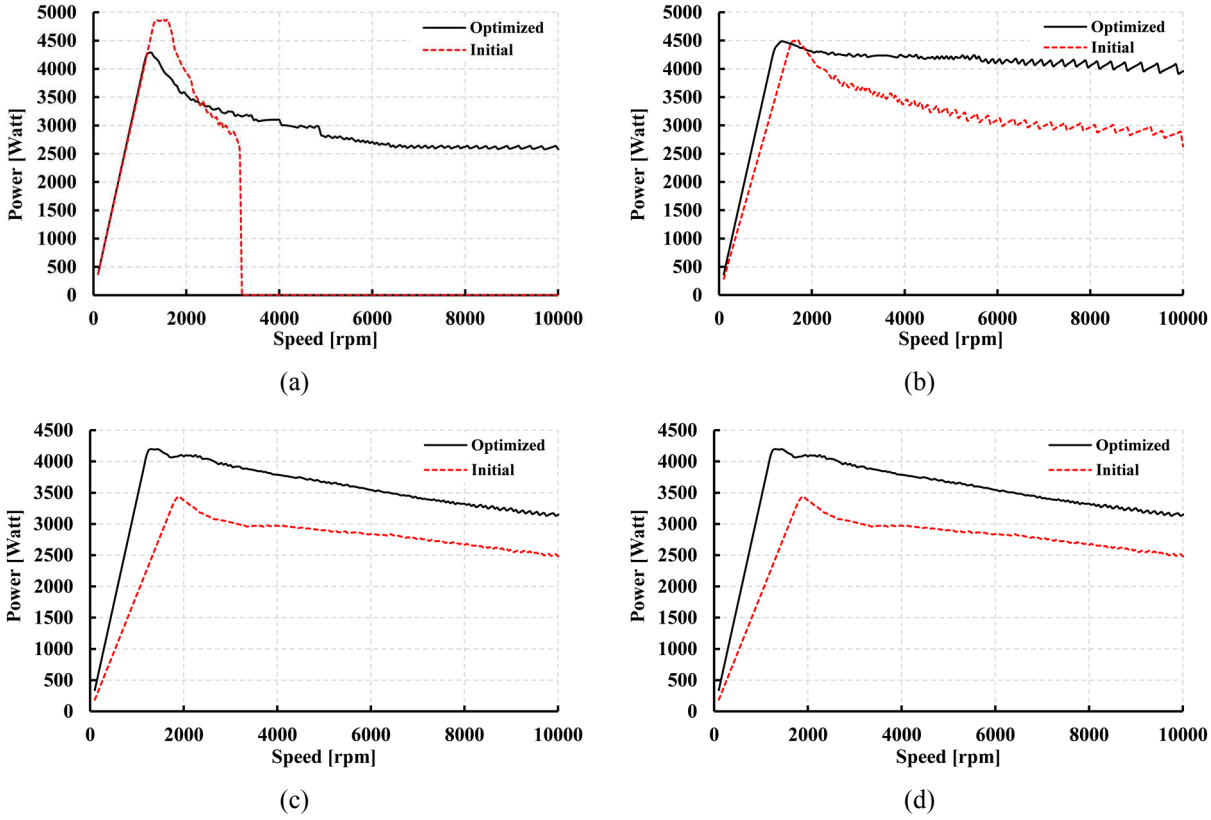

Fig. 4-24: Comparison of the power-speed characteristics between the initial and optimized designs at ML of (a): 100%, (b): 75%, (c): 50%, and (d): 25% (proposed method).

As the ML is reduced to 75%, the efficiency of the high-torque and low-speed region reduces and the efficiency of the machine at the high-speed region increases. Based on Fig. 4-25, with the ML reduction, the dark area (maximum efficiency) at the center of the efficiency map is enlarged toward the high-speed region. According to these results, lower MLs, provides a better efficiency at the high-speed region. On the other hand, the higher ML provides a better efficiency at low speed, high-torque region.

Table 4-3 shows the operating range of the proposed VFM at different MLs, and efficiency ranges. With an appropriate control strategy, and working at different MLs, the maximum available efficiency can be achieved at each operating point by varying the ML.

Fig. 4-26(a) shows the efficiency map of the optimized case considering the maximum achievable efficiencies at different MLs. Fig. 4-26(b) shows the MLs at which the maximum efficiency of the VFM is achieved. Based on Fig. 4-26(a), the optimized design has a high efficiency for a wide range of torque and speed that is provided by the variable magnet flux.

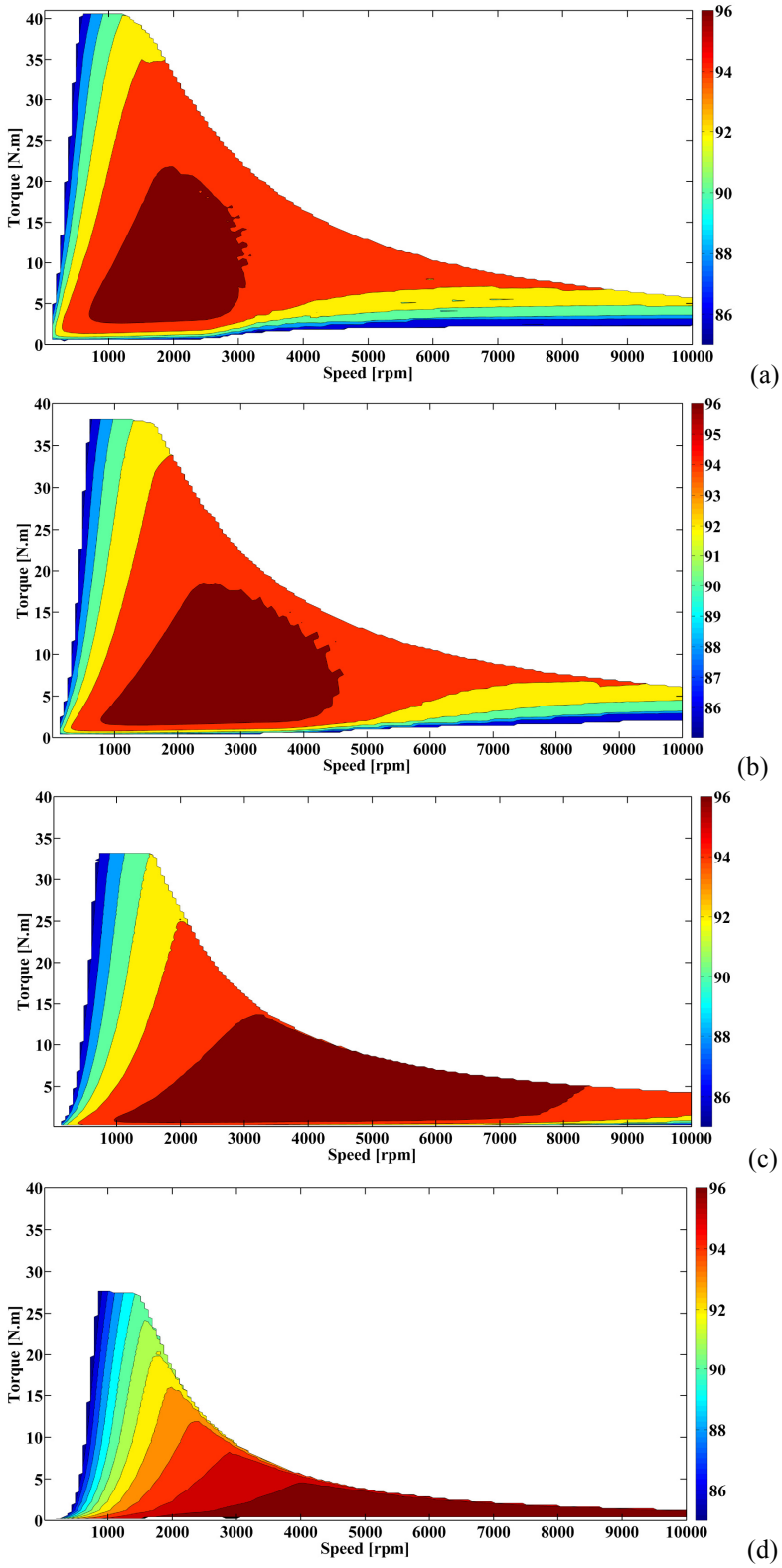

Fig. 4-25: Efficiency map of radialy magnetized VFM (a): 100%, (b): 75%, (c): 50%, and (d): 25% (FE results).

Table 4-3. Operating range (%) for different ranges of efficiency at different MLs (FE results).

ML%	>90%	>80%	>70%	>60%	>50%
100%	75.6	88.8	92.1	93.2	94.1
75%	77.2	89.1	91.9	92.9	93.9
50%	76.8	87.8	90.9	92.4	93.6
25%	62.9	81.3	86.6	89.7	90.6

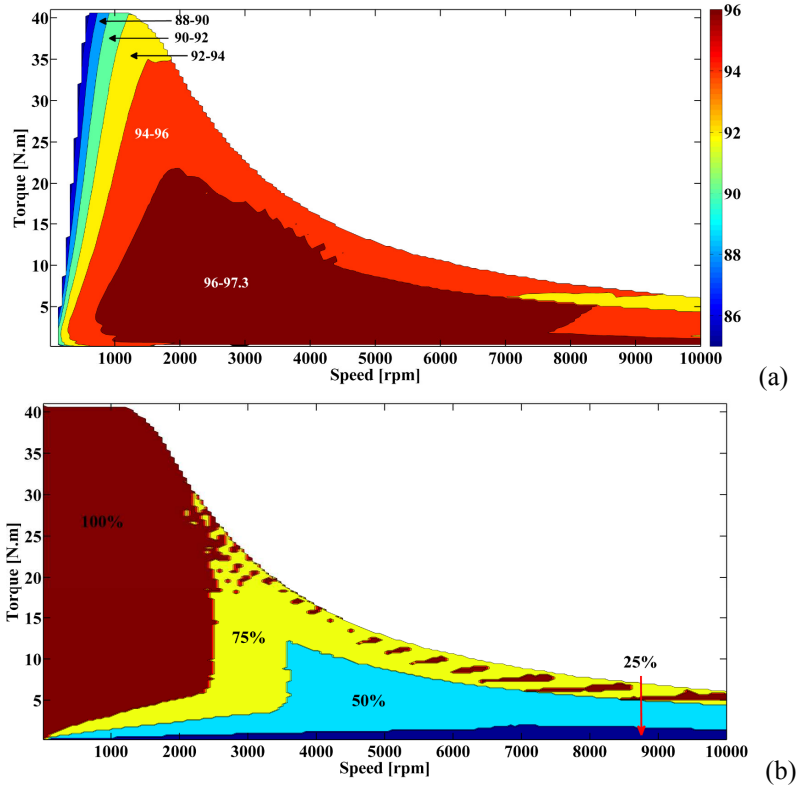

Fig. 4-26: (a): Efficiency map of the optimized VFM considering maximum efficiencies, (b): MLs to achieve maximum efficiency (FE results).

The maximum efficiency in this machine is 97.3% and for more than 90% of the operating range shown in Fig. 4-26(a), the efficiency is more than 94%. Based on Fig. 4-26(b), the maximum efficiency of the optimized VFM in the high-speed region is achieved at lower MLs.

4.6 Conclusion

A radially magnetized design of VFM with AlNiCo magnet with an enhanced power and torque capabilities in the high-speed region was proposed in this chapter. An analytical method using the FE results of L_d, L_q and flux linkage, as well as the *dq* model of PMSMs, was provided to develop the torque-speed and power-speed characteristics of the VFM considering the

AlNiCo magnet demagnetization. Application of the proposed method for the existing spoke-type VFM with inverted saliency (L_d>L_q) revealed that the power and torque drop in the field-weakening region is mainly due to the negative reluctance torque and the AlNiCo magnet demagnetization. A design procedure of the radially magnetized VFM was presented and the impact of magnet dimensions, position selection, and barrier shape on the machine performance, were discussed. A FE-based design optimization strategy to minimize the torque ripple of the machine and guarantee the high torque capability of the machine was proposed. The optimized radially magnetized design was compared with the existing VFM, and the results show 70% reduction in torque ripple and an improved power capability for a wider range of the speed.

Chapter 5. Characterization of the Variable Flux Machine at different Magnetization Levels

5.1 Introduction

Since the AlNiCo-based VFM is designed to operate with reduced magnet flux beyond the base speed, it is important to identify the features of VFM at this operating condition. The required energy for magnetization and demagnetization, torque, as well as the core loss, at different MLs are important parameters for the characterization and industrial applications of the VFM.

An analytical method is developed to calculate the required energy for the magnetization and demagnetization of AlNiCo magnets in the existing spoke type VFM. The FE model of a VFM is used to record the magnet operating point variations during the magnetization or demagnetization procedure and an advanced method is proposed to estimate the required magnetic energy to change the magnet operating point. A test procedure is also developed to measure the required magnetization and demagnetization energy using the applied current and voltage pulses. Moreover, the effect of the pulse duration on the required energy is studied.

In addition, the torque performance of the VFM at different MLs is analyzed in this chapter. The test results are compared with the FE results to evaluate the effect of ML variations on the torque characteristics. Since the harmonic content of the no-load back-EMF and the no-load air gap flux density affect the torque characteristics, the verified FE model of the VFM is used to show how the ML variations affect the harmonic content of the no-load back-EMF and air gap flux density.

A model for achieving improved prediction of core losses in electrical machines is also proposed in this chapter. The model is based on the calculation of an equivalent sinusoidal magnetic flux density for a non-sinusoidal magnetic flux density. In addition, an experimental method based on the flux controllability of the VFM is developed to measure the mechanical and the core losses at the no-load condition. These results are then used to verify the proposed core loss model coupled into the FE model of the VFM.

This chapter is organized as follow: Section 5.2 proposes an advanced method to calculate the magnetization and demagnetization energy at different MLs. An experimental procedure is

developed to measure the magnetization, and demagnetization energy and verify the analytical method. Section 5.3 shows the torque characteristics of the spoke type VFM at different MLs. Section 5.4 demonstrates the proposed model for VFM core loss calculation. This model is then implemented in the FE software, and an experimental model is developed to verify the proposed model.

5.2 Magnetization and Demagnetization Energy

While VFM has the potential to be used in the industrial, and traction applications, the magnetization and demagnetization procedures, as well as the machine features at different MLs, should be studied in depth. Moreover, in a specific working strategy, this machine may be subjected to consequent magnetizations and demagnetizations based on the required torque and speed. In this situation, the properties of the magnetization and demagnetization current pulses besides their energy are important, specifically for applications where the machine is supplied from a battery, and the driving range is important.

5.2.1 Test Procedure to Measure Magnetization and Demagnetization Energy

A test is developed to measure the required energy to magnetize the VFM fully or demagnetize the magnet to a specific ML. The VFM is supplied with one magnetizing or demagnetizing *d*-axis current pulse while the rotor speed is set to zero. The current pulse magnitude and duration can be controlled using the current controller drive system. The friction and windage losses are speed dependent and once the speed is zero, these two components of the mechanical loss are zero. During the test procedure, the VFM is supplied with I_d and as a result, the rotor moves to the closest *d*-axis. In this case, the rotor moves a couple of degrees that implies the overall speed of zero and as a result, the zero friction and windage losses.

Since the VFM phases are supplied with a constant DC current, the rate of change of the magnetic flux in different parts is negligible and the core losses are negligible in comparison with the Ohmic losses. Voltages, and currents of the three phases are recorded during each test. The supplied energy is calculated based on the power of pulses for all phases and the pulse duration. The Ohmic power loss is estimated based on the stator phase resistance of 1.3 Ω and the measured phase current pulses. The total Ohmic energy loss is calculated using the Ohmic power loss pulses for all phases and the pulse duration. The total Ohmic energy is subtracted from the input energy and the resultant energy is the energy that provides the required magnetic

energy for the magnetization or demagnetization.

5.2.2 Advanced Method to Estimate Magnetic Energy using FE Results

To change the operating point of a magnet from one point to another, a specific amount of magnetic energy should be provided. This magnetic energy for a VFM is provided using a short-time *d*-axis current pulse. Fig. 5-1 shows the B-H loop of the AlNiCo magnet that describes the flux controllability of the AlNiCo-based VFM.

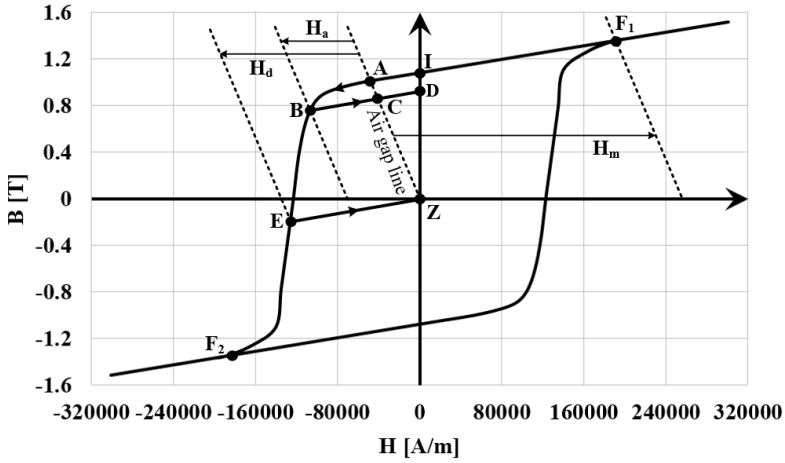

Fig. 5-1: B-H loop of AlNiCo 9 and the flux controllability in the VFM.

The operating point of the magnet for the fully magnetized VFM is point A as shown in Fig. 5-1. If the operating point of the magnet shifts to point B, the VFM is demagnetized to ML of D/I as expressed in Fig. 5-1. The magnetic energy that is required to demagnetize the fully magnetized magnet a the ML of D/I is the required energy to shift the operating point of the magnet from point A to point B. This magnetic energy (W_m) is proportional to the area between the B-H curve of AlNiCo 9 magnet and the vertical axis (B axis) between the two mentioned operating points as [72]

$$W_m = \int_V [\int_{B_A}^{B_B} H.dB]dv \tag{5-1}$$

where B_A and B_B are the magnetic flux densities at points A and B and V is the volume of the magnet.

In the FE software, a probe can be defined to record the radial and centrifugal components, as well as the absolute value of the magnetic flux density and field intensity in different parts of the model. To estimate the magnet operating point as explained in section 3.2.2.2, eight

probes are placed along the magnet in the FE model, to record B and H during the demagnetization procedure (Fig. 3-2). The mean values of both the magnetic flux density and field intensity for each probe are calculated over an excitation cycle. These mean values are averaged for the eight probes to have the average magnetic flux density and field intensity in the magnet which is considered as the operating point of the magnet in each working condition.

According to the operating point of the magnet at the no-load condition, and also the new operating point, the required magnetic energy to reach the new condition is calculated using (5-1). The integral of equation (5-1) is solved using the discrete integral function. In this integration, H is considered a function of B. To have accurate results of the discrete integration, the Spline method is used to fit a curve for the B-H loop of AlNiCo 9 in the 2nd quadrant and create more B and H values. Fig. 5-2 shows the overall flowchart of the proposed method.

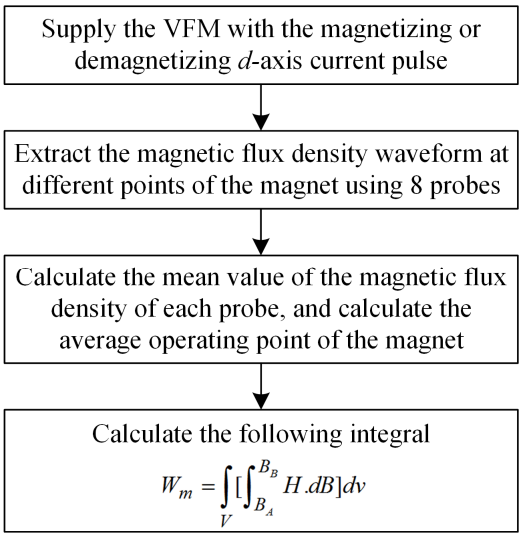

Fig. 5-2: The overall flowchart of the proposed method.

As the average operating point of the magnet is calculated based on the recorded magnetic flux densities, the integral over volume can be done by multiply $\int_{B_A}^{B_B} H.dB$ by the total volume of the magnet which is 7×14.2×120 mm^3 for the existing VFM. Moreover, since the VFM is a 6-pole machine, the number of the magnets should also be considered in the energy calculation.

5.2.3 Results and Discussions

In this section, the test results for the magnetization and demagnetization energy are compared with the estimated results using the proposed model. Moreover, the test and FE

results of the torque waveform at different MLs are compared. The effect of ML variation on the harmonic content of the no-load back-EMF and the no-load air gap flux density of the VFM is also presented.

Demagnetizing *d*-axis current pulses with different magnitudes are applied to the VFM and the ML is estimated after each test. For this, two sets of tests are performed: one with 15 ms pulses, a smaller DC bus voltage, and a higher current rise time, and the other with 10 ms pulses, a higher DC bus voltage, and a smaller current rise time. Although with the same demagnetization current magnitude, both cases lead to the same ML in the machine, with the 15 ms pulse consuming more energy that is not necessary. This means that with enough voltage, 10 ms is an appropriate pulse duration.

Fig. 5-3 shows I_d, the voltage and current pulses, and the resultant power in phase b, while the demagnetization current is set to -7 A with a duration of 10 ms. After 10 ms, the supply is removed and the current drops immediately, then the reverse voltages appear at the machine terminals. It is clear from Fig. 5-3 that the I_d current pulse follows the reference value with 10 ms duration and -7 A as the amplitude. According to Fig. 5-3, once the rotor moves to the *d*-axes, the phase current (phase b in this figure) has the same pattern as the I_d pulse and its value can be estimated using Park transformation with a constant angle. The phase voltage increases during the current transient and after that, it drops. To estimate the supplied energy to the VFM during the demagnetization procedure, the power pulse of the three phases for the duration of 10 ms is used.

According to Fig. 5-3(c), a significant part of the energy is injected during the transient of the current pulse. For this case, 55% of the 3-phase pulse energy is injected to the machine during the transient of the pulse. To minimize the energy consumption during the magnetization or demagnetization procedure, the available DC bus voltage magnitude and pulse duration should be selected to reduce the transient of the current pulse. In the FE simulation, the same procedure is simulated and the required energy to reach the specified ML is estimated.

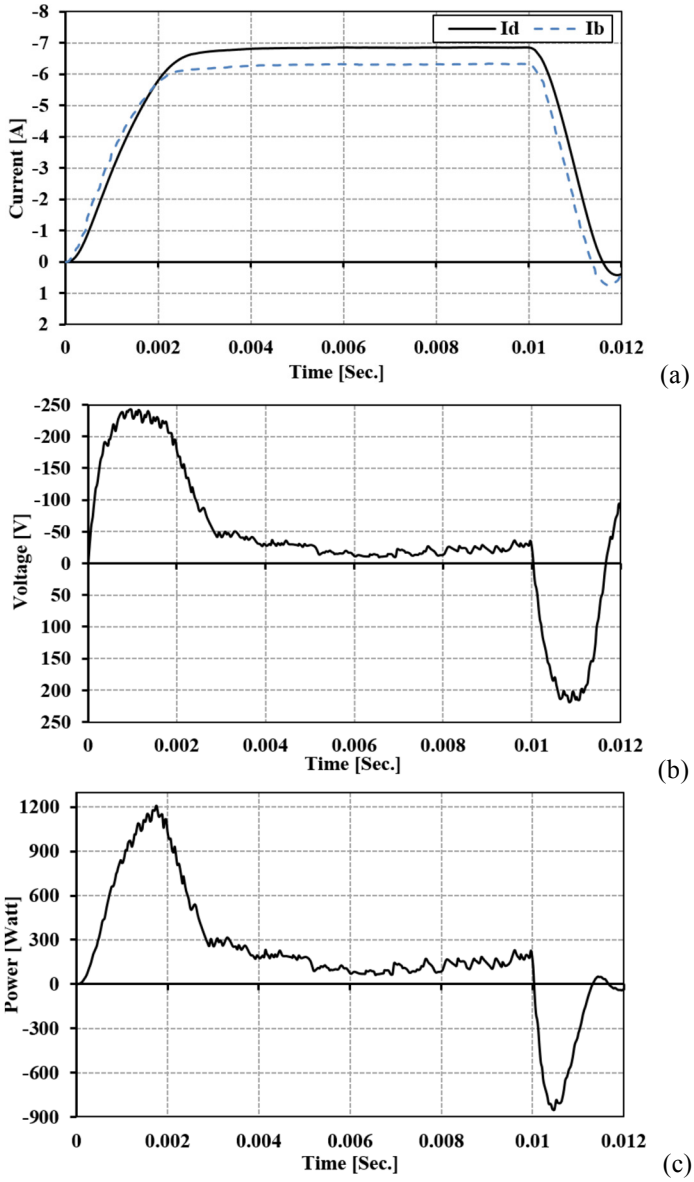

Fig. 5-3: (a) Demagnetizing *d*-axis current pulse and the current pulse of phase b, (b) the voltage pulse of phase b, and (c) the resultant power pulse of phase b.

Table 5-1 compares the required demagnetization energy from the test and the proposed model. Table 5-1 shows the applied demagnetization current magnitude, the achieved MLs and resultant Ohmic energy loss during the tests. With -11 A *d*-axis current pulse, the VFM is almost fully demagnetized. Based on Table 5-1, and the short period of the demagnetization current, the Ohmic energy loss due to field-weakening in VFMs is negligible compared to the permanent Ohmic loss of rare-earth PMSMs in the high-speed region. This guarantees the advantage of the AlNiCo-based VFMs against the conventional rare-earth PMSMs.

Table 5-1. Required magnetic energy for demagnetization.

Demagnetization current [A]	ML [%]	Loss energy [J]	Magnetic energy [J]		
			Exp.	Sim.	Err. %
4	86.6	0.55	1.16	1.21	-4.30
5	76.9	0.80	2.22	2.13	4.05
6	67	1.14	3.21	3.11	3.12
7	51	1.47	5.32	4.97	6.58
8	36	1.89	6.65	6.27	5.71
9	21	2.32	7.68	7.14	7.03
10	10.5	2.71	9.25	8.75	5.41
11	1.3	3.16	10.39	9.62	7.41

Additionally, Table 5-1 shows the required demagnetization and the required energy for the demagnetization of the VFM from tests compared to the analytical model. The comparison between the test and simulation shows the agreement. For all MLs, the difference between simulation and experimental results is less than 8%. The waste energy during the test can be reduced using a smaller demagnetization period. To magnetize the VFM magnets fully, a magnetization *d*-axis current pulse of 40 A with a duration of 10 ms is applied to the machine.

Fig. 5-4 shows the magnetization I_d pulse, the voltage and current pulses, and the resultant power in phase b. In this case, the VFM is supplied with a *d*-axis magnetizing pulse for 10 ms and after that, the supply is removed and the current drops immediately and the reverse voltage is induced in the VFM terminals. To calculate the required magnetization energy, the supplied energy to the machine within 10 ms and the Ohmic loss energy of all phases are used. According to Fig. 5-4, the duration and amplitude of the I_d current pulse show agreement with the desired values. According to the test results, the three-phase input energy is 65.17 J and the three-phase Ohmic energy loss is 21.60 J. As a result, the required magnetic energy for the magnetization procedure is 43.57 J.

Based on the FE model of the VFM and using (5-1), the required magnetic energy to shift the operating magnet from point Z in Fig. 5-1 to either point F_1 or F_2, is 41.66 J. Based on these results, 52% of the pulse energy is consumed during the transient of the pulses. During the transient of the current pulse, the voltage is maximum and the current is increasing.

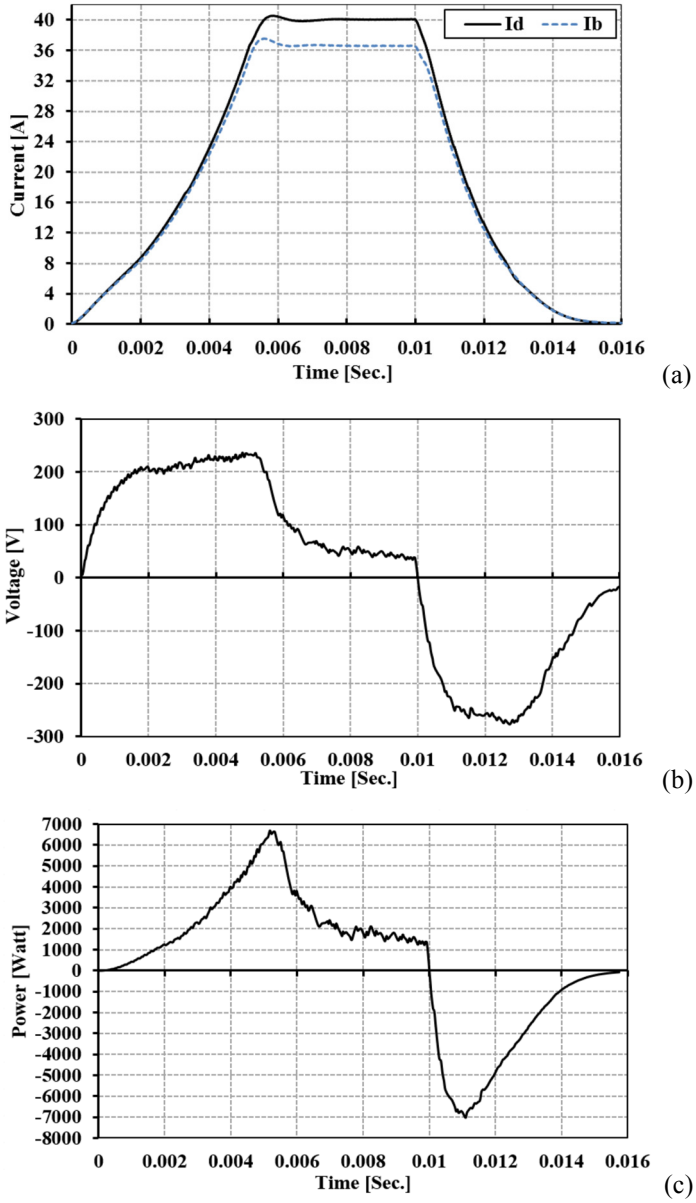

Fig. 5-4: (a) Magnetizing *d*-axis current and the current pulse of phase b, (b) the voltage pulse of phase b, and (c) the resultant power pulse of phase b.

The provided results in chapter show that the majority of the pulse energy is consumed during the transient of the current pulse. This shows the importance of the magnetization pulse duration selection and also minimizing the transient of the current pulse to have an efficient magnetization/demagnetization procedure.

5.3 Torque Waveform and Torque-angle at Different Magnetization Levels

This section investigates the effect of the ML of the magnet on the torque performance of the

VFM. Fig. 5-5 shows the test and FE results for the torque waveform of the VFM at three different MLs. The test and FE results show an agreement. Based on this figure, unlike the mean value of the torque, the peak to peak value and the ripple pattern of the torque waveform does not change dramatically with the change of the level of magnetization.

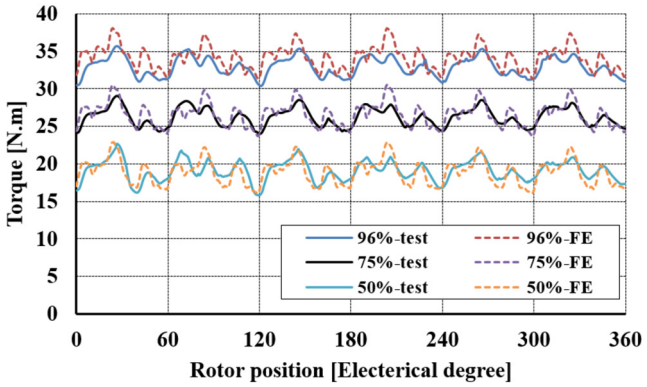

Fig. 5-5: Test and FE model results for torque waveform at different levels of magnetization.

Table 5-2 compares the test and FE results in more depth which shows a linear relationship between the torque mean value and the ML of the magnet.

Table 5-2. Torque characteristics at different MLs.

ML (%)	Mean value (N.m)		Peak to peak (N.m)		Ripple (%)	
	Test	FE	Test	FE	Test	FE
96%	33.00	34.17	5.29	6.68	16.03	19.53
75%	26.23	26.57	5.11	6.9	19.48	25.99
50%	19.19	18.87	5.88	7.2	30.64	38.16

Furthermore, the peak to peak value of the torque is almost constant with the ML variations. The torque ripple percentage increases with the ML decrease. According to the low variation of the peak to peak value of the torque, the torque mean value reduction is the main reason for the torque ripple increase. Besides the difference in the flux linkage values between the test and FE analysis, the accuracy of the measurement equipment, especially the torque transducer can cause the deviation between the measured values and the FE simulation results.

In the no-load condition, the back-EMF and the air gap flux density of PMSMs can project the effect of the magnet flux density on the electromagnetic torque production.

Fig. 5-6 shows the no-load phase back-EMF for different Mls at 1000 rpm from the FE

simulation. According to Fig. 5-6, the back-EMF reduction as a result of the reduction in the ML of the magnet is clear. The RMS values for the no-load phase back-EMF at different levels of the magnetization are 124.5 V, 90.83 V, 56.80 V, and 23.34 V, respectively.

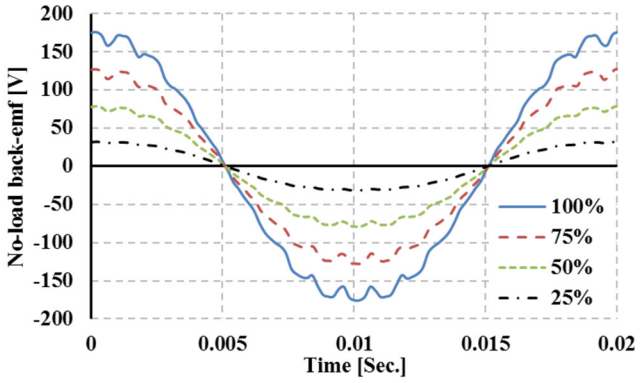

Fig. 5-6: Phase back-EMF at different levels of magnetization at 1000 rpm (FE results).

Table 5-3. Harmonic content of no-load phase back-EMF in [V] at different MLs.

ML (%)	1st	3rd (%)	5th (%)	7th (%)	THD %
100%	173.11	3.92 (2.26)	1.53 (0.88)	0.88 (0.51)	4.63
96%	164.45	3.86 (2.35)	1.4 (0.85)	0.84 (0.51)	4.66
75%	128.44	3.59 (2.80)	0.98 (0.76)	0.64 (0.50)	4.80
50%	80.32	2.97 (3.70)	0.42 (0.52)	0.35 (0.44)	5.00
25%	32.99	1.83 (5.55)	0.01 (0.04)	0.09 (0.27)	5.88

Table 5-3 shows the harmonic content of the no-load back-EMF at different MLs. Based on Table 5-3, it is clear that all harmonic components of the no-load back-EMF reduce with a reduction of the ML. The total harmonic distortion (THD) of the no-load back-EMF does not change dramatically with the ML reduction. The almost fixed THD of the no-load back-EMF can justify the constant peak to peak value of the torque with the ML changes.

In the VFM, the flux variation of the magnet affects the air gap flux. To obtain an overall picture of the flux density in the air gap, two particular points in the air gap with a significant difference in reluctance are selected for magnetic flux density calculation. One point is in the middle of one stator tooth and the other is in the middle of one stator slot.

Fig. 5-7 shows the harmonic content of the radial component of the no-load air gap magnetic flux density at the center of the stator tooth and slot.

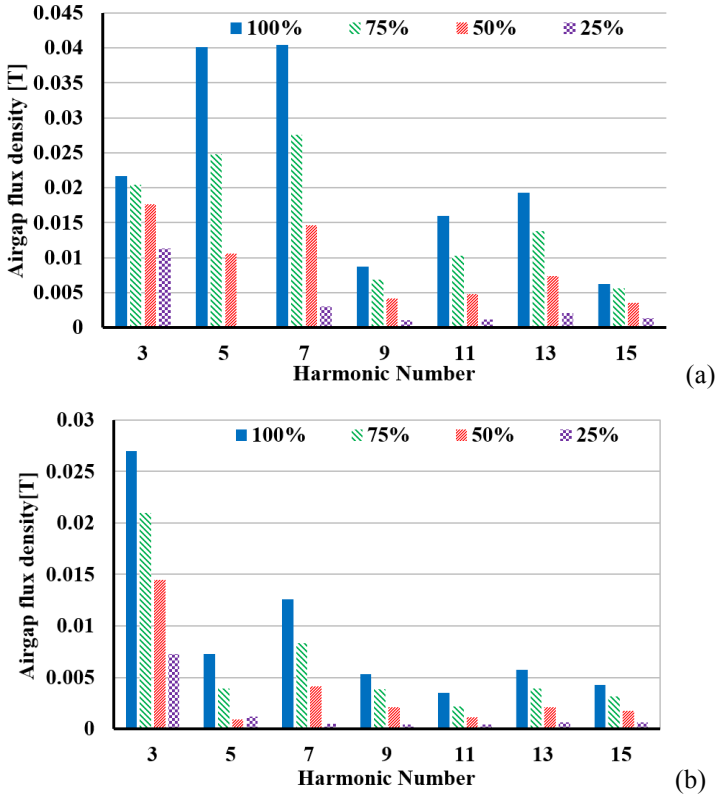

Fig. 5-7: Harmonic content of the no-load air gap flux density at the center of (a): the stator tooth, (b): the stator slot (FE simulation).

Based on Fig. 5-7, odd harmonics are dominant. For the point at the center of stator tooth, the 5th and 7th harmonics are the dominant harmonics and for the point at the center of stator slot, the 3rd harmonic is the dominant one. According to Fig. 5-7, the harmonics are reduced when the level of magnet magnetization decrease. For the point at the center of the stator tooth, the fundamental components of the no-load air gap flux density are 0.71 T, 0.52 T, 0.33 T and 0.13 T for the MLs of 100%, 75%, 50% and 25%. This reduction in the fundamental component of the no-load air gap magnetic flux density can justify the reduction of the torque mean value as a result of the magnet flux density reduction. The THD of the no-load air gap flux density at the center of the stator tooth is 9.58%, 9.11%, 8.5% and 9%, respectively for the mentioned MLs. These results show that the harmonic content of the no-load air gap flux density is almost constant with the change of the magnet ML and the main component of air gap flux density has the main role in the torque mean value reduction and as a result, the torque ripple percentage increases with the reduction of the magnet ML.

5.4 Core Loss Measurement and Estimation

The currently adopted core loss models in commercial FE software are based on calculating the machine core losses using curve fitting techniques that utilize core loss data provided by steel manufacturers under sinusoidal excitations. In [73], a core loss model for PMSMs is developed based on the magnetic flux variation loci in different parts of the motor that are predicted by carrying out a FE transient analysis. Since the flux variation pattern is complicated, an improved equation based on the conventional three-term expression is used for core loss calculation. In [74], the magnetic flux density distribution in a single-phase line-start PMSM are computed by using a two-dimensional FE method. The discrete Fourier transform is used to analyze the magnetic flux density waveforms in each element of the model and the core losses are evaluated using the measured core losses by an Epstein test apparatus.

The core loss measurement is a quite challenging step in the characterization of electrical machines. The existing standard procedures for measuring core losses in electrical machines are adapted for a simplified and standardized testing in the industry. The core losses obtained for such a test include several other sources of losses. As a result, the losses calculated by the use of traditional core loss models will most likely seem to be underestimated [75]. Different methods are proposed to measure the core losses and mechanical losses or to segregate the mechanical loss components [76]-[82]. In [77], the rotor of an IPM is replaced with a magnet-less rotor with identical geometry to measure the mechanical losses at different speeds. The measured mechanical loss data are used to separate the rotational loss components. Also, the friction and windage losses of electric machines can be calculated based on analytical methods [79], [80]. However, these methods require detailed information about the bearings and machine dimensions.

The ease of magnet demagnetization in VFMs can be utilized to facilitate the separation of the mechanical and core loss components, as the machine mechanical losses can be simply measured from the operating condition at which the magnets are completely demagnetized.

5.4.1 Core Loss Modeling

To develop an accurate core loss model, both radial and circumferential components of the magnetic flux density in each mesh element of the FE model should be taken into account. Fig. 5-8 shows the radial and circumferential components of the flux density in one mesh

element in the stator tooth when the AlNiCo magnets are fully magnetized and the VFM is rotating with a speed of 1000 rpm (50 Hz).

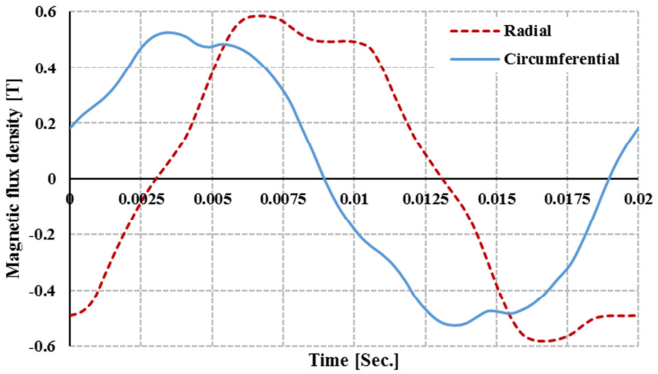

Fig. 5-8: Radial and circumferential components of magnetic flux density in one mesh element of the stator, 1000 rpm, and no-load condition.

It is clear that both components of the magnetic flux density are considerable in this mesh element. It can also be seen from Fig. 5-8 that the flux density waveforms are non-sinusoidal. Therefore, the analytical method should be able to consider the harmonic components of the flux density and their effects on the core loss components; the hysteresis and eddy current losses. In [83], it is shown that the core loss magnitude depends on the rate of flux density changes (*dB/dt*). According to this fact, an equivalent sinusoidal flux density can be defined that produces the same core losses as the non-sinusoidal magnetic flux density.

5.4.1.1 Equivalent Frequency Determination

To calculate the equivalent sinusoidal flux density waveform for a non-sinusoidal one, the flux density rate of change is first averaged over a complete magnetization cycle as [83]:

$$B^{(1)} = \frac{1}{\Delta B}\oint \frac{dB}{dt} dB \tag{5-2}$$

where $\Delta B = B_{max} - B_{min}$ in a cycle. (5-2) can be written as:

$$B^{(1)} = \frac{1}{\Delta B}\int_0^T \left(\frac{dB}{dt}\right)^2 dt \tag{5-3}$$

By considering the flux density variation as small linear pieces, (5-3) can be expressed as:

$$B^{(1)}=\frac{1}{B_{\max}-B_{\min}}\sum_{k=2}^{K}\left(\frac{B_k-B_{k-1}}{t_k-t_{k-1}}\right)^2(t_k-t_{k-1}) \tag{5-4}$$

B_k is the k[th] sample of the simulated flux density and t_k-t_{k-1} is the sampling time.

Based on the above-mentioned considerations, an equivalent sinusoidal magnetic flux density can be defined as:

$$B_{\sin,eq}(t)=\frac{\left(B_{\max}-B_{\min}\right)}{2}\times sin\left(2\pi f_{eq}t\right) \tag{5-5}$$

where f_{eq} is the equivalent frequency. According to (5-3), the average range of change for a sinusoidal magnetic flux density can be calculated as:

$$\begin{aligned}B_{\sin,eq}^{(1)}&=\frac{1}{B_{\max}-B_{\min}}\int_0^T\left(\frac{dB_{\sin,eq}}{dt}\right)^2dt=\\&=\frac{1}{B_{\max}-B_{\min}}\int_0^T\left(\frac{2\pi f_{eq}\left(B_{\max}-B_{\min}\right)}{2}\times\cos\left(2\pi f_{eq}t\right)\right)^2dt\end{aligned} \tag{5-6}$$

(5-6) can be simplified as:

$$\begin{aligned}&B_{\sin,eq}^{(1)}=\pi^2{f_{eq}}^2\left(B_{\max}-B_{\min}\right)\int_0^T\cos^2\left(2\pi f_{eq}t\right)dt\\&=\pi^2{f_{eq}}^2\left(B_{\max}-B_{\min}\right)\int_0^T\frac{1}{2}(\cos\left(4\pi f_{eq}t\right)+1)dt=\frac{\pi^2{f_{eq}}^2\left(B_{\max}-B_{\min}\right)T}{2}\\&\xrightarrow{T=\frac{1}{f_{eq}}}B_{\sin,eq}^{(1)}=\frac{\pi^2 f_{eq}\left(B_{\max}-B_{\min}\right)}{2}\end{aligned} \tag{5-7}$$

Based on the core loss model, the average rate of change of the equivalent sinusoidal flux density waveform should be equal to the same value of the non-sinusoidal flux density waveform. Thus, f_{eq} is determined based on (5-4) and (5-7) as [84], [85]:

$$\begin{aligned}&B^{(1)}=B_{\sin,eq}^{(1)}\rightarrow\\&\frac{1}{B_{\max}-B_{\min}}\sum_{k=2}^{K}\left(\frac{B_k-B_{k-1}}{t_k-t_{k-1}}\right)^2(t_k-t_{k-1})=\frac{\left(B_{\max}-B_{\min}\right)}{2}\pi^2 f_{eq}\\&\rightarrow f_{eq}=\frac{2}{\pi^2}\times\sum_{k=2}^{K}\left(\frac{B_k-B_{k-1}}{B_{\max}-B_{\min}}\right)^2\times\frac{1}{t_k-t_{k-1}}\end{aligned} \tag{5-8}$$

The high order harmonics in the steel flux waveforms may affect the hysteresis loss

component. Depending on the phase and magnitude of these harmonics, the resulting flux waveforms in the machine core may contain local flux reversals causing minor hysteresis loops to occur inside the main loop. The core loss model should be able to consider the minor loop losses. According to (5-8), f_{eq} is calculated based on the magnetic flux density variations that means that the effect of the local reversals in the flux density waveform is included. As a result, the effect of minor loops is considered in the equivalent frequency calculation. Moreover, this model also considers the effect of the flux harmonic content on the eddy current loss.

For the magnetic flux density waveforms in Fig. 5-8, the calculated f_{eq} for the radial and circumferential components is 63.7 Hz, and 59.58 Hz, respectively. The peak value of the equivalent sinusoidal flux density for the radial and circumferential components is 0.58 T and 0.53 T, respectively. According to these values, the equivalent frequency for the radial and circumferential components is increased by 27.4% and 19.2% in comparison with the supply frequency of 50 Hz.

5.4.1.2 Magnetic Material Core Loss Measurement

To implement the core loss model and apply it to the FE model, the core loss density of the VFM steel material (M19 G29), is measured using an Epstein frame test for a wide range of frequencies from 20 Hz to 4 kHz. Fig. 5-9 shows the measured core loss density of M19 G29 in Watt/kg. For higher frequencies, the achievable maximum flux density by the test setup is reduced. As a result, the curve fitting method is applied to estimate the core loss density at higher magnetic flux densities and higher frequencies.

5.4.1.3 Implementation of the Proposed Method in the FE Model

The magnetic flux density components and the area of each mesh element of the VFM model are first extracted from the FE simulation [67]. The equivalent frequency and the peak value of equivalent sinusoidal flux density (B_{eq}) for all components are calculated in each mesh element using (5-8).

The measured core loss density for M19 G29 is used as a lookup table to estimate the core loss density of each mesh. For the mesh element of Fig. 5-8, the estimated core loss density based on the measured data of Fig. 5-9 is 0.52 Watt/kg for the radial component of the magnetic flux density and 0.4 Watt/kg for the circumferential component.

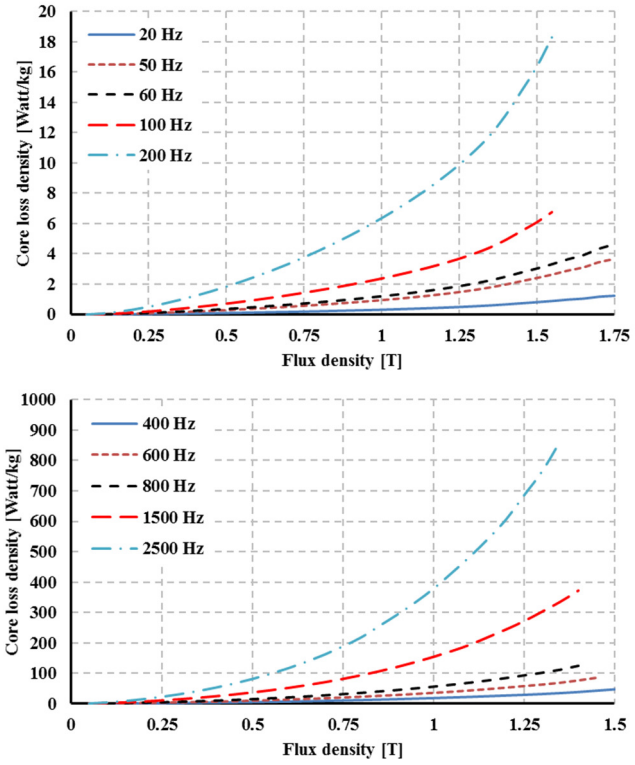

Fig. 5-9: The measured core loss density in Watt/kg for M19 G29.

Fig. 5-10 shows the developed meshes in a selected part of the stator, the equivalent frequency of the magnetic flux density component (black: radial and red: circumferential) in Hz and the resultant core loss density for each mesh in Watt/kg for the no-load VFM at 1000 rpm (50 Hz supply frequency). The selected part, is a part of the stator tooth close to the air gap. It can be seen that for meshes closer to the air gap, f_{eq} is higher than the meshes in the center of the stator tooth. For the meshes that are closer to the center of the tooth, the flux lines will be more radial, and will have less harmonics. As a result, f_{eq} for radial component is closer to the supply frequency. Moreover, the core loss density for meshes close to the air gap is higher than the meshes in the center of the stator tooth. The total core losses for each part of the machine are then calculated using,

$$P_{core,i} = L\rho \sum_{j=1}^{N} p_j A_j \tag{5-9}$$

where $P_{core,i}$ is the total core losses of part i, L is the stack length of the machine, ρ is the magnetic material mass density, N is the number of mesh elements in part i, p_j is the estimated core loss density in each mesh element of part i, and A_j is the area of the mesh element.

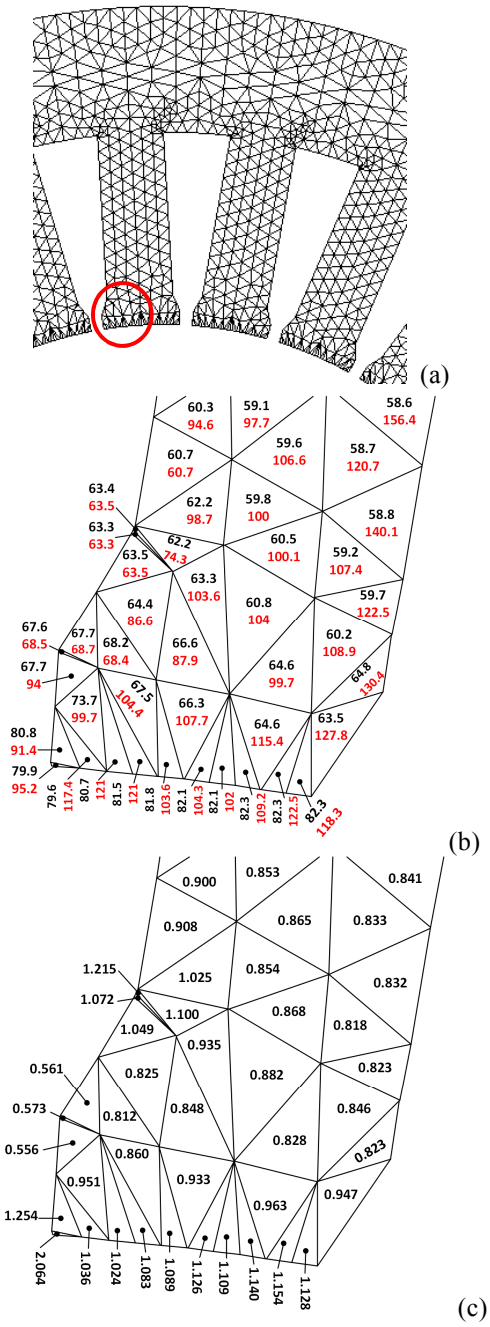

Fig. 5-10: (a) Developed mesh in the stator, (b) the equivalent frequency for magnetic flux density components (black: radial, red: circumferential) in Hz, and (c) the estimated core loss density in Watt/kg in each mesh of the selected section for the no-load VFM at 1000 rpm.

Fig. 5-11 shows the block diagram of the proposed core loss model.

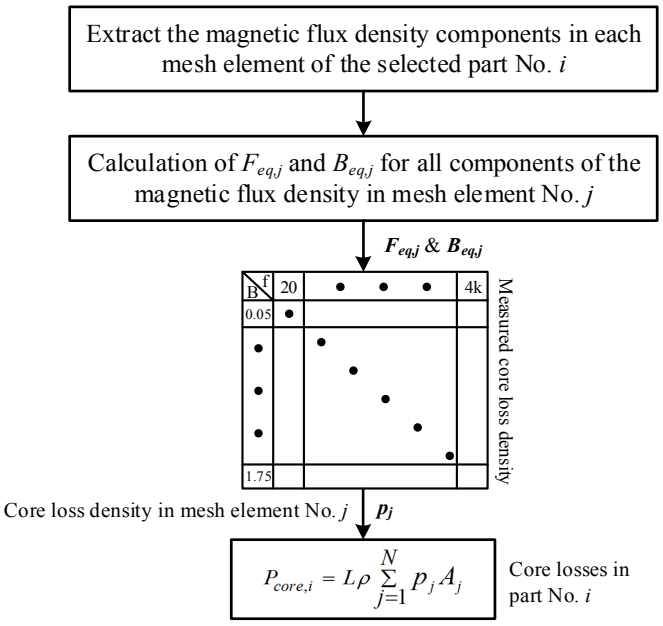

Fig. 5-11: The proposed core loss model.

5.4.2 Test Setup and Experimental Procedure

The rotational loss separation in VFMs is a straightforward procedure, as the magnet ML can be controlled by injecting armature *d*-axis current pulses. To measure the VFM core losses, the machine is driven by a DC motor with the VFM magnets adjusted at different MLs. Fig. 5-12 shows the experimental test setup. Five case studies are conducted based on the state of the magnet flux which is varied from approximately 0% to 100% in 25% intervals.

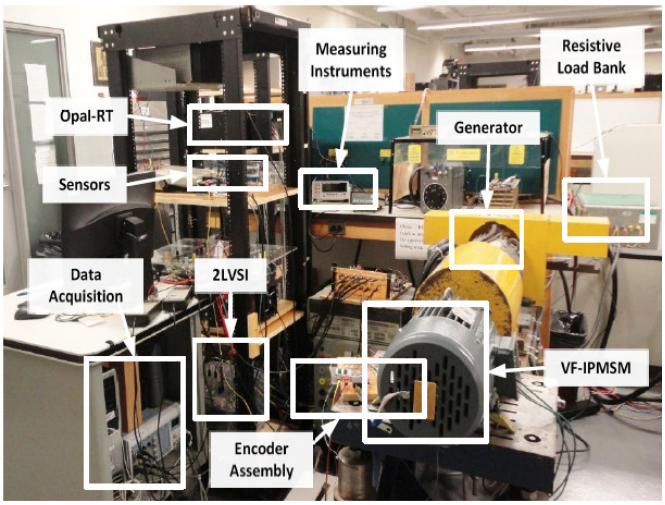

Fig. 5-12: Experimental setup to measure the core loss.

5.4.2.1 *Friction and Windage Loss Measurements*

To measure the mechanical losses of the VFM, the fully demagnetized VFM is coupled to the DC motor as a no-load generator. For the VFM at no-load condition, the Ohmic loss in the stator is zero. Moreover, the magnet flux is close to zero and the core losses in both the rotor and the stator are negligible. Therefore, the VFM input power can be considered equivalent to the mechanical losses. To perform the measurements, the magnet flux is initially reduced to approximately 0.003 Wb (0.6%). The VFM speed is then increased from 200 rpm to 1800 rpm. In each speed interval, the output torque of the DC motor is measured using a torque transducer, which is eventually used to estimate the machine mechanical losses. Fig. 5-13 shows the measured friction and windage losses for VFM at different speeds.

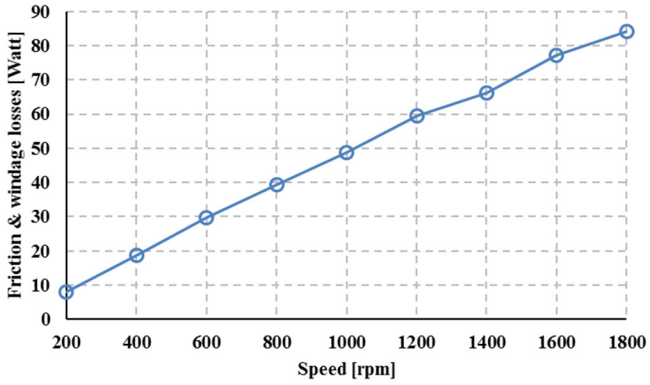

Fig. 5-13: Measured friction and windage losses for VFM at different speeds.

5.4.2.2 *VFM Core Loss Measurement*

To evaluate the effect of the ML of the rotor magnets on the core losses, the VFM with a specific ML is run as a no-load generator from 200 rpm to 1800 rpm. The core losses at each speed and ML can be calculated as:

$$P_{core} = P_{in} - P_{mech} \tag{5-10}$$

The core losses of the VFM are measured at MLs of 25%, 50%, 75% and 100%. However, the experimentally measured core losses for the 25% magnetization are found to be inaccurate as the mechanical losses dominates the total measured VFM losses.

To measure the core loss of the VFM in the loaded condition, the input and output of the VFM are measured at different loading conditions. The difference between the input and output of the VFM is the total loss. The core loss is then calculated by subtracting the Ohmic loss and

mechanical loss from the total loss. The Ohmic loss is calculated based on the rms value of the 3-phase currents and a phase resistance of 1.3Ω.

Fig. 5-14 shows the measured and estimated core losses of the VFM at MLs of 50%, 75% and 100%. The estimated core losses are based on the FE simulation coupled with the proposed core loss model.

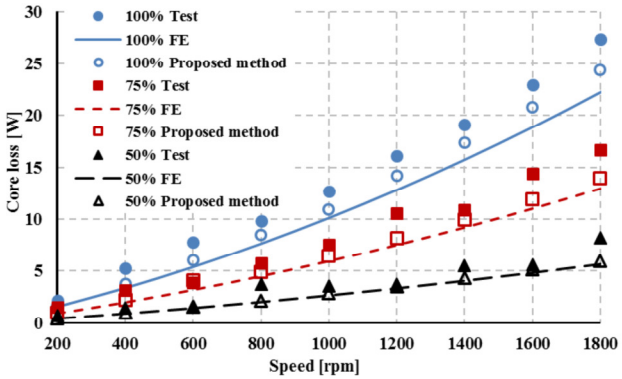

Fig. 5-14: Core loss in Watt for 100%, 75% and 50% level of magnetization at different speeds.

The VFM core losses are calculated using two methods; the standard core loss model in the FE software and the proposed core loss model coupled with the FEA simulation. According to Fig. 5-14, the results from the FE software underestimate the no-load core loss of the VFM as the FE package uses the Steinmetz equations with constant coefficients for different harmonics of the flux density. It can be seen from Fig. 5-14 that the estimated core losses are in good correlation with measured VFM losses at different ML with an average deviation of 12%. This deviation can be attributed to the change of the magnetic properties of the steel material during the manufacturing process.

To verify the proposed model in the loaded condition, the FE model of the VFM is supplied with the current waveforms which are captured from the experiments. Table 5-4 compares the core loss of the VFM with different stator currents at 1000 rpm for different magnetization levels. According to this table, the proposed method results are closer to the experimental test results in comparison with the FE results. Moreover, it is clear that the core loss increases with the armature current magnitude, which is related to the flux density level change in the stator and also the increased harmonic content of magnetic flux density waveforms. A comparison between the results of Fig. 5-14 and Table 5-4 shows that the core loss of the VFM increases in the loaded condition.

Table 5-4. Comparison of core loss for different load and magnetization levels at 1000 rpm.

ML%	RMS current [A]	Core loss [Watt]		
		Experimental	FE	Proposed method
100%	5	49.25	37.56	41.09
	7.5	84.45	66.84	74.65
	9	110.94	89.96	99.19
75%	5	39.89	27.23	33.65
	7.5	68.11	48.45	61.76
	9	93.5	77.68	84.09
50%	5	31.88	20.06	27.33
	7.5	56.85	41.83	51.71
	9	76.35	56.17	69.56

5.5 Conclusion

In this chapter, a test procedure was developed to measure the required energy for the magnetization and demagnetization. An analytical method based on the magnet operating point is developed to estimate the required energy for the magnetization and demagnetization procedures and verified using the test results. Based on the results, the input voltage and pulse duration should be selected to reduce the current pulse transient time in order to reduce the injected energy. Moreover, the results show that negligible Ohmic loss occurs during the demagnetization procedure in VFMs compared to the rare-earth PMSMs. This is a significant advantage of the VFM and guarantees the high performance of this machine in the field-weakening mode of operation.

The test and FE simulation results showed that the torque peak to peak value is almost constant with the variation of the ML and the torque mean value is a quasi-linear function of the ML. As a result, the torque ripple value increased with the ML reduction. The relationship between the no-load back-EMF and the ML of the magnet was discussed. The RMS value of the no-load back-EMF is reduced with the ML reduction and at the same time, the THD is almost fixed. Furthermore, the harmonic content of the no-load air gap flux density at two points in the air gap was analyzed. This shows that the THD of the no-load air gap flux density is almost constant with the ML variation, which justifies the almost constant torque peak to peak value of this machine at different MLs.

Moreover, a core loss model is developed to calculate the no-load core losses of the VFM using the magnetic flux density components in each mesh element of the FE model. The proposed model is based on the calculation of an equivalent sinusoidal magnetic flux density for the non-sinusoidal magnetic flux density waveform. The proposed model was implemented in FE software to calculate the core losses of the existing VFM. In order to validate the developed model, a measurement technique was presented to measure and segregate the no-load core losses and the mechanical losses and also the loaded core losses of the VFM at different MLs. The proposed model results were verified with the experimental results, and the results agreement shows that the developed model has a great potential for precise machine core loss prediction.

Chapter 6. Conclusions and Future Research

6.1 Conclusions

In Chapter 2, an analytical model of a spoke type VFM at no-load condition has been discussed and verified using the FE results. An analytical model can be used as a powerful tool to facilitate the design of VFM. A magnetic equivalent circuit of a spoke type PMSM was used to calculate the no-load air gap flux density of the machine considering the effects of stator slots and uneven air gap length. The air gap length is minimum in the center of stator teeth, and it is maximum in the center of the stator slots. The no-load back-EMF, the magnetization current, the average magnet torque vs. torque angle, and the peak to peak torque value were estimated using the analytical model. The peak value of the no-load air gap flux density increases with the increase in the magnet length and decreases with the decrease in the magnetization level of magnets, which leads to an output torque reduction. Moreover, an increase in both magnet length and width increase the magnet torque mean value in this machine. Besides, an increase in the magnet thickness increases the magnetization current of the VFM.

In Chapter 3, a complex multi-objective optimization problem was transferred to a two-level optimization procedure to reduce $T_r\%$, and I_{mag}, and to keep T_{mean} within an acceptable range. Moreover, the no-load operating point of the magnet must be considered during the optimization procedure. Experimental results of the existing VFM showed torque ripple of 17.6% and a 40 A peak magnetization current. A new analytical design criterion was developed to select the AlNiCo magnet size in the spoke type VFM based on the desired magnetization current and the torque mean value. The FE-based optimization strategy was discussed and the main guidelines to use the Genetic Algorithm were proposed. After performing the optimization, the optimized case was proposed with 11% reduction in the magnet volume, 57% reduction in the torque ripple, 4.4% reduction in the torque mean value and 12.5% reduction in the magnetization current.

Chapter 4 focused on a new design of AlNiCo-based radially magnetized VFM with conventional saliency to keep the promising features of the VFM and enhance its power and torque capabilities in the field-weakening region considering the demagnetization of the AlNiCo magnets. To achieve this, a VFM was designed with interior magnets positioned to

keep the fully magnetized condition at no-load, withstand the demagnetizing effect of *q*-axis armature flux, and be able to get demagnetized and re-magnetized using the *d*-axis current pulse. A design procedure of the radially magnetized VFM was presented and the impact of magnet dimensions, position selection, and barrier shape on the machine performance were discussed. A FE-based design optimization strategy to minimize the torque ripple of the machine and guarantee the high torque capability of the machine was proposed. The optimized radially magnetized design was compared with the existing VFM, and the results showed 70% reduction in torque ripple and an improved power capability for a wider range of the speed. Moreover, the optimized design has high efficiency for a wide range of speed.

Chapter 5 focused on the characterization of the existing VFM at different magnetization levels including the magnetization and demagnetization energy, torque ripple, and core losses.

A test procedure was developed to measure the required energy for the magnetization and demagnetization procedures. It was shown that the input voltage and the pulse duration should be selected to reduce the current pulse transient time, which directly reduces the required energy for demagnetization. An analytical method based on the magnet operating point from FE software, was developed to estimate the required energy for the magnetization and demagnetization procedures and was verified using the test results. The results showed negligible Ohmic loss for the demagnetization procedure in comparison with the rare-earth PMSMs, which results in higher performance in the field-weakening mode of operation.

The test and FE simulation results showed that the torque peak to peak value is almost constant with the variation of the magnetization level, and the torque mean value is a quasi-linear function of the magnetization level. Consequently, the torque ripple value increased with the magnetization level reduction. Moreover, the FE results showed that the RMS value of the no-load back-EMF reduces with the reduction of the magnetization level. The analysis also showed that THD of the no-load air gap flux density is almost constant with the magnetization level variation which justifies the constant torque peak to peak value at different magnetization levels.

A core loss model was developed to calculate the core losses of the VFM at different load conditions by calculating an equivalent sinusoidal magnetic flux density for the non-sinusoidal magnetic flux density waveform in each mesh element of the FE model. In order to validate the developed core loss model, a measurement technique was presented to measure and segregate

the no-load core losses, the mechanical losses, and the loaded core losses of the VFM at different magnetization levels. The proposed model results were compared with the experimental results and showed a good prediction of the core losses at different magnetization levels. The core loss analysis in this chapter showed that the core losses of the VFM increase with the increase of the rotor speed, the magnetization level, and the stator current.

6.2 Proposed Future Research

- ☐ Design of an AlNiCo-based VFM for an actual electrical powertrain with a rated current higher than the magnetization current. Different stator winding configuration for high current density applications, such as a hairpin stator winding, can be considered in this design.
- ☐ Design optimization of an AlNiCo-based VFM considering the performance and cost and using multi-objective GA of the FEA software.
- ☐ Design of an axial-flux AlNiCo-based VFM for in-wheel applications.
- ☐ Design of an AlNiCo-based VFM with fractional stator windings.
- ☐ Compare the results of the 2D and 3D models of the VFM considering the eddy currents in rotor and stator cores, as well as the magnets.

References

[1]. M.J. Kramer, R. W. McCallum, I. A. Anderson, and S. Constantinides, “Prospects for Non-Rare Earth Permanent Magnets for Traction Motors and Generators,” *The Journal of The Minerals, Metals & Materials Society*, vol. 64, issue 7, pp. 752-763, July 2012.

[2]. Adrian Quesada, “The permanent magnets challenge,” Instituto de Ceramica y Vidrio, icv 50, 2014.

[3]. Mark Seddon, and Argus Media Ltd., “Analysing the Changing Global Rare Earths Supply and Demand Outlook,” Argus Metal Pages Forum, Tokyo, 4 August 2016.

[4]. W. L. Soong and T. J. E. Miller, “Field-weakening performance of brushless synchronous AC motor drives,” *in IEE Proceedings Electric Power Applications,* vol. 141, no. 6, pp. 331-340, Nov. 1994.

[5]. R. Schifer and T. A. Lipo, "Core loss in buried magnet permanent magnet synchronous motors," in IEEE Transactions on Energy Conversion, vol. 4, no. 2, pp. 279-284, Jun 1989.

[6]. F. Chai, K. Zhao, Z. Li and L. Gan, "Flux Weakening Performance of Permanent Magnet Synchronous Motor With a Conical Rotor," in *IEEE Transactions on Magnetics*, vol. 53, no. 11, pp. 1-6, Nov. 2017.

[7]. Z. Zheng, Y. Li, K. Wang and L. Qiu, "A new adaptive flux weakening method of PMSM," *2011 International Conference on Electrical Machines and Systems*, Beijing, 2011, pp. 1-5.

[8]. L. Sepulchre, M. Fadel, M. Pietrzak-David and G. Porte, "New high speed PMSM flux-weakening strategy," *2016 19th International Conference on Electrical Machines and Systems (ICEMS)*, Chiba, 2016, pp. 1-6.

[9]. D. Fodorean, A. Djerdir, I. A. Viorel, & A. Miraoui, “A Double Excited Synchronous Machine for Direct Drive Application—Design and Prototype Tests,“ *IEEE Trans. on Energy Conversion*, vol.22, no.3, pp.656-665, Sept. 2007

[10]. Yue Li, & T. A. Lipo, “A doubly salient permanent magnet motor capable of field weakening,” *Power Electronics Specialists Conference*, 1995. PESC ’95 Record, 26th Annual IEEE, vol.1, no., pp.565-571 vol.1, 18-22 Jun 1995.

[11]. F. Leonardi, T. Matsuo, Y. Li, T. A. Lipo, & P. McCleer, “Design considerations and test results for a doubly salient PM motor with flux control,” *Industry Applications Conference, 1996. Thirty-First IAS Annual Meeting, IAS ’96*., Conference Record of the 1996 IEEE, vol.1, no., pp.458-463 vol.1, 6-10 Oct 1996.

[12]. T. Kosaka, Y. Kano, N. Matsui, & C. Pollock, “A novel multi-pole permanent magnet synchronous machine with SMC bypass core for magnet flux and SMC field-pole core with toroidal coil for independent field strengthening/weakening,” *2005 European Conference on Power Electronics and Applications*, pp. 10-, 11-14 Sept. 2005.

[13].I. Ozawa, T. Kosaka, and N. Matsui, "Less rare- earth Magnet-high power density hybrid excitation motor designed for hybrid electric vehicle drives" *European Conference on Power Electronics and Applications*, 2009. EPE 2009.

[14].R. Owen, Z. Q. Zhu, J. B. Wang, D. A. Stone, and I. Urquhart, "Review of variable-flux permanent magnet machines*," in Proc. Int. Conf. Electr. Mach. Syst. (ICEMS)*, Beijing, China, 2011, pp. 1-6.

[15].M. Aydin, S. Huang, & T. A. Lipo, "A new axial flux surface mounted permanent magnet machine capable of field control," *Conference Record of the Industry Applications Conference*, 2002. 37th IAS Annual Meeting. Vol. 2, pp. 1250-1257, 2002.

[16].M. Aydin, S. Huang, & T. A. Lipo, "Performance evaluation of an axial flux consequent pole PM motor using finite element analysis," *IEEE International Electric Machines and Drives Conference*, 2003. IEMDC'03, vol.3, pp. 1682-1687, 1-4 June 2003.

[17].J. A. Tapia, F. Leonardi, & T. A. Lipo, "Consequent-pole Permanent-magnet machine with extended field-weakening capability", *IEEE Transactions on Industry Applications,* Vol. 39, No. 6, pp1704-9, Nov-Dec 2003.

[18].W. Huijun, A. Zhongliang, T. Renyuan, & N. Yingli, "Design of a hybrid excitation permanent magnet synchronous with low voltage regulation," *Proceedings of the Eighth International Conference on Electrical Machines and Systems*, 2005. ICEMS 2005, vol.1, pp. 480-483, 27-29 Sept. 2005.

[19].S. Hlioui, L. Vido, Y. Amara, M. Gabsi, M. Lecrivain, A. Miraoui, "PM and hybrid excitation synchronous machines: Performances comparison," *18th International Conference on Electrical Machines*, 2008. ICEM 2008, pp.1-6, 6-9 Sept. 2008.

[20].J. S. Hsu, S.–T. Lee; & L. M. Tolbert, "High-Strength Undiffused Brushless (HSUB) Machine," *Proceedings of the IEEE Industry Applications Society Annual Meeting*, 2008. IAS '08, pp.1-8, 5-9 Oct. 2008

[21].J. S. Hsu, T. A. Burress, S. T. Lee, R. H. Wiles, C. L. Coomer, J. W. McKeever, & D. J. Adams, "16,000-RPM Interior Permanent Magnet Reluctance Machine with Brushless Field Excitation," *Proceedings of the IEEE Industry Applications Society Annual Meeting*, 2008. IAS '08, pp.1-6, 5-9 Oct. 2008.

[22].T. Finken, & K. Hameyer, "Study of Hybrid Excited Synchronous Alternators for Automotive Applications Using Coupled FE and Circuit Simulations," *IEEE Transactions on Magnetics*, vol.44, no.6, pp.1598-1601, June 2008.

[23].N. Naoe, T. Fukami, "Trial production of a hybrid excitation type synchronous machine," *Proceedings of the IEEE Electric Machines and Drives Conference*, 2001. IEMDC 2001, pp.545-547, 2001.

[24].K. T. Chau, J. Z. Jiang, & Y. Wang, "A novel stator doubly fed doubly salient permanent magnet brushless machine," *IEEE Transactions on Magnetics*, vol.39, no.5, pp. 3001-3003, Sept. 2003.

[25].K. T. Chau, Y. B. Li, J. Z. Jiang, & S. Niu, “Design and Control of a PM Brushless Hybrid Generator for Wind Power Application,” *IEEE Transactions on Magnetics*, vol.42, no.10, pp.3497-3499, Oct. 2006.

[26].R. L. Owen, Z. Q. Zhu, & G. W. Jewell, "Hybrid excited flux-switching permanent magnet machines," *13th European Conference on Power Electronics and Applications*, 2009. EPE '09, pp.1-10, 8-10 Sept. 2009

[27].J. T. Chen, Z. Q. Zhu, S. Iwasaki, R. Deodhar, “A novel hybrid excited switching-flux brushless AC machine for EV/HEV applications,” *IEEE Trans. on Vehicular Technology*, vol.60, no.4, pp.1365-1373, 2011.

[28].Chunhua Liu, K. T. Chau, J. Z. Jiang, Xinhua Liu, & Zheng Wang, "Design and Control of a Doubly-Excited Permanent-Magnet Brushless Integrated-Starter-Generator for Hybrid Electric Vehicles," *Conference Record of the 2007 IEEE Industry Applications Conference, 2007*. 42nd IAS Annual Meeting, pp.1702-1709, 23-27 Sept. 2007.

[29].F. Caricchi, F. Crescimbini, F. G. Capponi, & L. Solero, “Permanent-magnet, directdrive, starter/alternator machine with weakened flux linkage for constant-power operation over extremely wide speed range,” *Conference Record of the 2001 IEEE Industry Applications Conference, 2001*. Thirty-Sixth IAS Annual Meeting, vol.3, pp.1626-1633, 30 Sep-4 Oct 2001.

[30].L. Del Ferraro, F. G. Capponi, R. Terrigi, F. Caricchi, & O. Honorati, “Ironless Axial Flux PM Machine With Active Mechanical Flux Weakening For Automotive Applications,” *Conference Record of the 2006 IEEE Industry Applications Conference, 2006*. 41st IAS Annual Meeting, vol.1, pp.1-7, 8-12 Oct. 2006.

[31].L. Ma, M. Sanada, S. Morimoto, & Y. Takeda, “Advantages of IPMSM with adjustable PM armature flux linkage in efficiency improvement and operating range extension,” *Proceedings of the Power Conversion Conference*, 2002. PCC Osaka 2002, vol.1, pp.136-141, 2002.

[32].C. Yu and K. T. Chau, “Design, analysis, and control of DC-excited memory motors,” *IEEE Transactions on Energy Conversion*, vol. 26, no. 2, pp. 479-489, Jun. 2011.

[33].H. Yang *et al*., "Design Synthesis of Switched Flux Hybrid-Permanent Magnet Memory Machines," in *IEEE Transactions on Energy Conversion*, vol. 32, no. 1, pp. 65-79, March 2017.

[34].H. Hua, Z. Q. Zhu, A. Pride, R. Deodhar, and T. Sasaki, “A novel variable flux memory machine with series hybrid magnets,” *in 2016 IEEE Energy Conversion Congress and Exposition (ECCE)*, 2016, pp. 1–8.

[35].K. Sakai, K. Yuki, Y. Hashiba, N. Takahashi, and K. Yasui, “Principle of the variable-magnetic-force memory motor,” *in 2009 International Conference on Electrical Machines and Systems, 2009*, pp. 1–6.

[36].A. Athavale, K. Sasaki, B. S. Gagas, T. Kato, and R. D. Lorenz, “Variable Flux Permanent Magnet Synchronous Machine (VF-PMSM) Design Methodologies to Meet Electric Vehicle Traction Requirements with Reduced Losses,” *IEEE Transactions on Industry Applications,* vol. 53, no. 5, pp. 4318–4326, Sep. 2017.

[37].Y. Zhou, Y. Chen, and J. X. Shen, “Analysis and Improvement of a Hybrid Permanent-Magnet Memory Motor,” *IEEE Transactions on Energy Conversion*, vol. 31, no. 3, pp. 915–923, Sep. 2016.

[38].V. Ostovic, “Memory motors,” *IEEE Industry Applications Magazine,* vol. 9, no. 1, pp. 52-61, Jan./Feb. 2003.

[39].N. Limsuwan, T. Kato, K. Akatsu, and R. D. Lorenz, “Design and Evaluation of a Variable-Flux Flux-Intensifying Interior Permanent-Magnet Machine,” *IEEE Transactions on Industry Applications*, vol. 50, no. 2, pp. 1015–1024, Mar. 2014.

[40].T. Kato, N. Limsuwan, C. Y. Yu, K. Akatsu, and R. D. Lorenz, “Rare Earth Reduction Using a Novel Variable Magnetomotive Force Flux-Intensified IPM Machine,” *IEEE Transactions on Industry Applications*, vol. 50, no. 3, pp. 1748–1756, May 2014.

[41].M. Ibrahim, L. Masisi and P. Pillay, "Design of Variable Flux Permanent-Magnet Machine for Reduced Inverter Rating," in *IEEE Transactions on Industry Applications*, vol. 51, no. 5, pp. 3666-3674, Sept.-Oct. 2015.

[42].M. Ibrahim, P. Pillay, "Design of high torque density variable flux permanent magnet machine using Alnico magnets," *2014 IEEE Energy Conversion Congress and Exposition (ECCE)*, vol., no., pp.3535,3540, 14-18 Sept. 2014.

[43].L. Masisi, M. Ibrahim and P. Pillay, "Control strategy of a variable flux machine using AlNiCo permanent magnets," *2015 IEEE Energy Conversion Congress and Exposition (ECCE)*, Montreal, QC, 2015, pp. 5249-5255.

[44].J. D. L. Ree and N. Boules, “Magnetic shaping to reduce induced voltage harmonics in PM machines with surface mounted magnets,” *IEEE Transactions on energy conversion*, vol. 6, pp. 155-161, 1991.

[45].Z. Q. Zhu, D. Howe, E. Bolte, B. Ackermann, “Instantaneous magnetic field distribution in brushless permanent magnet DC motors. I. Open-circuit field,” *IEEE Transactions on Magnetics,* vol.29, no.1, pp.124-135, Jan 1993.

[46].Z. Q. Zhu, D. Howe, “Instantaneous magnetic field distribution in brushless permanent magnet DC motors. II. Armature-reaction field,” *IEEE Transactions on Magnetics,* vol.29, no.1, pp.124-135, Jan 1993.

[47].Z. Q. Zhu, D. Howe, “Instantaneous magnetic field distribution in brushless permanent magnet DC motors. III. Effect of stator slotting,” *IEEE Transactions on Magnetics,* vol.29, no.1, pp.124-135, Jan 1993.

[48].Z. Q. Zhu, D. Howe, "Instantaneous magnetic field distribution in permanent magnet brushless DC motors. IV. Magnetic field on load," *IEEE Transactions on Magnetics,* vol.29, no.1, pp.124-135, Jan 1993.

[49].K. Boughrara, R. Ibtiouen, T. Lubin, "Analytical Prediction of Magnetic Field in Parallel Double Excitation and Spoke-Type Permanent-Magnet Machines Accounting for Tooth-Tips and Shape of Polar Pieces," *IEEE Transactions on Magnetics*, vol.48, no.7, pp.2121-2137, July 2012.

[50].M. R. Mohammad, Kim Kyung-tae, Jin Hur, "Design and Analysis of a Spoke Type Motor With Segmented Pushing Permanent Magnet for Concentrating Air-Gap Flux Density, " *IEEE Transactions on Magnetics*, vol.49, no.5, pp.2397-2400, May 2013.

[51].D. Lin, P. Zhou, C. Lu, S. Lin, "Analytical Prediction of Cogging Torque for Spoke Type Permanent Magnet Machines" *IEEE Transactions on Magnetics,* vol.48, no.2, pp.1035-1038, Feb. 2012.

[52].E. Carraro, N. Bianchi, S. Zhang, M. Koch, "Permanent magnet volume minimization of spoke type fractional slot synchronous motors," in *Energy Conversion Congress and Exposition (ECCE), 2014 IEEE* , vol., no., pp.4180-4187, 14-18 Sept. 2014.

[53].A. B. Proca, A. Keyhani, A. El-Antably, Lu. Wenzhe, Dai. Min, "Analytical model for permanent magnet motors with surface mounted magnets," *IEEE Transactions on energy conversion*, vol.18, no.3, pp.386-391, Sept. 2003.

[54].Wang Xinghua, Li Qingfu, Wang Shuhong, Li Qunfeng, "Analytical calculation of air-gap magnetic field distribution and instantaneous characteristics of brushless DC motors, " *IEEE Transactions on energy conversion*, vol.18, no.3, pp.424-432, Sept. 2003.

[55].D. C. Hanselman, "Brushless permanent-magnet motor design," New York, McGraw-Hill, 1994.

[56].M. M. Rahman, K. T. Kim and J. Hur, "Design and Optimization of Neodymium-Free SPOKE-Type Motor With Segmented Wing-Shaped PM," in IEEE Transactions on Magnetics, vol. 50, no. 2, pp. 865-868, Feb. 2014.

[57].A. Fatemi, D. M. Ionel, N. A. O. Demerdash and T. W. Nehl, "Optimal Design of IPM Motors With Different Cooling Systems and Winding Configurations," in IEEE Transactions on Industry Applications, vol. 52, no. 4, pp. 3041-3049, July-Aug. 2016.

[58].L. Yang, S. L. Ho, W. N. Fu and W. Li, "Design Optimization of a Permanent Magnet Motor Derived From a General Magnetization Pattern," in IEEE Transactions on Magnetics, vol. 51, no. 11, pp. 1-4, Nov. 2015.

[59].G. Lei, C. Liu, J. Zhu and Y. Guo, "Techniques for Multilevel Design Optimization of Permanent Magnet Motors," in *IEEE Transactions on* Energy Conversion, vol. 30, no. 4, pp. 1574-1584, Dec. 2015.

[60].C. Lu, S. Ferrari and G. Pellegrino, "Two Design Procedures for PM Synchronous Machines for Electric Powertrains," in *IEEE Transactions on Transportation Electrification*, vol. 3, no. 1, pp. 98-107, March 2017.

[61].M. van der Geest, H. Polinder, J. A. Ferreira and M. Christmann, "Power Density Limits and Design Trends of High-Speed Permanent Magnet Synchronous Machines," in *IEEE Transactions on Transportation Electrification*, vol. 1, no. 3, pp. 266-276, Oct. 2015.

[62].A. S. Isfanuti *et al*., "Small single-phase two pole Ferrite-PM-stator double-saliency motor: Optimal design and experimental characterization," *2016 XXII International Conference on Electrical Machines (ICEM)*, Lausanne, 2016, pp. 2492-2497.

[63].M. S. Islam, R. Islam and T. Sebastian, "Experimental Verification of Design Techniques of Permanent-Magnet Synchronous Motors for Low-Torque-Ripple Applications," in *IEEE Transactions on Industry Applications*, vol. 47, no. 1, pp. 88-95, Jan.-Feb. 2011.

[64].C. Desai and P. Pillay, "Torque and core loss characterization of a variable-flux permanent-magnet machine," *2016 IEEE Energy Conversion Congress and Exposition (ECCE)*, Milwaukee, WI, 2016, pp. 1-6.

[65].M. Chowdhury, A. Gebregergis, M. Islam and T. Sebastian, "Analysis of harmonic contents in induced voltage and electromagnetic torque in interior permanent magnet synchronous machines under loaded condition," *2013 International Electric Machines & Drives Conference*, Chicago, IL, 2013, pp. 260-267.

[66].Yoshiyuki Sakashita, “Study on the Application of the JMAG Optimization Function in Motor Design”, JMAG Users Conference 2015, 2015.

[67].*JMAG Version 16.1 Reference Manual, Volume 1*, 1st ed., JSOL Corporation, Tokyo, Japan, 2017.

[68].T. Fukushige, N. Limsuwan, T. Kato, K. Akatsu and R. D. Lorenz, "Efficiency Contours and Loss Minimization Over a Driving Cycle of a Variable Flux-Intensifying Machine," in *IEEE Transactions on Industry Applications*, vol. 51, no. 4, pp. 2984-2989, July-Aug. 2015.

[69].N. Limsuwan, Y. Shibukawa, D. D. Reigosa, and R. D. Lorenz, “Novel Design of Flux-Intensifying Interior Permanent Magnet Synchronous Machine Suitable for Self-Sensing Control at Very Low Speed and Power Conversion,” in *IEEE Transactions on Industry Applications*, vol. 47, no. 5, pp. 2004–2012, Oct. 2011.

[70].T. Kato, M. Minowa, H. Hijikata, K. Akatsu and R. D. Lorenz, "Design Methodology for Variable Leakage Flux IPM for Automobile Traction Drives," in *IEEE Transactions on Industry Applications*, vol. 51, no. 5, pp. 3811-3821, Sept.-Oct. 2015.

[71].S. Ray and D. A. Lowther, "Multi-Objective Optimization Applied to the Matching of a Specified Torque-Speed Curve for an Internal Permanent Magnet Motor," in *IEEE Transactions on Magnetics*, vol. 45, no. 3, pp. 1518-1521, March 2009.

[72].Edward P. Furlani, "Permanent Magnet and Electromechanical Devices: Materials, Analysis, and Application," San Diego, Academic Press, 2001.

[73].Yunkai Huang; Jianning Dong; Jian Guo Zhu; Youguang Guo, "Core Loss Modeling for Permanent-Magnet Motor Based on Flux Variation Locus and Finite-Element Method," *IEEE Transactions on Magnetics,* vol.48, no.2, pp.1023,1026, Feb. 2012.

[74].Hyuk Nam; Kyung-Ho Ha; Jeong-Jong Lee; Jung-Pyo Hong; Gyu-Hong Kang, "A study on iron loss analysis method considering the harmonics of the flux density waveform using iron loss curves tested on Epstein samples," *IEEE Transactions on Magnetics,* vol.39, no.3, pp.1472,1475, May 2003.

[75].A. Krings, S. Nategh, A. Stening, and J. Soulard, "Measurement and modeling of iron losses in electrical machines," In: Proceedings of the 5th International Conference Magnetism and Metallurgy WMM'12, Gent, Belgium: Gent University, 101-119 p, 2012.

[76].S. Zhu, M. Cheng, J. Dong and J. Du, "Core Loss Analysis and Calculation of Stator Permanent-Magnet Machine Considering DC-Biased Magnetic Induction," in *IEEE Transactions on Industrial Electronics*, vol. 61, no. 10, pp. 5203-5212, Oct. 2014.

[77].Lei Ma, M. Sanada, S. Morimoto and Y. Takeda, "Prediction of iron loss in rotating machines with rotational loss included," in *IEEE Transactions on Magnetics*, vol. 39, no. 4, pp. 2036-2041, July 2003.

[78].G. J. Yan, R. B. Lin and M. H. Jian, "Improvement on the core loss of high speed slotless PMBLDC motor and its measurement," *2012 15th International Conference on Electrical Machines and Systems (ICEMS)*, Sapporo, 2012, pp. 1-4.

[79].F. Gieras, R. Wang, M. Kamper, "Axial Flux Permanent Magnet Machines", Springer Netherlands, 2008, ISBN: 978-1-4020-8227-6.

[80].J. E. Vranick, "Prediction of Windage Power Loss in Alternators," NASA Technical Note, TN D-4849, pp. 1 – 18, October 1968.

[81].R. Wrobel, G. Vainel, C. Copeland, T. Duda, D. Staton and P. H. Mellor, "Investigation of Mechanical Loss Components and Heat Transfer in an Axial-Flux PM Machine," in *IEEE Transactions on Industry Applications*, vol. 51, no. 4, pp. 3000-3011, July-Aug. 2015.

[82].I. D. Ilina, "Experimental determination of moment to inertia and mechanical losses vs. speed, in electrical machines," *2011 7TH INTERNATIONAL SYMPOSIUM ON ADVANCED TOPICS IN ELECTRICAL ENGINEERING (ATEE)*, Bucharest, 2011, pp. 1-4.

[83].J. Reinert, A. Brockmeyer, and R. De Doncker, "Calculation of losses in ferro- and ferrimagnetic materials based on the modified steinmetz equation," *IEEE Transactions on Industry Applications,* vol. 37, no. 4, pp. 1055–1061, Jul 2001.

[84].L. Masisi, A. Takbash and P. Pillay, "Core Loss Performance of a New PM Machine Topology for Electric Vehicles", *Electric Machines and Drives Conference, 2014. IEMDC '14. IEEE International*.

[85].M. Albach, T. Durbaum and A. Brockmeyer, "Calculating core losses in transformers for arbitrary magnetizing currents a comparison of different approaches," *in Power Electronics Specialists Conference, 1996. PESC '96 Record, 27th Annual IEEE*, vol.2, no., pp.1463-1468 vol.2, 23-27 Jun 1996.